Hybrid Molecular Dynamics – Continuum Mechanics for Polymers

TECHNISCHE UNIVERSITÄT DARMSTADT

Vom Fachbereich Chemie
der Technischen Universität Darmstadt

zur Erlangung des akademischen Grades eines
Doktor rerum naturalium (Dr. rer. nat.)

genehmigte
Dissertation

vorgelegt von

Mohammad Rahimi, M.Sc. of Physics

aus Isfahan, Iran

Referent: Prof. Dr. Florian Müller-Plathe
Korreferent: Prof. Dr. Nico van Der Vegt
Tag der Einreichung: 19.10.2012
Tag der mündliche Prüfung: 3.12.2012

Darmstadt 2013
D 17

Summary

The interaction of polymers and a solid surface modifies the polymer properties near the surface (the so-called interphase) in comparison to those of the bulk polymers. A clear explanation of the origin of this modification in the polymer properties is still missing. The aim of my PhD thesis has been the study of the mechanical properties of nanocomposite materials and the analysis of the behavior of polymers in the interphase region under deformation. Coarse-grained simulations have been performed for a model system of silica nanoparticles (NPs) embedded in atactic polystyrene (PS). In this case molecular details are important only in a small spatial region of the interphase. The rest of the polymer has bulk-like behavior which can be described by continuum mechanics. Therefore, it is convenient to simulate the region of interest by molecular dynamics (MD) and to treat the rest of the nanocomposite by continuum mechanics methods. To fulfill this we developed a new hybrid molecular – continuum simulation method for polymers. In our model the center of the simulation box is treated by MD. This region is surrounded by a continuum domain which is described by a finite element approach. To the best of our knowledge, the present work is the first attempt to use simultaneously MD and FE methods in simulations of polymers. It has been the main motivation of this work to develop a new hybrid scheme for polymers. Coupling a MD to a FE method requires a lot of modifications in both the MD and FE domains. The introduction of my thesis contains a short review on the existing hybrid schemes and modifications needed to couple the two domains. Difficulties to couple them such as transferring the information between two domains and equilibrating the continuum domain are explained. Different methods and techniques to overcome these difficulties as well as the advantages and disadvantages of each method are described briefly. These methods, however, are limited to liquid and crystalline solid materials. They have to be modified to be capable of simulating polymers. In the present PhD thesis we have explained the technical difficulties to couple a MD to a FE model for polymers in the MD domain and how we tackled these problems. Modifications in the FE domain have been done by researchers in the Applied Mechanics Department of the University of Erlangen. The current work has involved a strong collaboration with them to integrate a modified MD domain into a FE domain.

In the second chapter of the thesis, the mechanical properties of a pure polystyrene matrix as well as a polystyrene matrix filled with bare silica nanoparticles are investigated by MD simulations at the coarse-grained level. The stress-strain curve of polystyrene has been computed for a range of temperatures below and above the glass transition. The Young's modulus of polystyrene obtained from the stress-strain curve has been compared to experimental and atomistic simulation data. By studying the local segmental orientation and the local structure of the polymer near the nanoparticle surface

under deformation, we have found that the segments close to the silica nanoparticle surface are stiffer than those in the bulk. The thickness of the interphase has been estimated. We have shown that the Young's modulus of the studied nanocomposite increases by increasing the volume fraction of the nanoparticle. The results of interphase studies under deformation as described in this section are important input parameters for the FE simulations in the present hybrid scheme; this will explained in chapter four.

In hybrid simulations the usual periodic boundary conditions of MD cannot be used as the MD domain is surrounded by a FE domain. In hybrid schemes boundary conditions should allow an information transfer through the boundary region between two domains. Therefore, I developed new non-periodic boundary conditions, so-called stochastic boundary conditions (SBC), which are able to transfer information (forces and deformations) between the two domains and to minimize the artifacts in the dynamics. In the SBC ensemble we have defined a set of auxiliary particles, so-called anchor points, in the boundary region. The anchor points are harmonically coupled to the MD particles. They play an important role to transfer the information between the MD and FE domains. Particles in the boundary region are forced to mimic the bulk behavior by employing a stochastic dynamics in the boundary region. This minimizes the artificial influence of the anchor points and the vacuum on the polymers in the center of the box. The SBCs are explained in more detail in the third chapter. We have validated these boundary conditions by comparing the results of coarse-grained polystyrene melts under non-periodic and regular periodic boundary conditions. Excellent agreement is found for thermodynamic, structural, and dynamic properties.

The new hybrid molecular – continuum method for polymers is explained in more detail in chapter four. Due to the significant difference between the time steps in the two domains, we employed a staggered coupling procedure in which the continuum domain has been described as a static region while the MD domain has been treated dynamically. The Arlequin method has been used for the static coupling of the MD to the FE domain. The information transfer between them has been realized in a coupling region which contains the above mentioned anchor points. In this region two descriptions are valid, i.e., the particle and the continuum one. The total energy is blended by a weighting factor. Atactic PS and a PS silica nanocomposite have been simulated in a coarse-grained representation to validate the new hybrid scheme. The deviations between data from the hybrid method and pure FE simulations have been computed for quantities such as reaction forces and the Cauchy stress. The sources of the observed deviations are discussed in some detail.

Finally, the fifth chapter summarizes the results obtained in this PhD work, and discusses possibilities to extend the current hybrid model to new problems such as larger deformations.

Zusammenfassung

Die Wechselwirkung zwischen einem Polymer und einer festen Oberfläche ändert die Polymereigenschaften in der Nähe der Oberfläche (der so genannten Interphase) relativ zu denen der reinen Polymerphase. Eine eindeutige Erklärung für die Ursachen dieser Änderung der Polymereigenschaften steht noch aus. Das Ziel meiner Doktorarbeit war die Untersuchung der mechanischen Eigenschaften von Nanokomposit Materialien sowie die Analyse der Polymereigenschaften in der Interphase im Fall einer strukturellen Deformation. Simulationen vom „coarse-grained“ Typ wurden an einem Modellsystem durchgeführt, das aus einem Silikat-Nanoteilchen in einer ataktischen Polystyrol (PS) Matrix besteht. In diesem Fall sind molekulare Details nur in dem kleineren Bereich der Interphase wichtig. Im restlichen Polymervolumen entsprechen die Eigenschaften denen der reinen Polymerphase und können mit den Methoden der Kontinuumsmechanik beschrieben werden. Aus diesem Grund bietet es sich an, den kleinen „interessanten“ Polymerbereich mit einem Molekular-Dynamik (MD) Ansatz zu beschreiben und den „großen Rest“ kontinuumsmechanisch zu behandeln. Um dies zu ermöglichen, haben wir eine neue Hybridmethode für Polymere entwickelt, die eine molekulare Beschreibung mit einem Ansatz der Kontinuumsmechanik kombiniert. In diesem Modell wird der zentrale Bereich einer Simulationszelle molekulardynamisch beschrieben. Er ist von einem Kontinuum umgeben, das mit einem Finite-Element (FE) Ansatz beschrieben wird. Nach meinem besten Wissen ist die vorliegende Arbeit der erste Versuch, MD und FE Methoden zur Beschreibung von Polymeren zu kombinieren. Die Entwicklung einer solchen Methode war das zentrale Ziel meiner Arbeit. Die Kopplung einer MD und einer FE Methode erfordert eine Reihe von Änderungen sowohl im MD als auch im FE Bereich (Referenz: reine MD und FE Simulation).

Die Einleitung meiner Arbeit gibt einen kurzen Überblick über bestehende Hybrid-Simulationen sowie über die Schritte, die notwendig sind, zwei Domänen zu koppeln. Die Probleme bei der Kopplung dieser Domänen werden beschrieben, ebenso der Informationstransfer zwischen ihnen sowie das Erreichen eines stationären Zustands (Equilibrierung) im Kontinuum. In diesem Teil meiner Arbeit gebe ich einen Überblick über die verschiedenen Koppel-Methoden, beschreibe ihre Vor- und Nachteile sowie Methoden, technische Probleme bei der MD-FE Kopplung zu lösen. Wie bereits angedeutet, waren diese Methoden auf Flüssigkeiten und kristalline Festkörper beschränkt. Um sie für Polymere einsetzen zu können, ist eine Reihe von Änderungen notwendig. In meiner Arbeit beschreibe ich die Probleme, die im Fall der MD-FE Kopplung in der MD Domäne auftreten sowie Ansätze zur Problemlösung. Die Änderungen, die im FE Bereich notwendig sind wurden von

Wissenschaftlern des Lehrstuhls für angewandte Mechanik der Universität Erlangen-Nürnberg durchgeführt. Die vorliegende Arbeit erforderte eine intensive Zusammenarbeit mit Ihnen, um ein modifiziertes MD Verfahren in eine FE Beschreibung zu integrieren.

Im zweiten Kapitel dieser Doktorarbeit werden die mechanischen Eigenschaften einer reinen Polystyrol-Matrix sowie einer Polystyrol-Matrix mit einem Silikat-Nanoteilchen mithilfe von MD Simulationen in einer „coarse-grained" Auflösung untersucht. Die Spannungs- Dehnungs-Kurven von Polystyrol wurden für eine Reihe von Temperaturen über- und unterhalb des Glas-Übergangs berechnet. Young-Module von Polystyrol auf Basis solcher Spannungs-Dehnungs-Kurven wurden sowohl mit experimentellen Daten als auch mit Simulationen in atomarer Auflösung verglichen. Durch ein Studium der lokalen Segment-Orientierung und der lokalen Struktur des Polymers nahe der Oberfläche der Nanoteilchen in Gegenwart einer geometrischen Deformation konnten wir zeigen, dass das Polymer hier steifer ist als in der reinen Polymerphase. Die Dicke der Interphase konnte ermittelt werden. Wir konnten zeigen, dass Young-Module der untersuchten Nonokomposit-Materialien mit zunehmendem Volumenanteil der Nanoteilchen ansteigen. Ergebnisse dieser Interphasen-Analyse in Gegenwart von räumlichen Deformationen sind wichtige Eingabe-Parameter für die FE Simulationen des vorgestellten Hybrid-Modells; dies wird im vierten Kapitel erläutert.

In den hier vorgestellten Hydrid-Simulationen können die üblichen periodischen Randbedingungen bei MD Rechnungen nicht verwendet werden, da der MD Bereich von dem FE Kontinuum umgeben ist. Deshalb haben wir einen neuen nicht-periodischen Ansatz im Rahmen stochastischer Randbedingungen (SBC) ausgearbeitet, der einen Informations-Austausch (Kräfte und Auslenkungen) zwischen beiden Domänen zulässt und Artefakte in der berechneten Dynamik minimiert. Im SBC Ensemble werden Hilfsteilchen, so genannte Ankerpunkte, in der Grenzregion zwischen MD und FE Bereich eingeführt. Diese Ankerpunkte sind harmonisch an die realen MD Teilchen gekoppelt. Sie haben eine wichtige Funktion im Informationstransfer zwischen MD und FE Bereich. Die Teilchen in der Kopplungsregion bewegen sich nach den Gesetzen einer dissipativen Teilchendynamik, um die Dissipation von Energie und die Thermostatisierung der Simulation zu ermöglichen. Das Prinzip der stochastischen Randbedingungen wird im dritten Kapitel näher erläutert. Die Leistungsfähigkeit dieser Randbedingungen bei Simulationen wurde am Beispiel von Polystyrol in einer „coarse-grained" Auflösung in Gegenwart nicht-periodischer und gewöhnlicher periodischer Randbedingungen gezeigt. Eine exzellente Übereinstimmung zwischen beiden Verfahren wurde für thermodynamische, geometrische und dynamische Eigenschaften gefunden.

Eine ausführliche Beschreibung des neuen Hybrid-Verfahrens auf Basis molekularer und kontinuumsmechanischer Ansätze ist im Kapitel vier zu finden. Aufgrund der großen Unterschiede in den Zeitschritten in beiden Domänen, MD und FE, haben wir eine „gestaffelte Kopplungsprozedur"

verwendet, in der das Kontinuum statisch, der MD Bereich aber dynamisch behandelt wird. Die Arlequin-Methode wurde für die statische Kopplung der MD und FE Bereiche verwendet. Der Informationsaustausch zwischen beiden Bereichen geschieht in einer Kopplungsregion, in der sich die bereits erwähnten Ankerpunkte befinden. In der Kopplungsregion gelten sowohl die Gesetze für MD Simulationen als auch diejenigen, die für eine Kontinuumsbeschreibung relevant sind. Die Gesamtenergie ergibt sich aus einem „Mischen“ von MD und FE Energien. Ataktisches PS sowie ein PS-Silikat Komposit wurden in einer „coarse-grained“ Auflösung simuliert, um die Leistungsfähigkeit der neuen Hybrid-Methode zu demonstrieren. Abweichungen zwischen Daten aus der Hybrid-Methode und FE Simulationen wurden für Eigenschaften wie „Reaktionskräfte“ oder „Cauchy-Spannung“ berechnet. Die Ursachen für die erhaltenen Abweichungen wurden näher erläutert.

Im fünften Kapitel dieser Doktorarbeit werden die Ergebnisse noch einmal zusammengefasst. Dabei werden Möglichkeiten diskutiert, das vorgestellte Hybrid-Verfahren für zukünftige Anwendungen zu erweitern. Stärkere Materialdeformationen sind hier nur ein Beispiel.

Table of Contents

1. Introduction

Continuum is an efficient and powerful tool in describing macroscopic phenomena. However, it fails to describe situations in the microscale, where molecular details are important. On the other hand, molecular dynamics (MD) simulations can provide such information. The performance of MD simulations in the macroscale is computationally unfeasible due to the large number of molecules. In many cases molecular details are required only in small spatial regions such as solid-fluid interfaces, while a continuum description is accurate enough in the remaining bulk region. Therefore, it is desirable to develop a hybrid simulation method to combine the efficiency of continuum mechanics with the accuracy of MD simulations. In the present context the "hybrid" refers to schemes in which the system is separated into MD and continuum region. Hybrid methods are useful to study nanodevices interacting with microscale systems. In such cases many degrees of freedoms are reduced by the continuum domain. Therefore we are able to simulate system sizes which are impossible to simulate with atomistic resolution. Hybrid methods can be employed to study such large-scale phenomena as mechanical deformation and failure of in materials. As deformation processes occur on many different length and time scales, mechanical deformations are known as multiscale phenomena. In these cases the phenomena occurring over large length scale are connected to those occurring over shorter length scale. Therefore the use of hybrid methods which can model a variety of length scales is crucial for studying such systems. The main challenge in hybrid methods is the conservation of an internal consistency in the coupling of the two a fore-cited domains. For example, it is essential to keep continues physical quantities (density, momentum, and energy) and their fluxes (for hydrodynamics methods). The consistency of physical quantities at the interface of the two domains can be obtained through exchanging boundary conditions in the overlapping region. Boundary conditions from the MD domain into the continuum domain transfer physical quantities from the MD to the continuum domain through temporal averaging. For the other direction, continuum boundary conditions into the MD domains, it requires to generate a particle configuration from macroscopic quantities. Another challenge in hybrid methods is that the continuum timescales are much larger than those at the atomistic scale. Thus a proper timescale decoupling is necessary for efficient hybrid computations. The existing hybrid schemes can be grouped into those for treating hydrodynamics problems and those for structural-mechanics problems. The two methods differ in the treatment of continuum domain and on the method of transfer of information between MD and continuum domains.

1.1. Hydrodynamical hybrid scheme

In these hybrid schemes the Navier-Stokes equations are usually adopted for modeling the fluid dynamics. These kinds of hybrid schemes are employed for simulations of liquid flows in microchannels[1–4]. Flows in microchannels have properties different from those of existence at macroscales. The main reason for these differences is the fluid-solid interactions. Therefore to simulate the flows in microchannels, we have to take into account the interaction of fluid and solid at the microscales. Continuum dynamics, on the one hand, cannot treat such interaction. On the other hand MD simulations are computationally expensive. As a result, hybrid schemes are the best methods to simulate such systems. In the hybrid simulation the solid and fluid nearby can be solved by MD, while the fluid at a sufficient large distance from the solid is treated by a continuum model. Figure 1 illustrates the channel flow modeled by hybrid schemes. The hybrid schemes for hydrodynamics can be grouped into state variable-based coupling and flux exchange-based methods.

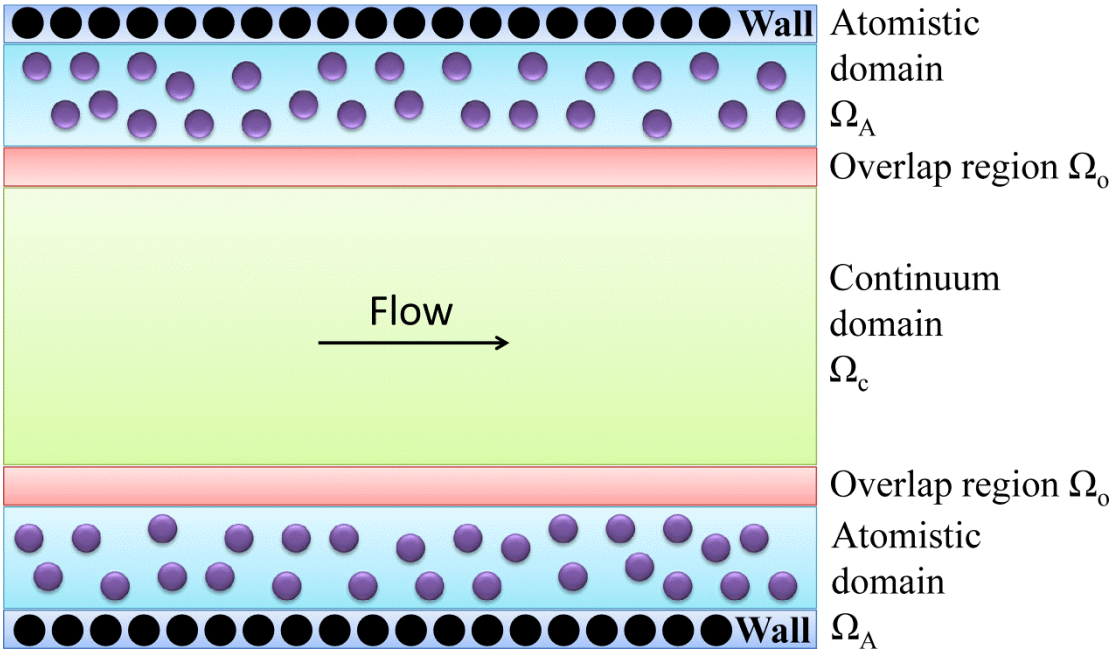

Figure 1. Schematic picture of the channel flow modeled by a hybrid scheme. The boundary conditions shown by red color define an overlap region where both methods are valid.

The state variable coupling method was first developed by O'Connell and Thompson[5]. In the proposed hybrid scheme, the atomistic domain (Ω_A) is limited to regions where molecular details are required. The continuum domain (Ω_c) has an overlap with the atomistic domain to avoid the local structures in the interface region between two domains. In the overlap region (Ω_o), both the continuum and the atomistic descriptions must be valid. In fact the Ω_o region is a communication device between Ω_A and

Ω_c. The continuity of thermodynamic and transport properties across the interface between the atomistic and continuum descriptions was validated by simulating an isothermal Couette flow[6]. To enforce momentum continuity, the total momentum of the particles in Ω_o was relaxed to that of the corresponding continuum fluid element by using a constrained dynamics. The constraint can be expressed as $\sum_{i=1}^{N} \boldsymbol{p}_i - M\boldsymbol{u} = 0$, where N is the total number of particles, $\boldsymbol{p}_i$ the momentum of particle i, M and $\boldsymbol{u}$ the continuum mass and velocity of the fluid element for the overlapping N particles. The limitation of this model is that the continuum and the MD domains have a common timescale. To overcome this problem, Hadjiconstantinou et al. developed a model for an incompressible flow which is able to transfer the mass flow across the interface and allows the decoupling of timescales between the evolution of the continuum and the MD solutions[7]. Using a particle reservoir, mass can be transferred across the interface of the two domains. To deal with different timesteps, the solution of one domain provides boundary conditions to the other domain via Ω_o, and vice versa. This process is repeated until the solutions in Ω_o are matched. Therefore, each domain can proceed on different timescales. Later this model was modified to improve the description of the atomistic structure of the fluid as well as the details in the microscopic physics[8].

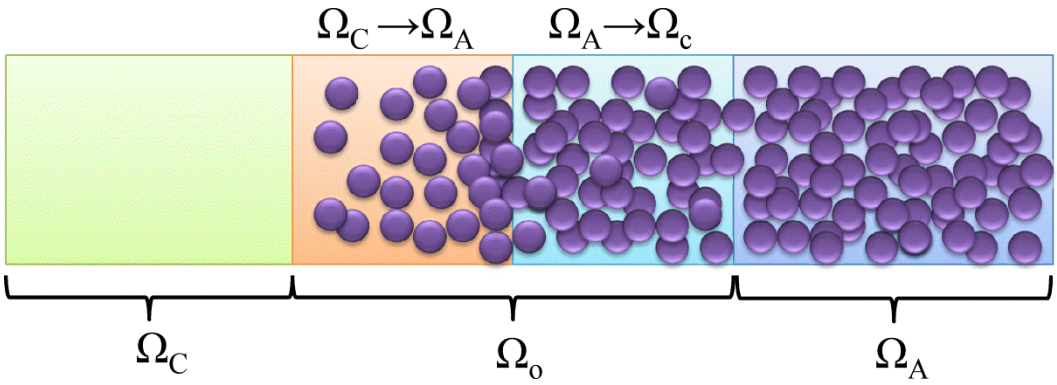

Figure 2. Schematic picture of the flux exchange coupling method. There are three regions atomistic: Ω_A, continuum Ω_c and overlap region Ω_o. The overlap region is subdivided into $\Omega_c \rightarrow \Omega_A$ and $\Omega_A \rightarrow \Omega_c$.

A flux exchange coupling method was developed first by Flekkøy et al[9]. In this method one has a flux exchange between domains instead of having an exchange of state variables as realized in the previous method. Therefore, instead of an equation of state conservation laws for the direct exchange of fluxes are used. Also in this method Ω_A and Ω_c overlap within Ω_o. The Ω_o region is divided into two regions $\Omega_c \rightarrow \Omega_A$ and $\Omega_A \rightarrow \Omega_c$ as shown in figure 2. In the $\Omega_c \rightarrow \Omega_A$ cell, continuum fluxes are imposed on the particles, whereas in the $\Omega_A \rightarrow \Omega_c$ cell, the opposite is carried out. The time average of mass and

momentum flux densities of the particles in the $\Omega_A \rightarrow \Omega_c$ region is simply obtained to replace the continuum flux. The replacement of the particle flux by the continuum flux proceeds as follows:

Mass flux ($\Omega_A \rightarrow \Omega_c$): $\frac{1}{V} < \sum_i m\boldsymbol{v}_i > . \boldsymbol{n} \rightarrow \rho \boldsymbol{u} . \boldsymbol{n}$

Momentum flux ($\Omega_A \rightarrow \Omega_c$): $\frac{1}{V} < \sum_i \boldsymbol{v}_i \boldsymbol{v}_i - \frac{1}{2} \sum_{i \neq j} \boldsymbol{F}_{ij} \boldsymbol{r}_{ij} > . \boldsymbol{n} \rightarrow \boldsymbol{\Pi} . \boldsymbol{n}$

In the two equations i is the particle number, m and $\boldsymbol{v}_i$ its mass and velocity, V the volume, $\boldsymbol{u}$ the velocity of the continuum and $\boldsymbol{F}_{ij}$ the interaction force between particles i and j which are separated by $\boldsymbol{r}_{ij}$. $\boldsymbol{\Pi}$ is the momentum flux tensor and ρ the mass density. The unit vector $\boldsymbol{n}$ is normal to the cell face. The averaging <…> is taken over the continuum timestep. The expression for the flux exchange between Ω_c to Ω_A is given by:

Mass flux ($\Omega_C \rightarrow \Omega_A$): $A\rho \boldsymbol{u} . \boldsymbol{n} \rightarrow ms$

Momentum flux ($\Omega_C \rightarrow \Omega_A$): $A(\rho \boldsymbol{u}\boldsymbol{u} + \boldsymbol{\Pi}) . \boldsymbol{n} \rightarrow ms < \boldsymbol{v}' > + < \sum_i \boldsymbol{F}_i >$

Here s is the number of particles added to the cell per time unit via the continuum mass in flow, A is the cell cross sectional area, $\boldsymbol{v}'$ the velocity of the introduced particles, and $\boldsymbol{F}$ an external force acting on the particles, time averaged over the continuum timestep. It is shown that the last equation is satisfied when: $< \boldsymbol{v}' > = \boldsymbol{u}$ and $\sum_i \boldsymbol{F}_i = A(\boldsymbol{\Pi} - \rho \boldsymbol{u}\boldsymbol{u}) . \boldsymbol{n}$. In the $\Omega_C \rightarrow \Omega_A$ cell the force acting on the introduced particles drive them towards Ω_A. This method had been extended by Delgado-Buscalioni to include an energy flux transfer[10].

In the hybrid simulations both coupling methods, flux and state variable couplings, can be used simultaneously as long as both domains are consistent. In fact, the boundary conditions contain two parts, $\Omega_A \rightarrow \Omega_c$ and $\Omega_c \rightarrow \Omega_A$. Each part can be modeled of the two coupling methods, and therefore there are four different coupling schemes. The stability and convergence rate of these four coupling methods were studied analytically and numerically. It was shown that static coupling in the $\Omega_A \rightarrow \Omega_c$ boundary conditions has the best performance for static and dynamic cases[11]. For the $\Omega_C \rightarrow \Omega_A$ boundary conditions flux coupling was recommended since the convergence rate does not depend on the size of the overlap region[11]. However it should be mentioned that imposing continuum data onto discrete MD domain, with a larger number of degrees of freedom, is still a challenge with no unique solution. Another challenge is to develop a hybrid method with an arbitrary shape of the MD domain. This will allow the simulation of flows in more complex geometries. In this regards an excellent recent review of hydrodynamical hybrid schemes has been given by Mohamed[12].

1.2. Structural-mechanical hybrid scheme

Structural-mechanical hybrid models have been employed for simulations of crystalline solids. A finite element (FE) description is usually adopted to describe the continuum domain. Structural-mechanical hybrid models have the potential to predict and to analyze the material failure[13–17]. In fact the mechanical deformation and failure of solids are multiscale phenomena which happen in various time and length scales. For instance, the breaking of chemical bonds can be explained by quantum mechanics, while the atom displacement and dissipation of energy can be modeled by MD. In the far length scale, the stress and strain which refer to an average over all length scales can be described by FE. The physically most meaningful method to study the failure is quantum mechanics. However, it is impossible to simulate the failure with quantum mechanical details due to the limitation in the computational time. At atomic scale, MD is capable to simulate the mechanical deformation and failure[18]. However, many systems of interest involve too many atoms and therefore it is too expensive to simulate them with atomistic details. At a very large scale, it is very difficult to describe the complex phenomena such as the crack propagation via FE[19]. Therefore, hybrid schemes are the best approaches to simulate the failure. They require fewer degrees of freedom relative to an equivalent full atomistic simulation without scarificing any information in the area of interest. Another capability of hybrid schemes is to study the contact area evolution of rough surfaces under normal loading[20]. In most hybrid schemes, MD is employed in the interesting area like crack, whereas the surrounding FE domain provides the correct boundary conditions for the MD part.

In structural-mechanical hybrid methods the system is divided into three regions Ω_A, Ω_c and Ω_o . Region Ω_A is treated atomistically, while region Ω_C is modeled as a continuum in a finite element description. The interface region between Ω_A and Ω_C is defined by Ω_o where both an atomistic and a finite element picture are valid. The key differences between the different hybrid methods lie in the way they handle the interface region and the method to find the equilibrium. In most methods the interface region is subdivided into a handshake region and a padding region. In the handshake region there is some degree of mixing between the two descriptions of the material. The treatment and the thickness of the handshake region depend on the method adopted. The padding region refers to a continuum domain that contains atoms to provide the boundary conditions for the atoms in the handshake region. Therefore the thickness of the padding region corresponds to the cutoff distance. This is illustrated in figure 3. The motion of the atoms in this region is determined by the continuum displacement fields at the position of the padding atoms. Since there is a significant difference in the timescales of the two domains, coupling both domains dynamically is impossible. However, there are

some efforts to couple real MD to FE descriptions for a one dimensional toy system with a time scale discrepancy of ten to twenty orders of magnitude[21]. Since it is impossible to couple real MD to FE due to a large difference in the timescale, approaches that artificially enhance the dynamics of the MD part are employed[22]. An enhancement of the dynamics can be achieved by performing simulations at high loads, high temperature or with an artificial potential. The resulting information should be examined with real conditions. Here we focused only on the methods which MD domain is treated statistically since they are less complicated. For static methods, there are two different approaches to find the equilibrium, i.e. an energy-based and a force-based approach.

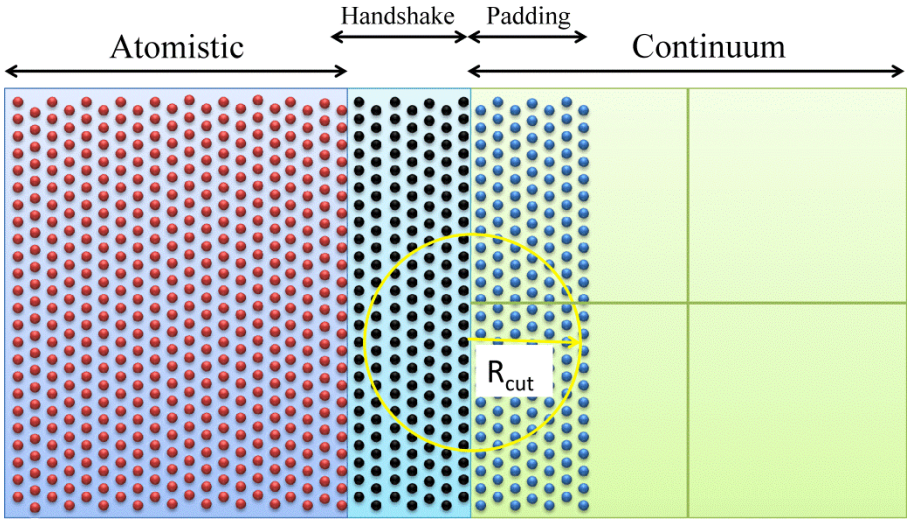

Figure 3. Schematic picture of a structural-mechanical hybrid scheme. Regular atoms are shown as red circles, handshake atoms as black and padding atoms as blue. The thickness of padding region is equal to the cut-off radius.

In an energy-based formulation, the total potential energy can be written as the sum of the potential energy of the three subdomains. In the continuum and the atomistic domains the calculation of the potential energy is straightforward. But in the handshake region, the energy refers to a blend of atomistic- and continuum-based energies. The contributions of the continuum and atomistic energies are weighted according to a weighting function. It is worth mentioning that in this model the energy of the atoms in the padding region is not taken into account. In fact the padding region is inside the continuum region and it only provides the boundary conditions for the atoms in the handshake region. The total potential energy is then minimized under the boundary conditions to obtain the equilibrium configuration of the system. The continuum energy density is only an approximation to the atomistic energy density. Therefore the derivative of the continuum energy is not equal to the derivative of the atomistic energy. This problem leads to errors known as ghost forces. Even if all atoms are at an

energy equilibrium, there are still residual ghost forces acting on them[23]. All methods based on energy minimization suffer from this error. One of the most famous and popular energy-based method is the quasicontiuum method[24].

Force-based methods were developed to eliminate ghost forces. As a matter of fact, all forces are equal to zero in these methods when a perfect crystal is in its correct equilibrium state. Here the forces on all degrees of freedom are calculated to reach equilibrium by driving them towards zero. While it might seem that the two methods are identical, they actually are not. Forces in force-based methods are calculated by postulating that two independent potential energy functionals exist: One treating the entire system atomistically and one treating the entire system as a continuum. For the atomistic description, atoms positions in the continuum region are determined by knowing reference crystal structure and the displacement field of the finite elements. To calculate the force on each atom, first the potential energy of the atomic configuration E_{atom} is computed. Then the derivative of the potential energy with respect to the position of any atom leads to the force on the atom. For the finite element description, the whole body is modeled by a finite element with the same elements as defined for the coupled system. This is obtained by knowing the positions of the atoms and defining the displacement for the elements. Since the force on each FE node is obtained from elements in direct contact with the node, knowledge of the position of the elements near the interface of two domains is enough to calculate the force. In general the force on each atom in this model is defined as $f_i = \frac{\partial E_{atom}}{\partial r_i}$ where r_i is the position of atom *i*, while the force on each node defined as $f_i = \frac{\partial E_{FE}}{\partial u_i}$ where u_i is the position of FE node *i*. This is clearly not the same as minimizing the combined energy which $E=E_{atom}+E_{FE}$. The evaluation of equilibrium positions in this model is more difficult than in the previous method[25–27]. Although in this scheme ghost forces do not appear, some spurious effects that are similar to ghost forces were observed[25–27].

Apart from different choices to equilibrate the systems, hybrid methods differ in the way defining coupling or boundary conditions. The coupling between a continuum and an atomistic region requires conditions which allow the transfer of displacements between them. In the strong coupling method, padding atoms are constrained to move with element nodes as though they were glued to the finite elements. The disadvantage of this method is that the generation of a mesh file near the interface is very difficult since the mesh must be refined completely. Furthermore it must be consistent with the underlying atomistic configuration. To avoid these problems some approaches make use of a weak coupling method where displacements of the boundary conditions are imposed only in some average sense or with some type of penalty function[28]. These methods are less accurate than the previous ones.

So far many methods have been developed based on the energy-based and force-based techniques[29–31]. However, it is very difficult to understand the similarities, differences and weaknesses of the various schemes. It is also hard to quantify the relative accuracy and efficiency of these methods. Recently Miller and Tadmor have performed test simulations to study the accuracy and the efficiency of fourteen different methods[31]. It was observed that the energy-based methods converge faster than the force-based methods. But the force-based methods are more accurate than energy-based methods due to the ghost force problem. The handshake region and weak coupling methods make hybrid methods slower and less accurate. However, these two features are appealing because they make the mesh generation easier. As a result it is very difficult to find the optimum hybrid scheme. There are some efforts to analyze and improve the accuracy of energy-based methods and to increase the convergence rate of force-based methods[32,33]. For example, a ghost-force corrected quasicontinuum method has been developed by Sheny et. al[34]. In this method the ghost forces are approximately calculated and proposed to the original quasicontinuum method which is an energy-based method. Interestingly, It was found that this correction makes the method faster than the original quasicontinuum description. However, developing an optimized method which can be easily implemented in three dimensions is still a big challenge.

1.3 A hybrid scheme for structural mechanics of polymer materials

Polymers are an important class of materials which are widely used in industry. Among their unique behavior, mechanical properties of polymers have attracted a lot of interest. Mechanical properties of polymers have been investigated at different length scales. For example, at an atomistic scale Lyulin et al. have employed molecular dynamics to study mechanical properties of polystyrene[35]. At a larger length scale, i.e. a coarse-grained scale, the mechanical properties of polystyrene have been investigated near a silica nanoparticle surface[36]. An excellent recent review of simulation techniques to predict the mechanical behavior of amorphous polymers at different length scale has been given by Bouvard et al[37]. However, there is still an absence of hybrid schemes to study the deformation of polymers at a multiscale level. All of the structural-mechanical hybrid schemes have been limited to crystalline materials with regular atomic conformations and space fixed-atoms. The complex random structures of amorphous polymers make the coupling in the handshake region very difficult.

To the best of our knowledge the only effort to develop a hybrid scheme for polymers is the one by Bian et al very recently[38]. In this work, polymers in the MD domain have been modeled at the coarse grained level. The amorphous cell method has been used to generate the MD configurations[39]. The

initial configuration of one chain has been generated in a main cell, and then the configuration has been equilibrated by a conjugate gradient method. The MD domain has been produced by copying the main cell according to the boundary conditions. It should be mentioned that the MD configuration and therefore the hybrid scheme has been modeled in two dimensions. For the FE domain, they have generated a mesh file where the size of each element was exactly the same as the MD cell. Two domains have been coupled in the handshake region in the way that each FE element in the handshake region was exactly fitted to the one MD cell. A mapping relation has been defined to map the displacement of four nodes of an element to particles in the corresponding MD cell. Therefore, a deformation of the FE domain can be transferred to the MD domain via the mapping relation in the handshake region. A deformation can also be transferred from the MD domain to the FE domain by reverse mapping. After each load step the conjugate gradient method has been used to obtain the equilibrium configuration. This method has been employed to study the fracture of polymers.

Although Bian et al. have developed the first hybrid scheme for polymers, the MD domain of their method is completely unrealistic. First of all, many properties of polymers can be modeled only in three dimensions such as entanglement which has important effects on mechanical properties. They might have limited the simulation to two dimensions because in three dimensions the finding of mapping relations between six nodes and particles inside the element is more complicated than in two dimensions. Secondly, the configuration of polymers in the MD domain cannot model the amorphous polymers since it has been generated by copying the main cell according to periodic boundary conditions. This method has been employed to generate the initial configuration in order to have the same number of particles in each element in the handshake region and simply defining the mapping relation between MD particles and FE nodes. For real amorphous polymers, an identically replicated distribution of particles in all elements is impossible. In addition, the configuration of particles in each element will be different which makes very hard or even impossible to define a mapping relation. Thirdly, the method employed to equilibrate the MD domain, i.e. the conjugate gradient method, does not depend on time, and therefore, it is not a real MD model. Using real MD might cause the diffusion of polymers and therefore polymers will move outside the MD domain. Finally, in this model the absence of the padding region is very clear. The particles in the handshake region cannot behave like bulk particles since they are in contact with vacuum. This modifies the properties of polymer in the handshake region and it might affect the polymer properties in the center of the MD domains. In fact defining a region like the padding region for amorphous polymers is very difficult due to the irregular configuration of polymers.

As it was explained here the coupling of a real MD to the FE domain is a very challenging task and many technical difficulties in both domains should be solved to couple the real MD to FE. The main purpose of the present work has been the extension of a structural-mechanical hybrid scheme to polymers with their irregular particle arrangement.

1.4 A hybrid scheme for nanocomposite materials

Polymer materials have extraordinary properties such as light weight, light transparence, and low cost. Their mechanical properties, however, are poor compared to metals, and therefore need to be improved for industrial purposes. Reinforcement of polymers with nanoparticles, so-called nanocomposites, can improve the mechanical properties of polymers. Parameters such as dispersion, length, size and orientation of nanofillers affect the nanocomposite properties. Controlling these parameters to achieve the best properties of a nanocomposite is the main challenge in the nanocomposite field. Quantifying the influence of parameters at the nanoscale is experimentally very difficult. Therefore simulation techniques can be very useful to answer many unsolved questions. For example, it was proved that the mobility of nanoparticles is enhancing the toughness of nanocomposites[40]. For nanotubes as fillers, the mechanical properties of nanocomposites significantly depend on the direction of nanotubes with respect to the deformation direction and the length of the nanotube[41,42]. It was found that there is an optimum filler volume fraction for rubber reinforcement with attractive polymer-filler interaction[43]. There are some excellent reviews about simulation achievements in nanocomposite field[44–46].

Recent studies have shown that nanocomposite properties can be enhanced by switching the filler size from micro- to nano-scale at the same volume fraction[47,48]. This has guided the attentions to the region near the nanoparticle surface, the so-called interphase. The size of the interphase region usually is in order of nanometers. Polymer properties in the interphase are completely different from those of the bulk polymer. The interaction of a nanoparticle surface with polymers organizes the polymers into layers around the nanoparticles and also slows down the mobility of chains[49–51]. This local modification of the polymer structure and behavior is one main reason for the new properties of nanocomposites which cannot be estimated additively from polymer and filler properties. As a result, a large range of length scales is involved in macroscopic properties of nanocomposites. This clearly shows a need for an approach to integrate different modeling methods.

The FE method is a very popular simulation technique due to its flexibility in geometry, refinement and loading conditions. The FE method, however, is not capable of modeling system at length scales of microns and nanometers. At these length scales, physical quantities such as stress, density and

temperature lose their meaning. In addition, the fundamental assumption of continuum mechanics which relies on the continuous and homogeneous description of materials is not valid any more. MD simulations, on the other hand, are able to simulate at the nanometer scale or less. Nevertheless, nonocomposite materials usually contain too many particles to be simulated by MD. Therefore, modeling the nanocomposite materials and the study of the interphase can only be achieved through concurrent coupling of MD and FE. This will reduce the number of degrees of freedom for this extremely large system size. In the coupling method for nanocomposite materials the system should be decomposed into MD and FE regions. The nanoparticles and the interphase region should be represented by MD, while the polymer with bulk properties can be modeled in the FE framework.

As it was mentioned before, mechanical deformation and failure are multiscale phenomena, and therefore hybrid schemes are the best approach to study them. The importance of hybrid schemes is more obvious when we want to study the mechanical properties of nanocomposites. The hybrid scheme can quantify the size and the behavior of polymers in the interphase region under deformation. Calculating these parameters with other simulation techniques is very difficult or even impossible. The simulation of nanocomposites with hybrid scheme might help to answer some unsolved questions. For example, adding nanoparticles to polymers enhances the mechanical properties but makes the polymers more fragile and brittle[52]. To understand the reason we can perform a hybrid scheme simulation. Here the nanoparticles and enough polymers are treated by MD, while the rest of the system is described by FE. Then the deformation should be applied to the system and then quantities such as the position of failures and their propagation can be analyzed.

References

(1) Bugel, M.; Galliéro, G.; Caltagirone, J.-P. *Microfluidics and Nanofluidics* **2010**, *10*, 637-647.

(2) Yen, T. H.; Soong, C. Y.; Tzeng, P. Y. *Microfluidics and Nanofluidics* **2007**, *3*, 665-675.

(3) Cui, J.; He, G.; Qi, D. *Acta Mechanica Sinica* **2006**, *22*, 503-508.

(4) Nie, X. B.; Chen, S. Y.; E, W. N.; Robbins, M. O. *Journal of Fluid Mechanics* **2004**, *500*, 55-64.

(5) O'Connell, S.; Thompson, P. *Physical Review E* **1995**, *52*, R5792-R5795.

(6) Koplik, J.; Banavar, J. R. *Annual Review of Fluid Mechanics* **1995**, *27*, 257-292.

(7) Hadjiconstantinou, N. G.; Patera, A. T. *International Journal of Modern Physics C* **1997**, *8*, 967-976.

(8) Li, J.; Liao, D.; Yip, S. *Physical Review E* **1998**, *57*, 7259-7267.

(9) Flekkøy, E. G.; Wagner, G.; Feder, J. *Europhysics Letters (EPL)* **2000**, *52*, 271-276.

(10) Delgado-Buscalioni, R.; Coveney, P. *Physical Review E* **2003**, *67*, 046704.

(11) Ren, W. *Journal of Computational Physics* **2007**, *227*, 1353-1371.

(12) Mohamed, K. M.; Mohamad, A. A. *Microfluidics and Nanofluidics* **2009**, *8*, 283-302.

(13) Moseley, P.; Oswald, J.; Belytschko, T. *International Journal for Numerical Methods in Engineering* **2012**, *online*, DOI: 10.1002/nme.4358.

(14) Aubertin, P.; Réthoré, J.; de Borst, R. *International Journal for Numerical Methods in Engineering* **2009**, *81*, 72-88.

(15) Gracie, R.; Belytschko, T. *International Journal for Numerical Methods in Engineering* **2009**, *78*, 354-378.

(16) Park, H. S.; Karpov, E. G.; Liu, W. K.; Klein, P. A. *Philosophical Magazine* **2005**, *85*, 79-113.

(17) Shilkrot, L. E.; Curtin, W. A.; Miller, R. E. *Journal of the Mechanics and Physics of Solids* **2002**, *50*, 2085-2106.

(18) Zhou, S.; Lomdahl, P.; Thomson, R.; Holian, B. *Physical Review Letters* **1996**, *76*, 2318-2321.

(19) Belytschko, T.; Gracie, R.; Ventura, G. *Modelling and Simulation in Materials Science and Engineering* **2009**, *17*, 043001.

(20) Anciaux, G.; Ramisetti, S. B.; Molinari, J. F. *Computer Methods in Applied Mechanics and Engineering* **2012**, *205-208*, 204-212.

(21) Xiaoa S. P.; Belytschko T. *Computer Methods in Applied Mechanics and Engineering* **2004**, *193*, 1645-1669.

(22) Baker, K. L.; Warner, D. H. *Modelling and Simulation in Materials Science and Engineering* **2012**, *20*, 065005.

(23) Dobson, M.; Luskin, M. *Mathematical Modelling and Numerical Analysis* **2009**, *43*, 591-604.

(24) Shenoy, V.; Miller, R.; Tadmor, E.; Phillips, R.; Ortiz, M. *Physical Review Letters* **1998**, *80*, 742-745.

(25) Luan, B.; Hyun, S.; Molinari, J.; Bernstein, N.; Robbins, M. *Physical Review E* **2006**, *74*, 1-11.

(26) Parks, M. L.; Bochev, P. B.; Lehoucq, R. B. *Multiscale Modeling Simulation* **2008**, *7*, 362-380.

(27) Shilkrot, L. E.; Miller, R. E.; Curtin, W. A. *Journal of the Mechanics and Physics of Solids* **2004**, *52*, 755-787.

(28) Wagner, G. J.; Liu, W. K. *Journal of Computational Physics* **2003**, *190*, 249-274.

(29) Curtin, W. A.; Miller, R. E. *Modelling and Simulation in Materials Science and Engineering* **2003**, *11*, R33-R68.

(30) Weinan E; Bjorn Engquist; Xiantao Li; Weiqing Ren; Eric Vanden-Eijnden *Communications in Computational Physics* **2007**, *2*, 367–450.

(31) Miller, R. E.; Tadmor, E. B. *Modelling and Simulation in Materials Science and Engineering* **2009**, *17*, 053001.

(32) Lu, J.; Ming, P. *http://arxiv.org/abs/1102.2523* **2011**, (in press).

(33) Chen, J.; Ming, P. *http://arxiv.org/abs/1205.6107* **2012**, (in press).

(34) Shenoy, V. B.; Miller, R.; Tadmor, E. b.; Rodney, D.; Phillips, R.; Ortiz, M. *Journal of the Mechanics and Physics of Solids* **1999**, *47*, 611-642.

(35) Lyulin, A. V.; Balabaev, N. K.; Mazo, M. A.; Michels, M. A. J. *Macromolecules* **2004**, *37*, 8785-8793.

(36) Rahimi, M.; Iriarte-Carretero, I.; Ghanbari, A.; Böhm, M. C.; Müller-Plathe, F. *Nanotechnology* **2012**, *23*, 305702.

(37) Bouvard, J. L.; Ward, D. K.; Hossain, D.; Nouranian, S.; Marin, E. B.; Horstemeyer, M. F. *Journal of Engineering Materials and Technology* **2009**, *131*, 041206.

(38) Bian, J.; Wang, G. *Computational Materials Science* **2012**, *57*, 8-13.

(39) Theodorou, D. N.; Suter, U. W. *Macromolecules* **1985**, *18*, 1467-1478.

(40) Gersappe, D. *Physical Review Letters* **2002**, *89*, 058301.

(41) Frankland, S. *Composites Science and Technology* **2003**, *63*, 1655-1661.

(42) Griebel, M. *Computer Methods in Applied Mechanics and Engineering* **2004**, *193*, 1773-1788.

(43) Liu, J.; Wu, Y.; Shen, J.; Gao, Y.; Zhang, L.; Cao, D. *Physical chemistry chemical physics : PCCP* **2011**, *13*, 13058-69.

(44) Allegra, G.; Raos, G.; Vacatello, M. *Progress in Polymer Science* **2008**, *33*, 683-731.

(45) Liu, J.; Zhang, L.; Cao, D.; Wang, W. *Physical Chemistry Chemical Physics* **2009**, *11*, 11365-84.

(46) Zeng, Q. H.; Yu, A. B.; Lu, G. Q. *Progress in Polymer Science* **2008**, *33*, 191-269.

(47) Kumar, S. K.; Krishnamoorti, R. *Annual review of chemical and biomolecular engineering* **2010**, *1*, 37-58.

(48) Schadler, L. *Nature materials* **2007**, *6*, 257-8.

(49) Ghanbari, A.; Ndoro, T. V. M.; Leroy, F. D.; Rahimi, M.; Böhm, M. C.; Müller-Plathe, F. *Macromolecules* **2012**, *45*, 572-584.

(50) Ndoro, T. V. M.; Böhm, M. C.; Müller-Plathe, F. *Macromolecules* **2012**, *45*, 171–179.

(51) Ndoro, T. V. M.; Voyiatzis, E.; Ghanbari, A.; Theodorou, D. N.; Böhm, M. C.; Müller-Plathe, F. *Macromolecules* **2011**, *44*, 2316-2327.

(52) Kontou, E.; Anthoulis, G. *Journal of Applied Polymer Science* **2007**, *105*, 1723-1731.

2. Mechanical behavior and interphase structure in a silica - polystyrene nanocomposite under uniaxial deformation*

2.1 Abstract

The mechanical behavior of polystyrene and a silica–polystyrene nanocomposite under uniaxial elongation has been studied using a coarse-grained molecular dynamics technique. The Young's modulus, the Poisson ratio and the stress-strain curve of polystyrene have been computed for a range of temperatures, below and above the glass transition temperature. The predicted temperature dependence of the Young's modulus of polystyrene is compared to experimental data and predictions from atomistic simulations. The observed mechanical behavior of the nanocomposite is related to the local structure of the polymer matrix around the nanoparticles. Local segmental orientational and structural parameters of the deforming matrix have been calculated as a function of distance from nanoparticle's surface. A thorough analysis of these parameters reveals that the segments close to the silica nanoparticle's surface are stiffer than those in the bulk. The thickness of the nanoparticle-matrix interphase layer is estimated. The Young's modulus of the nanocomposite has been obtained for several nanoparticle volume fractions. The addition of nanoparticles results in an enhanced Young's modulus. A linear relation describes adequately the dependence of Young's modulus on the nanoparticle volume fraction.

2.2 Introduction

The mixture of nanoparticles and a polymer matrix, so-called nanocomposites, can show dramatically improved properties in comparison to the pure polymer[1]. For instance, carbon black has been used for many years in industry to enhance the mechanical properties of rubber[2]. Although nanocomposites inherit properties from their parent materials, they can also exhibit new properties not found in the parent constituents. Therefore, new materials with novel properties or novel combinations of properties can be prepared by combining nanoparticles with a polymer matrix. The search for materials with optimized quantities for different applications has generated significant attention in nanocomposite materials. The behavior of nanocomposites depends not only on the properties of their components but

*Rahimi, M., Iriarte-Carretero, I., Ghanbari, A., Böhm, M. C., & Müller-Plathe, F. (2012). *Nanotechnology* 23, 305702.

also on their morphology and interfacial characteristics[3,4,5]. The polymer in the interphase, i.e. the region near the nanoparticle surface, often has completely different properties to the bulk polymer. This local modification of the polymer structure and behavior is one main reason for the new properties of nanocomposites[6,7,8], and, in particular, for the fact that nanocomposite properties often cannot be combined additively from polymer and filler properties. In spite of the all efforts to study the effect of the interphase on the properties of nanocomposites, there are still many open questions.

Computer modeling and simulation is a powerful tool which can answer many unsolved questions at the molecular level, therefore helping to design and to predict nanocomposite properties. Below we will summarize some of the computer simulations and theoretical approaches which have been employed to understand nanocomposite materials. Smith et al.[9] simulated spherical nanoparticles surrounded by a generic bead-spring polymer melt. They found that the more attractive the nanoparticle-polymer interaction is, the more homogenous is the dispersion of the nanoparticles in the melt. Brown et al.[10] showed that nanoparticles force the polymer into a layered structure near the surface. They pointed out that the polymer chains align with the surface of the nanoparticle. In another work by the same authors, it has been shown that the thickness of the interphase does not depend on the size of the spherical nanoparticles. This differs from the chain mobility which strongly depends on the nanoparticle geometry. Recent work of this group has shown that relaxations time for the polymer depend on the nanoparticle size[11]. To increase the influence of the interphase for a fixed volume fraction of the filler units, one can decrease the size of the nanoparticles[12]. Gersappe[13] found that the mobility of nanoparticles is the key point to enhance the toughness of nanocomposites. The energy dissipation process during the deformation of materials increases the toughness and this energy dissipation is a result of the mobility of the nanoparticle. It was shown that for a nanotube as a filler, the direction of the nanotube with respect to the deformation direction and the length of the nanotube have a significant influence on the mechanical properties[14,15]. Liu et al. [16] have studied the microscopic mechanism of polymer reinforcement. They found an optimum filler volume fraction for rubber reinforcement with attractive polymer-filler interactions. The effect of the rubber-filler interaction and the temperature on stress strain curves have been studied too. In another work Liu et al. [17] have analyzed the polymer-filler interfacial structure, as well as the dynamic and mechanical properties by coarse grained simulations. Also the Monte Carlo method has been used to study nanocomposite materials. For example, Papakonstantopoulos et al. [18] calculated the elastic modulus of a nanocomposite by measuring the thermal fluctuations of the internal stress. They have shown that the

Young's modulus of the nanocomposite is higher than that of the pure polymer. They have also obtained the local elastic modulus in the vicinity of the nanoparticle. These efforts have been reviewed in references[19,20,21].

Recently Ndoro et al. [22] have simulated a silica nanoparticle embedded in polystyrene at the atomistic level. The structure of the polymer in the immediate neighborhood of spherical nanoparticles with different diameters has been investigated. The results show that the silica nanoparticle organizes the polymers into layers. By analyzing the radius of gyration it was found that polymer chains extend near the nanoparticle. In addition, it was found that polymer chains are oriented parallel to the nanoparticle surface. In another work by the same authors, the chain dynamics of the polymer in the interfacial region surrounding a spherical nanoparticle have been investigated by MD simulations at the atomistic level [11]. The autocorrelation of intramolecular vectors (C-H bond vector, three monomers segment, and the end-to-end vector) has been investigated. With these data, the relaxation times have been computed as a function of the separation from the surface. It was shown that the dynamics of polymer near the surface is slower than in the polymer bulk. Using these atomistic trajectories Rahimi et al.[23] developed coarse grained potentials for the silica-polystyrene system. The simulations have been performed for different chain lengths to study how much the structure of the polymer interphase is length dependent. It has been shown that the interphase dimension does not depend on the length of the matrix chains. The same local behavior that had been observed for short atomistic chains was observed for long chains in a coarse grained scale. In the same work it has been shown that the size of the interphase varies according to the structural element being examined. In contrast to the local structure, the structure of entire polymer chains (radius of gyration and orientation with respect to the surface) and its variation as a function of the distance from the nanoparticle depends strongly on the chain length.
Since one main reason of adding nanoparticles to a polymer is to improve the mechanical properties, in this work we have studied the mechanical properties of the silica-polystyrene system at the coarse grained scale. We have chosen a coarse grained model because simulations of nanoparticle surrounded by polymers at the atomistic scale are prohibitively expensive. This system was also interesting for experimentalists: Kontou et al.[24] have studied its mechanical properties and found that a silica weight fraction of 4% is the optimum for the enhancement of the mechanical properties. In this work, we aim to study the effect of nanoparticles on mechanical properties and also to analyze the orientation of polymer chains under deformation, especially in the interphase. Then by analyzing these data we aim to calculate the thickness of the interphase under deformation. In the first part we calculated the mechanical properties (Young's modulus and Poisson ratio) at different temperatures, below and

above the glass transition. By comparing the results with atomistic and experimental data we found an empirical scaling factor to scale the Young's modulus obtained from the coarse-grained simulation. In the next step, we applied deformations to a system containing one nanoparticle and analyzed the deformation and orientation of polymer chains as a function of distance from the surface. It will be shown that, in the interphase region, the deformation of the polymer is completely different to that of the bulk polymer. At the end, by adding more nanoparticles to the polymer, we observed that the Young's modulus of the nanocomposite increases linearly. It is out-explanatory that this setup only allows prediction on nanocomposites with homogeneously distributed nanoparticles in low concentration. Recent experiment progress to generate such materials have been described in the litrature[25].

2.3 Model and simulation algorithm

In this contribution one or several spherical bare silica nanoparticles (NPs) embedded in atactic polystyrene (PS) are simulated to study the influence of NP on PS under deformation. Since we have performed the simulations at the coarse-grained (CG) scale, we will briefly explain the CG method used for this system. The details of the system in atomistic and CG resolution and the development of the force field are described elsewhere[26,22,23]. The nonbonded interactions are described with a tabulated potential obtained by Iterative Boltzmann Inversion (IBI) from the corresponding atomistic radial distribution functions. The IBI method optimizes the CG potential to reproduce atomistic structural distribution. The force field was developed at 590 K and 1 atm. In the mapping scheme each monomer in PS is represented by one superatom placed at its center of mass. Two different bead type are defined for the *R* and *S* enantiomers found in atactic PS. This mapping scheme has developed originally by Qian et al.[26] for pure PS. Comparing the density between pure PS with this potential and atomistic PS for short chains (20 mer) shows an error of only 0.2% at 590 K.

The strategy for the silica NP was slightly different[22,23]. The atomistic silica NP was constructed from a lattice of crystalline silica by deleting the atoms beyond the radius of NP. Dangling bonds of surface oxygen atoms were saturated with hydrogen. The CG model of silica places one superatom at the position of every Si atom. Thus, a superatom formally corresponds to a SiO_2 unit. The surface hydrogens are not accounted in the mapping scheme. The size of the NP in all simulations is constant, with 873 CG superatoms and a radius of 2 nm. It has been found that for a faithful description of the silica-PS interaction, different interaction potentials of its core and surface beads with the polymer

have to be chosen. The surface beads of the NP have the dominant contribution to the interaction with the polymer matrix, in comparison to core ones. Thus, the surface beads are more attractive than the core beads. CG potentials obtained with these mapping schemes are able to reproduce the atomistic structure and they are also transferable between systems of different NP sizes and chain lengths. The same interaction potential between polymer beads which was developed for pure PS was also used for the system with one or more NPs embedded in PS. All of the initial configurations in this work were generated by the method which has been developed in our previous study[23]. In this method, a self-avoiding random walk was used as the initial configuration of PS. Firstly, the structure of the NP is placed the simulation box and then the polymer chains are generated randomly monomer-by-monomer. During the growth of the polymer, possible overlaps with the NP and already existing polymer is monitored and if there is an overlap, a new random position is chosen. The initial density needs to be low (0.7 kg/m^3) to be able to generate the chains without overlap. An MD simulation of up to 20 ns under the NPT ensemble follows to fully equilibrate the system at atmospheric pressure and 590 K temperature with a time step Δt = 5 fs. After equilibration, the system is cooled with a constant rate of 10 K/ns, to different lower temperatures, including temperatures below the glass transition temperature of the CG model (170 K). The glass transition temperature, which is an important characteristic of polymer material, was determined from the change in slope of the curve of the specific volume vs. temperature. It is worth mentioning that the transferability of this force field and mapping scheme is limited to a temperature range of about 100 K, and that in general, CG potentials are not transferable over phase boundaries. We use it in spite of theses caveat, knowing that quantitative accuracy at low temperatures cannot be expected. We are confident, though, that qualitative description of the molecular structure of the interphase under deformation can still be obtained.

The uniaxial elongation is carried out by deforming the length of the simulation box, L, in one direction at a constant rate:

$$L(t) = L_0 + \alpha t$$

where L_0 is the initial length of the box in this direction, t is the time and α is the deformation rate. The strain γ_L is defined as $\gamma_L = \frac{L-L_0}{L_0} \times 100\%$. The two perpendicular box dimensions are coupled to the bath pressure (1 bar) using a Berendsen barostat with pressure coupling time 1.0 ps and isothermal compressibility 1.0×10^{-5} 1/kPa. The temperature of the system is kept constant during the deformation by using a Berendsen thermostat with temperature coupling time 0.3 ps. The tension in the system (stress) is equal to $-P_{\chi\chi}$, where **P** is the stress tensor and χ denotes the Cartesian coordinate in the

deformation direction . The Young modulus which is the slope of the stress-strain curve in the linear regime, and the Poisson ratio which is the ratio of transverse strain (perpendicular to the applied load) to the parallel strain, have both been calculated. Most of the results have been obtained with a constant deformation rate of $\alpha = 10$ nm/ns. We are aware of the fact that this deformation rate is much higher than accessible experimental ones. However we had to employ a time dependence that is in line with the MD line timescale allowing time steps in the fs range and simulation times in the range of ns. As a direct comparison with experimental numbers is not possible we have checked that our results are insensible to deformation rates between 1 and 50 nm/ns. These deformation rates are also comparable with other deformation rates reported in literature[27]. With a typical box length 21 nm, the present setup translates into a strain rate of 47%/ns. However some runs have been performed at different deformation rates. We have performed simulations at chain lengths from 200 to 10000 monomers. The simulation times for the deformation runs were 2 ns, during which a maximum strain of 94% was reached. Uniaxial deformations have been applied along all three Cartesian axes independently to three different equilibrated samples. Final results have been averaged over all three samples and three directions of deformation.

We have also performed some simulations with more than one NP to study the effect of the number of NPs on the mechanical properties. Since the CG potential was developed for one NP embedded in PS, there is at present no term for the interaction between NPs. Therefore we cannot simulate the system with a high concentration of NPs. However, we could simulate systems with a volume fraction up to 5.3%. The initial configurations were generated with high dispersion, i.e. the NPs well separated, see comments in the introduction. During the simulation of multi-NP systems we have traced all distances between NPs to ensure that the NPs stay dispersed in the polymer matrix and do not touch each other. The center-to-center distances of NPs have never been less than 5.5 nm. Since the radius of an NP is 2 nm and the diameter of a polymer bead is around 0.5 nm, we can state that at least two layer of polymer have been between two NPs at all times. Since the aim of this work is not to study dispersion of NP in a polymer matrix, we only checked the nearest NP neighbor. The maximum distance of nearest NP neighbor in a box with volume V and N NPs is $\sqrt[3]{\frac{V}{N}}$. At the highest NP concentration in this work (16 NPs), the maximum distance is 8.4 nm and the average nearest-neighbor distance calculated is 6.4 nm. Moreover, the nearest neighbor is more than 5.7 nm apart. Therefore, the NPs are sufficiently dispersed in the polymer matrix that our results pertain to a nanocomposite with homogeneous filler distribution.

2.4 Mechanical properties

Pure polystyrene. We applied deformations to all systems above and below the glass transition temperature T_g = 170 K of the CG model. This temperature is much lower than the atomistic and experimental T_g, both close to 370 K[27,28]. This is a well-known feature of CG polymer models, its reason is that the dynamics in CG is much faster than for atomistic models and experiment. Thus, all properties which depend on the dynamics are affected. Attempted solutions to this problem make use of a stochastic dynamics with artificial friction or defining a scaling factor between CG and atomistic dynamics. We will discuss a strategy to find such a scaling factor for the Young's moduli (see below). As a reference, deformations were first applied to pure PS without nanoparticles, 300 polymer chains with 200 monomers, at a deformation rate of 10 nm/ns and different temperatures. In Fig. 2.1, the stress-strain curves are shown above and below T_g. Below the glass transition, the elastic regime is clearly seen for extensions up to 3%; it is followed by the yield point at 7-10%. To further check the elasticity of the linear regime, a 3% deformation was applied to the system and the strain was then allowed to relax. We observed that the systems below T_g are able to recover the strain and only 0.05% remains after 0.5 ns of relaxation. For systems above the glass transition, no yield points were observed and already below 3% strain, the curves exhibit fluctuations. However, we consider this region as a linear regime in order to obtain an apparent modulus. The (apparent) Young's moduli obtained from the slopes of the stress-strain curves are discussed below.

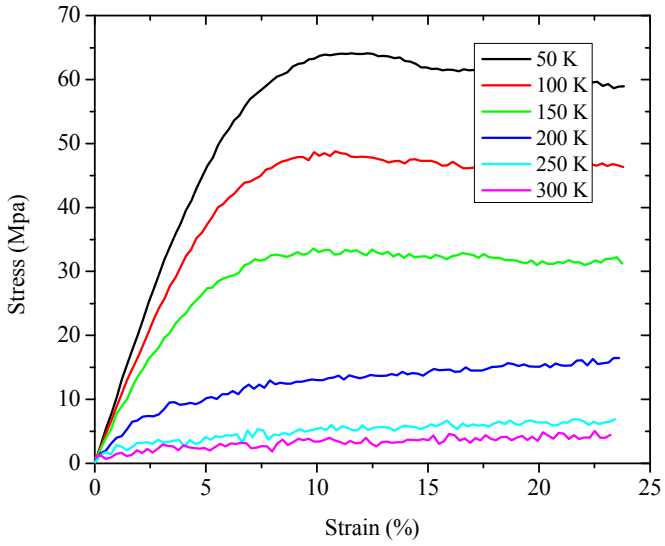

Figure 2.1. Stress-strain response of coarse-grained pure polystyrene (without nanoparticles) at different temperatures obtained at a deformation rate of 10 nm/ns. The glass transition temperature of the coarse-grained model is 170 K.

Some simulations have been performed to investigate the influence of the deformation rate, in the range of 50 to 1 nm/ns, with the barostat parameters kept constant. For all deformation rates, the barostat was able to control the pressure of the systems in the two orthogonal directions. For different deformation rates, no significant differences have been observed in the linear regime. Changing the deformation rate only shifts the yield point. If the box is deformed more slowly, the yield point appears sooner and the yield stress is smaller. For instance for deformation rates of 5, 10 and 15 nm/ns at 100 K, pure PS with a chain length of 200 monomers has yield stresses equal to 44, 47 and 50 MPa, respectively, whereas the Young's moduli obtained from the slopes below 3% strain are 799±29, 827±32 and 832±35 MPa. Also the effect of chain length on the stress–strain curves has been investigated. The total number of monomers remained at 60000 and only the polymer length was changed between 200 and 10000 monomers (MW = 20 kDa to 1 MDa). We observed that all systems have the same slope in the linear regime, Young's moduli obtained from the slopes below 3% strain are 827±32, 856±35 and 853±36 MPa for 200, 1000 and 10000 monomers, which is due to all polymer lengths being greater than the entanglement. After these tests, we have decided to perform all further simulations in this work at a 10 nm/ns deformation rate with 300 polymer chains of length 200.

The Poisson ratio has also been calculated at different temperatures (Fig. 2.2). The Poisson ratio above the glass transition temperature is in the range of 0.4 ~ 0.45, with fluctuations, especially for small deformations. The Poisson ratio obtained from atomistic simulations at 480 K (above the atomistic T_g) is around 0.42[26]. Below the glass transition, the Poisson ration is between 0.30 and 0.33 at small deformations and then increases. This is close to the Poisson ratio obtained from atomistic simulations at 240 K (below the atomistic T_g) of 0.33±0.02[26], and to the experimental estimates of 0.32-0.33[29]. We have observed that the Poisson ratio increases very slowly in the linear regime (< 3% strain), before the slope of the curves increase around the yield point. The Poisson ratio then converges at a rather high deformation.

The Young's modulus has been obtained from the slope of the stres –strain curves in the linear regime (up to 3% strain), table 2.1. The Young's modulus at 240 K is 141 MPa which is twenty times smaller than atomistic (2781 MPa at 240 K)[26]. The reason might be adoption of a softer potential in the CG than in the atomistic model. Even below the glass transition the Young's modulus in the CG model is small. However, we have observed that the behavior of Young's modulus is qualitatively very similar in the atomistic and the CG description; in both cases, it decreases linearly with temperature for temperatures below the glass transition. Lyulin et al.[27] have calculated theYoung's modulus at different temperatures atomistically. We have compared their results to our CG data. Lyulin et al. have reported T_g=370 K, and by interpolation of their data we found that the Young's modulus at this

temperature, E_g, is around 1280 MPa. In our case the glass transition is at 170 K and the Young's modulus is 470 MPa. The Young's modulus of CG and atomistic simulations are compared in Fig. 2.3, where we have plotted the Young's modulus as a function of the temperature, both normalized by the respective values at the glass transition. The data in Fig. 2.3 show that the slopes of experimental and atomistic data at temperatures below T_g are similar, but larger than the CG value. Above T_g, there is a plateau in the atomistic and experimental data. In the CG approach we observe this plateau only above of 1.2 T_g. However, one can estimate the Young's modulus over a wider range of temperatures, e.g., 280 ~ 420 K, from the CG data. For instance, to calculate the Young's modulus at room temperature, 300 K, the normalized atomistic temperature must be calculated as $\frac{T}{T_g} = \frac{300}{370} \sim 0.8$. The normalized Young's modulus at this normalized temperature, 1.45, can then be obtained from the CG data in Fig. 2.3. Multiplying this with the atomistic Young's modulus at the glass transition, 1280 MPa, we arrive at 1856 MPa which is of the same order as the true atomistic value, 2140 MPa. The same can be done using the experimental data. With such values, T_g = 370 K and E_g = 2000 MPa[28], the room-temperature Young's modulus is estimated to be 2900 MPa, compared with the true experimental value of 3500 MPa.

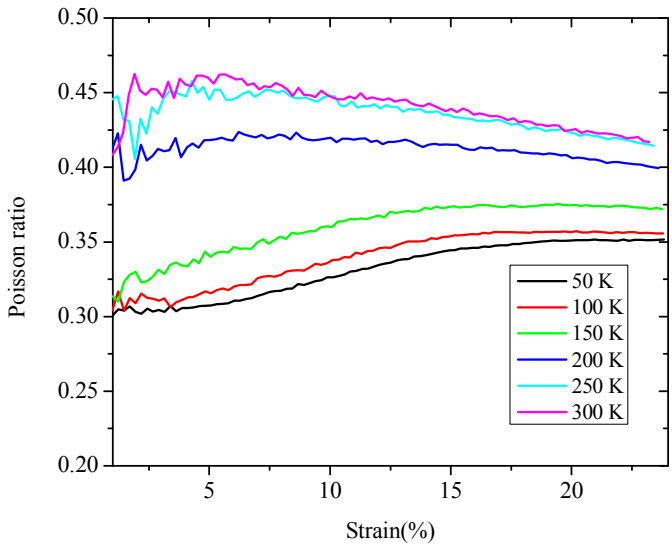

Figure 2.2. Poisson ratio as a function of strain at different temperatures for coarse-grained pure polystyrene (without nanoparticles) at 0.01 nm/ps deformation rate. The glass transition temperature of the coarse-grained model is 170 K.

Temperature K	Young's modulus
100	827
130	710
150	664
170	470
200	216
220	152
240	141

Table 2.1. Young's modulus of coarse-grained pure polystyrene (without nanoparticles) at different temperatures obtained at a deformation rate of 10 nm/ns. The glass transition temperature of the coarse-grained model is 170 K.

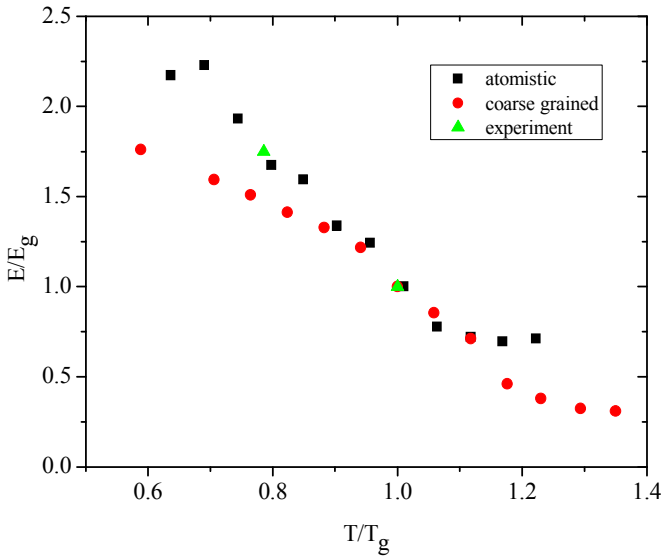

Figure 2.3. Normalized Young's modulus as a function of the normalized temperature for atomistic simulations (Ref. 26), coarse-grained simulations (this work) and experiment (Ref. 27) for pure polystyrene. E_g is the Young's modulus at the glass transition and T_g is the glass transition temperature. The corresponding values used in scaling are: atomistic T_g=370 K, E_g=1280 MPa; coarse-grained T_g =170 K, E_g=470 MPa; experiment T_g=370 K, E_g=2000 MPa.

One nanoparticle. As a first approximation to a nanocomposite, we deformed a system containing a single ungrafted silica NP of 2 nm radius. As for the pure PS, there are 300 chains; the degree of polymerisation is 200 which leads to an undisturbed radius of gyration of ~3.4 nm, which is of the same order as the particle diameter. The previous simulation has shown that the chain length has no effect to the linear deformation regime. Since we found the same glass transition for this system

(T_g=170 K), the simulations have been performed at a scaling temperature of 0.8. A constant deformation rate α=10 nm/ns has been applied. Since the volume fraction of NP is very small 0.3% there is no significant differences in stress-strain curves and the Young's modulus at 0.8T_g (~136 K) is 702 and 706 MPa for pure PS and filled case, respectively.

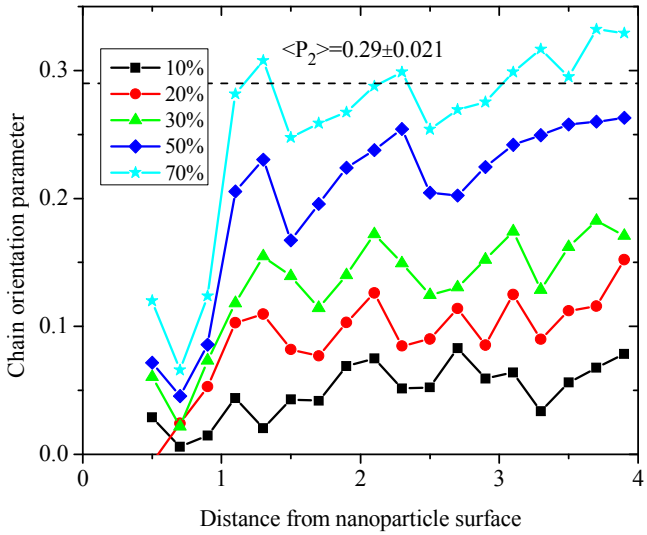

Figure 2.4. Chain segment (5 monomers) orientation in the deformation direction for a system of 300 polystyrene chains of length 200 and a single nanoparticle. The order parameter P_2 (for definition, see text) is shown as a function of the distance from the nanoparticle surface for different strains. P_2 for the undeformed system is zero. The temperature is 136 K corresponding to 0.8 T_g, the deformation rate is 10 nm/ns. The dashed line is the average P_2 for pure polystyrene at 70% strain.

For the case of nanocomposites, it is also interesting to study the polymer structure near the nanoparticle and its evolution under a deformation of the system. The chain orientation is a useful microstructural element to investigate the polymer response. To monitor the structure on the local scale, the orientation of an inter-monomer vector spanning 5 monomers is a sensible probe, since such a segment is still small enough to be localizable. The orientation of the segment is characterized by the second-order Legendre polynomials P_2, given by

$$P_{2\chi} = \frac{3}{2}\left(cos^2\left(\frac{\boldsymbol{e}_i.\mathbf{e}_\chi}{|e_i||e_\chi|}\right)\right) - \frac{1}{2}$$

where $\mathbf{e}_\chi$ is the vector in the direction of the applied strain and $\mathbf{e}_i$ denotes the vector joining beads *i* and *i*+4. P_2 is 0 if the segment vectors are randomly orientated, 1 if the segment vectors are perfectly parallel to the applied strain, and -0.5 if the segment vectors are orthogonal to the applied strain. For the undeformed system P_2 = 0, since the direction of segments are completely random with respect to

the Cartesian coordinates. Then, upon applying strain, the segments will rotate toward the direction of the applied stress and P_2 will increase. We defined the midpoint of the vector $\mathbf{e}_i$ as the position of the segment and averaged P_2 over all segments into spherical bins of thickness 0.2 nm around the NP. The orientation parameter, P_2, has been calculated as a function of distance from the NP surface for strains between 10% to 70% (Fig. 2.4). As expected, P_2 increases with the strain, as the chain segments tend to align with the loading direction. The main point here is that change of the segment orientation is not constant in the simulation box. The change of P_2 within a 1 nm layer near the NP surface is less than beyond this distance. The segments near the NP surface seem to stick to the surface. Therefore, their orientation is surface-dominated and they not align with the loading direction. Beyond 1 nm, the alignment quickly reaches plateau values for every strain value. This plateau value corresponds to the bulk alignment in pure PS. For example, the average P_2 for pure PS at 70% strain is 0.29±0.021 and the average of P_2 between 1 nm and 4 nm away from NP surface for the system containing one NP is 0.3±0.015. Comparing these values shows that beyond the distance of 1 nm from the NP surface, the polymers behave bulk-like. Therefore we can conclude that the thickness of the interphase is 1 nm, if measured by "chain orientability". This compares well with interphase thicknesses measured by other local properties, such as: density oscillations and segment orientation with respect to the surface [22,23], monomer reorientation times[11]. We also obtained the density as a function of the distance from the NP and we have not observed any significant differences between undeformed and highly strained systems (not shown). High deformation causes the overall density to reduce by 4%. This density reduction is, however, distributed throughout the system and no cracks or crazes are apparent in our simulation.

To further study the influence of NP on the polymer orientation under the deformation, we have used the geometric technique developed by Yashiro et al. [30]. In this technique the angle between two vectors that connect bead i to bead i+x and i-x, all on the same polymer, is calculated. The angle between these two vectors is obtained for each applicable bead. The change of this angle during the deformation relates to the stiffness of polymer. Here, since we would like to study the stiffness as a function of distance from the NP, or in other words we would like to analyze the stiffness locally, x should not be too large. On the other hand, if it is too small, the change of the angle due to deformation will be very small. We found that the optimum value of x for our simulation is 5. By sorting beads into spherical bins of thickness 0.5 nm around the NP, the angle between the two vectors has been calculated as a function of the distance of the central bead from NP and then averaged over all angles in different slabs. Fig. 2.5 shows the average angle as a function of distance from the NP surface for the undeformed and 70% deformed systems. for distances beyond 1 nm in the undeformed system, the average angle is more or less constant around 72.0°±0.7 which is very close to pure PS (71.3°±1.2). For

low strains, the average angle remains more or less constant with only a slight increase. As the strain increases, the average angle also increases. This angle increase of angles shows the polymers aligning in the loading direction. However the amount of the increase is not constant in the simulation box. While the average angle beyond a 1 nm seperation from the NP surface increases by around 3.2°, it remains constant near the NP surface. These results show that the NP increases the stiffness of the polymer within a distance of 1 nm from the surface. Therefore, in this area, where the polymer conformation is dominated by surface interactions, the polymer structure does not change due to the deformation.

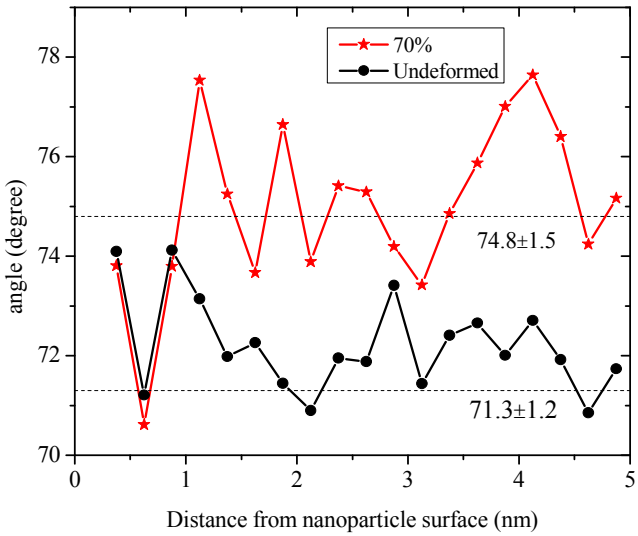

Figure 2.5. The average angle between two vectors that connect bead i to bead i+5 and i-5 as a function of distance from the nanoparticle surface for the undeformed as well as for a 70% strained system. The temperature is 136 K corresponding to 0.8 T_g, the deformation rate is 10 nm/ns. One nanoparticle and 300 chains of length 200 are simulated. The dashed lines are the average angle for the undeformed and a 70% deformed pure polystyrene.

The structure of the polymer at a larger length scale was studied by calculating the radius of gyration of 20-monomer segments (Fig. 2.6). In the undeformed system the radius of gyration near the NP is higher than in the bulk, and far from the NP it converges to the bulk value, R_g=0.95 nm. It shows that the polymers in contact with the NP are elongated along the NP surface. This is known to be due to wrapping of chains around the surface[23]. The region with enlarged R_g is followed by a region of compressed radii of gyration due to the excluded volume of the NP[23], which ends at ~1.5 nm. Beyond this distance, which is of the same order as the segment's unperturbed R_g, we observe essentially bulk behavior. One should expect that the radius of gyration will increase upon applying strain, since the polymers align in the loading direction. This is clearly shown in Fig. 2.6: the more the system is

deformed, the more the polymers are elongated. However, this elongation is not homogeneous. The radius of gyration remains invariant between the NP surface and the crossover distance at 1-1.5 nm surface separation, while at larger distances it increases due to the deformation. All these analyses show that the polymers near the NP surface keep their equilibrium structure also under deformation, whereas at larger distances they then deform slightly. In other words, the interfacial interactions between the NP surface and the polymer matrix chains modify the structure of the polymer in the vicinity of the NP. Analyzing the orientation and structure of the segments, we obtained the length over which the polymer properties of are affected, i.e. the thickness of the interphase, which is about 1 nm. It is worth mentioning that the size of the interphase depends on the properties calculated and in our case these are the mechanical properties.

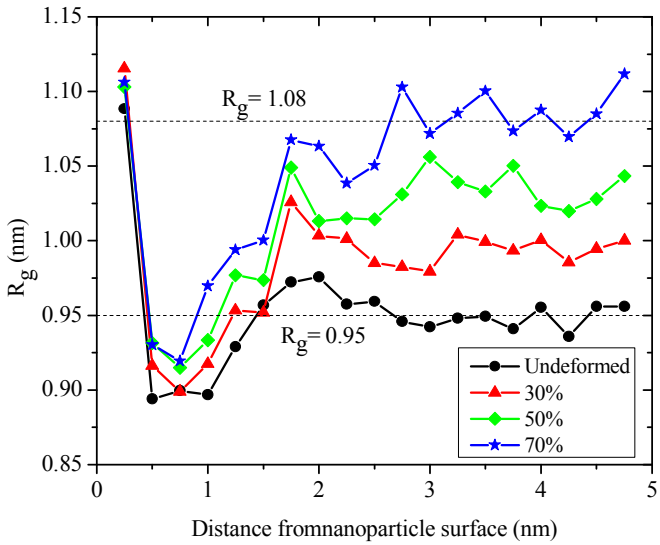

Figure 2.6. Radius of gyration of 20-monomer segments as a function of the distance of their centre of mass from the nanoparticle surface for undeformed as well as deformed systems. The temperature is 136 K corresponding to 0.8 T_g, the deformation rate is 10 nm/ns One nanoparticle and 300 chains of length 200 are simulated. The dashed lines are the radii of gyration for the undeformed and a 70% deformed pure polystyrene.

More than one nanoparticle. An interesting topic in nanocomposite materials is the enhancement of mechanical properties as a function of the filler volume fraction. Since the interfacial interaction between polymers and the NP surface enhances the mechanical properties of the polymer, the large surface area - in addition with the high modulus of the filler - is expected to influence the bulk properties of the nanocomposite. To study the effect of the NP volume fraction on the mechanical properties, we have performed simulations with different numbers of NPs. We have used the same amount of the polymer (300 chains with 200 monomers) with 4, 8, 12 and 16 NPs. The volume

fraction is defined as NP volume to the polymer volume. After full equilibration and cooling to $0.8T_g$ (~140 K) the volume fraction is 1.4%, 2.7%, 4.0% and 5.3% respectively. The distance between the NPs was always checked to ensure that the NPs are dispersed in the matrix or at least that they are not in direct contact (see section Model and Simulation Algorithm). As emphasized above this setup does not allow an analysis of aggregation. We found that the glass transition temperature slightly increased by adding more NPs to the matrix. For instance, the T_g is 170 K for pure PS and 176 K for system with 16 NPs. This result is consistent with work done by Starr et al. [31]. They have studied the change of the glass transition in nanocomposite materials by simulating a bead spring melt surrounding a nanoscopic particle. They have found that, for a system with an attractive potential between polymer and the NP, the glass transition increases, but for non-attractive systems it decreases. They have claimed that the glass transition temperature increases as the attractive NPs slow down the dynamics of the system. The same can be said about our simulations: As the interaction of the silica NP with PS is attractive, it slows down the dynamics of the system and therefore increases the glass transition. Adding more NPs means the dynamics of more polymer chains is attenuated and the glass transition is higher. To all four systems a deformation with the constant rate α=10 nm/ns has been applied $0.8T_g$ (~140 K). The segment orientation parameter P_2, in the same definition as above, has been calculated to study the size of the interphase at different volume fractions. Comparison of the orientation parameter of the entire system with one NP and several NPs shows that the thickness of the interphase does not change. To further study the orientation of polymers in the region between two NP surfaces under deformation, the orientation parameter has been calculated between these two NPs. To this end, we considered a cylinder with the same radius as the NP and the length of center-to-center distance, and calculated the P_2 for all segments which were located in the cylinder. Fig. 2.7 shows the P_2 as a function of distance from the NP surface when the centre-to-centre distance is 8.1 nm and 11.8 nm as well as for the system with one NP, all for 20% deformation. It is worth mentioning that, since the radius of NP is 2 nm, the nearest distance between NP surfaces is 4.1 nm and 7.8 nm, respectively. As the profiles for 2 NPs are expected to be symmetric, we present the average of the two branches. The orientation of the polymers between two NPs at a distance of 11.8 nm is very similar to the system with one NP and in both systems the size of the interphase is 1 nm. For the NP distance of 8.1 nm, we observe the same behavior within 1 nm of the NP surfaces. But at longer distances the oscillations around the mean are more pronounced than for the two other systems, which experience less confinement. For interparticle distances below 8 nm, the fluctuations of the orientation parameter between the particles is too high and too erratic to clearly distinguish the interphase region. The reason might be that the polymers are packed between the two NPs and they cannot rotate freely.

The slope of the stress-strain curves in the linear regime (3%), which represents the Young's modulus, has been calculated for all systems at different NP volume fractions. Error estimates were obtained as fluctuation of the stress at 3% strain. The squares in Fig. 2.8 show the calculated Young's moduli. The Young's modulus increases linearly with an increasing volume fraction of the nanoparticles. This result is not consistent with the experimental result[24], which shows that there is an optimum fraction (The 4% weight fraction was reported in the experimental work but the weight fraction of our system at high concentration is 12%) and that the addition of more NPs beyond that value causes a decrease of the Young's modulus. The reason might be that in experiment the NPs agglomerate at high concentrations, while in our simulation the NPs are completely dispersed. Based on the Young's modulus of pure PS and NP we found a simple equation to estimate the Young's modulus of the nanocomposite: $E_{NC} = V_{PS}E_{PS} + V_{NP}E_{NP}$, where V_{PS} and V_{NP} are the volume fraction of the PS and NP, respectively, and E_{PS}, E_{NP} and E_{NC} the Young's moduli of PS, NP and the nanocomposite, respectively. By applying a deformation to a silica crystal at 135 K, the Young's modulus of the NP obtained was E_{NP}=3790 MPa. The line in Fig. 3.8 represents the estimate of the nanocomposite's Young's modulus with this linear equation. The agreement between the simple additivity equation and the actual moduli is quite close. However, the estimated values are systematically below the computed values. This could indicate a maximum of the modulus (as in experiment[24]) at a higher NP volume fraction, which has not been sampled here. We should note that the simulations confirm the increase of the modulus with the NP volume fraction at low NP concentrations. They do not allow to separate the effects of simply filling some volume with a material of higher modulus and the effect of changing the polymer structure and dynamics in the interphase around every particle. Since in our simulation, the NP size is constant, addind particles increases the filler volumeand the filler surface by the same ratio. To further study this aspect, simulations with different NP sizes will have to be performed.

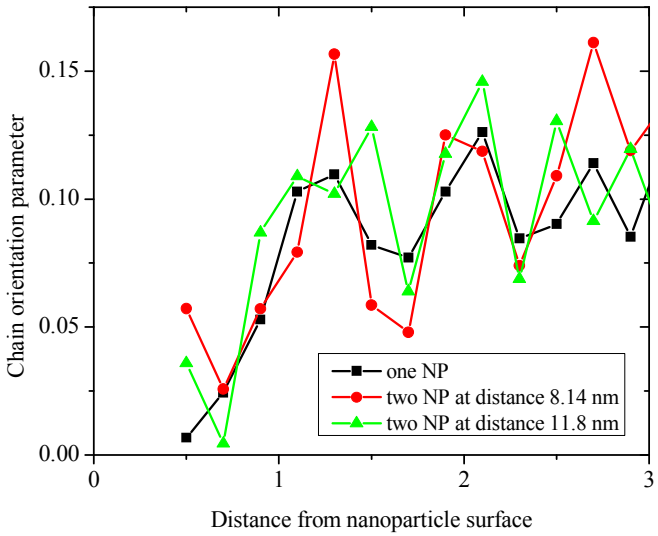

Figure 2.7. Profile of the chain segment (5 monomers) orientation parameter P_2 in the region between two nanoparticles at centre-to-centre distances of 8.1 nm and 11.8 nm as a function of distance from the nanoparticle surface for systems at 20% strain. The orientation parameter for a system with a single NP is also plotted for comparison. The temperature is 136 K corresponding to 0.8 T_g, the deformation rate is 10 nm/ns One or 2 nanoparticles and 300 chains of length 200 are simulated.

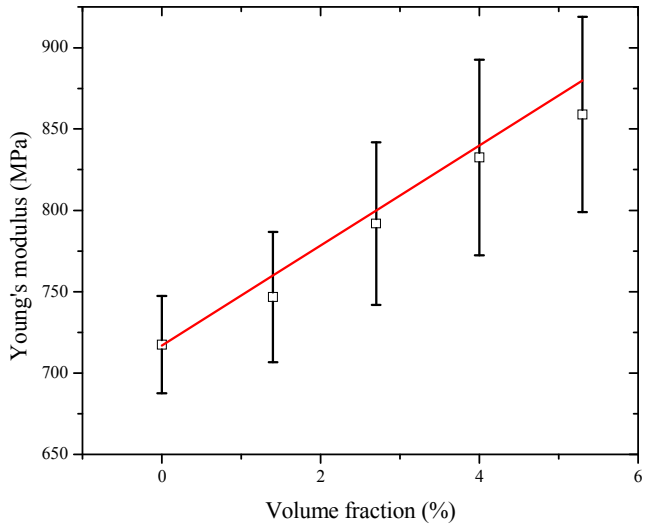

Figure 2.8. Young's modulus of the nanocomposite at different nanoparticle volume fractions. Squares represent the calculated values, error bars are estimates from stress fluctuations at 3% strain. The line shows the Young's modulus of the nanocomposite estimated by the linear equation $E_{NC} = V_{PS}E_{PS} + V_{NP}E_{NP}$ where V_{PS} and V_{NP} are the volume fraction of the PS and NP respectively. E_{PS}, E_{NP} and E_{NC} are the Young's moduli of PS, NP and the nanocomposite respectively.

2.5 Conclusions

Coarse-grained molecular dynamics simulations for a uniaxial mechanical deformation have been performed for pure polystyrene as well as polysterene containing silica NPs. The simulated stress-strain behavior of pure PS at different temperatures reproduces the significant difference between the mechanical properties of PS below and above the glass transitions. The Poisson ratio obtained from deformations below the glass transition temperatures is around 0.3 while it is around 0.4 above the glass transition. The Young's modulus has been calculated at different temperatures from the initial linear regions (3% strain) of the stress-strain curves. It has been shown that the behavior of the Young's modulus as a function of temperature is similar to that at the atomistic level. Below the glass transition, the Young's modulus decreases linearly and above the glass transition there is plateau. The Young's modulus of the coarse-grained model, however, is found to decrease more smoothly with temperature than that of the atomistic model due to the fact that the CG potential is softer.

To study the effect of the interaction of the NP surface on the polymer chains, orientation parameters have been calculated as a function of distance from the NP surface. The uniaxial deformation of the polymer leads to an orientation of the chains in the direction of the deformation. However, it has been shown that the polymers near the surface tend to keep their equilibrium orientation. Beyond 1 nm from the NP surface they deform bulk-like. This behaviour is confirmed by the change of other investigated parameters under deformation, such as intersegment angles and segment gyration radii. So we put the thickness of the interphase as measured by the deformation dependence of the investigated geometrical parameters. Based on our findings, the interfacial interactions between the NP surface and the polymer chains improve the mechanical properties of the polymer in the vicinity of the NP surface. This is the main reason that nanocomposites are more resistant to deformation than polymer matrices.

Finally, to study the effect of NP volume fractions, simulations have been performed with different numbers of NPs. It was observed that added NPs increase the glass transitions, since the NPs slow down the dynamics of the system. The Young's modulus at different NP volumes, obtained from the stress-strain curves, increases linearly with the addition of the NPs. We found that the nanocomposite modulus can be approximated by volume-weighted additive contributions from the polymer and filler. However, there is a small negative deviation of the actual moduli from the additive estimate which

could point to mutual interactions of the interphases around different nanoparticles, once they approach too small distance.

References

(1) Kumar, S. K.; Krishnamoorti, R. *Annu. Rev. Chem. Biomol. Eng.* **2010**, *1*, 37-58.

(2) Kraus, G. *Angew. Makromol. Chem.* **1977**, *60*, 215-248.

(3) Rittigstein, P.; Torkelson, J. M. *J. Polym. Sci. Pol. Phys.* **2006**, *44*, 2935-2943.

(4) Putz, K.; Krishnamoorti, R.; Green, P. F. *Polymer* **2007**, *48*, 3540-3545.

(5) Cui, S. *Carbon* **2003**, *41*, 797-809.

(6) Ding, W.; Eitan, A.; Fisher, F. T.; Chen, X.; Dikin, D. A.; Andrews, R.; Brinson, L. C.; Schadler, L. S.; Ruoff, R. S. *Nano. Lett.* **2003**, *3*, 1593-1597.

(7) Valentín, J. L.; Mora-Barrantes, I.; Carretero-González, J.; López-Manchado, M. A.; Sotta, P.; Long, D. R.; Saalwächter, K. *Macromolecules* **2010**, *43*, 334-346.

(8) Ciprari, D.; Jacob, K.; Tannenbaum, R. *Macromolecules* **2006**, *39*, 6565-6573.

(9) Smith, J. S.; Bedrov, D.; Smith, G. D. *Compos. Sci. Technol.* **2003**, *63*, 1599-1605.

(10) Brown, D.; Mélé, P.; Marceau, S.; Albérola, N. D. *Macromolecules* **2003**, *36*, 1395-1406.

(11) Ndoro, T. V. M.; Böhm, M. C.; Müller-Plathe, F. *Macromolecules* **2012**, *45*, 171–179.

(12) Brown, D.; Marcadon, V.; Mélé, P.; Albérola, N. D. *Macromolecules* **2008**, *41*, 1499-1511.

(13) Gersappe, D. *Phys. Rev. Lett.* **2002**, *89*, 058301.

(14) Frankland, S. *Compos. Sci. Technol.* **2003**, *63*, 1655-1661.

(15) Griebel, M. *Comput. Methods. Applied. M.* **2004**, *193*, 1773-1788.

(16) Liu, J.; Wu, S.; Zhang, L.; Wang, W.; Cao, D. *Phys. Chem. Chem. Phys.* **2011**, *13*, 518-29.

(17) Liu, J.; Wu, Y.; Shen, J.; Gao, Y.; Zhang, L.; Cao, D. *Phys. Chem. Chem. Phys.* **2011**, *13*, 13058-13069.

(18) Papakonstantopoulos, G.; Doxastakis, M.; Nealey, P.; Barrat, J.-L.; de Pablo, J. *Phys. Rev. E* **2007**, *75*, 031803.

(19) Liu, J.; Zhang, L.; Cao, D.; Wang, W. *Phys. Chem. Chem. Phys.* **2009**, *11*, 11365-84.

(20) Zeng, Q. H.; Yu, A. B.; Lu, G. Q. *Prog. Polym. Sci.* **2008**, *33*, 191-269.

(21) Allegra, G.; Raos, G.; Vacatello, M. *Prog. Polym. Sci.* **2008**, *33*, 683-731.

(22) Ndoro, T. V. M.; Voyiatzis, E.; Rahimi, A.; Theodorou, D. N.; Böhm, M. C.; Müller-Plathe, F. *Macromolecules* **2011**, *44*, 2316-2327.

(23) Rahimi, A.; Ndoro, T. V. M.; Leroy, F. D.; Rahimi, M.; Böhm, M. C.; Müller-Plathe, F. *Macromolecules* **2012**, *45*, 572-584.

(24) Kontou, E.; Anthoulis, G. *J. Appl. Polym. Sci.* **2007**, *105*, 1723-1731.

(25) Harton, S. E.; Kumar, S. K.; Yang, H.; Koga, T.; Hicks, K.; Lee, H.; Mijovic, J.; Liu, M.; Vallery, R. S.; Gidley, D. W. *Macromolecules* **2010**, *43*, 3415-3421.

(26) Qian, H.-J.; Carbone, P.; Chen, X.; Karimi-Varzaneh, H. A.; Liew, C. C.; Müller-Plathe, F. *Macromolecules* **2008**, *41*, 9919-9929.

(27) Lyulin, A. V.; Balabaev, N. K.; Mazo, M. A.; Michels, M. A. J. *Macromolecules* **2004**, *37*, 8785-8793.

(28) Kaliappan, S.; Cappella, B. *Polymer* **2005**, *46*, 11416-11423.

(29) Mark, J. E. *Polymer data handbook*; Oxford University Press, 1999.

(30) Yashiro, K. *Int. J. Mech. Sci.* **2003**, *45*, 1863-1876.

(31) Starr, F. W.; Schrøder, T. B.; Glotzer, S. C. *Macromolecules* **2002**, *35*, 4481-4492.

3. Nonperiodic stochastic boundary conditions for molecular dynamics simulations of materials embedded into a continuum mechanics domain*

3.1. Abstract

A scheme is described for performing molecular dynamics simulations on polymers under nonperiodic, stochastic boundary conditions. It has been designed to allow later the embedding of a particle domain treated by molecular dynamics into a continuum environment treated by finite elements. It combines, in the boundary region, harmonically restrained particles to confine the system with dissipative particle dynamics to dissipate energy and to thermostat the simulation. The equilibrium position of the tethered particles, the so-called anchor points, are well suited for transmitting deformations, forces and force derivatives between the particle and continuum domains. In the present work the particle scheme is tested by comparing results for coarse-grained polystyrene melts under nonperiodic and regular periodic boundary conditions. Excellent agreement is found for thermodynamic, structural, and dynamic properties.

3.2. Introduction

The standard way of avoiding surface artefacts in molecular dynamics (MD) simulations of bulk systems is through periodic boundary conditions (PBC): Particles leaving the periodic simulation box through one face re-enter it through the opposite face. Moreover, a particle only interacts with the closest of all periodic images of any other particle.[1] For certain problems, however, there are good reasons to employ *nonperiodic* boundary conditions[2-8]. Firstly, PBC can be unnecessarily costly. They require a simulation box whose shape is space-filling when periodically replicated, for example a cube. If the simulated system consists of a globular macromolecule such as a protein in solution or a localized chemical event, less solvent has to be simulated in a spherical than a cubic box. Thus, nonperiodic boundary conditions were originally designed for these cases[9-11]. Secondly, PBC may introduce spurious features in structural or dynamic properties in certain systems[12-17] (even more so when electrostatic interactions are also treated as periodic, which is not an issue in this work[18,19]). This

*Rahimi, M., Karimi-Varzaneh, H. A., Böhm, M. C., Müller-Plathe, F., Pfaller, S., Possart, G., & Steinmann, P. (2011). *The Journal of chemical physics*, *134*(15), 154108.

behavior follows from a periodicity that is artificially imposed onto intrinsically nonperiodic systems like fluids and amorphous polymers.

Our reason for developing nonperiodic boundary conditions is different. We plan to embed a molecular dynamics domain into a larger region described by a continuum simulation technique (finite element method, FE)[20]. The continuation of the material beyond the MD region is provided by the FE domain; therefore, there is no need and no use for a periodic continuation. For problems of fluid flow, nonperiodic MD regions have been embedded into a continuum domain described by computational fluid dynamics schems, in order to locally resolve flow problems at a higher resolution; for recent reviews, see Refs. 21 and 22 . Two schemes are widely used. In the so-called state-variable approach, the MD and the continuum domain overlap with each other. In this coupling region, the continuum and particle descriptions are simultaneously valid and consistent[23]. Continuity of thermodynamic and transport properties (mass and momentum flux) across the interface between the particle and the continuum region is the most important issue. In other state-variable schemes, these two regions are separated from each other by a hard wall. To control the density fluctuations near the boundaries, an external boundary force is applied to the particles[24,25]. In contrast to the state-variable approach which is based on an exchange of variables, the second technique is characterized by flux exchange[26]. In this method the flux boundary conditions are used to couple the MD to the continuum domain[27]. They guarantee that the MD domain exchanges mass, momentum, and energy with the continuum domain according to the underlying microscopic dynamics.

In the area of structural mechanics, the concept of embedding MD domains into a larger environment modeled by a continuum method has also been used, for example to model crack propagation and materials failure[28-32]. However, these applications have to our knowledge been limited to crystalline materials, e.g. metals. The known atom positions in these systems can be used to simplify the coupling, for example by introducing affine and synchronous deformations of atoms and finite elements. This is the case in the so-called quasicontinuum method where, roughly spoken, the resolution of a FE domain is locally increased to that of the underlying atomic lattice. Other approaches, like e.g. the bridging domain method[33] or the Arlequin method[34], define an overlap region which does not require a particle lattice any more. Our objective for embedding an MD domain into a FE surrounding is different from the above applications. Therefore the requirements on the nonperiodic boundary conditions are different. We aim to ultimately study the behavior of polymeric materials under variable deformations. Detailed simulation studies will be necessary to estimate the maximum deformations in viscoelastic materials that can be described by a linear stress deformation relation. The materials we have in mind include - in principle - amorphous polymers, polymer blends,

block-copolymers, semicrystalline polymers as well as nanocomposites. They all have an interesting elastic and plastic deformation behavior and failure mechanisms, which are not yet fully understood on a molecular scale. It is their common property that they are highly disordered and sometimes even heterogeneous and anisotropic. Affine deformation strategies of the established quasicontinuum method for crystalline materials thus cannot be employed.

In particular, we need to devise different nonperiodic boundary conditions for the MD domain for polymeric and other amorphous systems, which is the subject of this contribution. (A preliminary version of the coupling strategy has already been given[35], the implementation and testing of the MD-FE hybrid scheme for amorphous materials will be fully described in a later article.) Our nonperiodic boundary conditions require a set of modifications to standard MD, which ensure the following features:

(i) The boundary confines the molecules to the designated MD region, preventing them from evaporating into the FE domain.

(ii) The boundary exerts pressure on the system to create a thermodynamic state (pressure, density) in its centre, which is the same as for the system under the usual PBC. It compensates the spurious surface tension.

(iii) The boundary acts gently on the MD domain in order to produce polymer structure and dynamics as close as possible to an unperturbed periodic simulation.

(iv) The boundary provides a heat bath for the MD region and controls its temperature.

(v) The boundary mimics the dynamical influence of the missing material beyond the simulation box. In particular, it can be made to provide a substitute of the random collisions of MD particles with the missing external atoms and to inhibit dynamics artifacts due to the presence of the boundary.

(vi) In view of the intended coupling to an FE environment, the boundary conditions are able to transmit displacements and forces between the two domains. In later applications the boundary conditions will be extended to allow deformations of the MD region.

Requirements (i)-(iii) and (vi) are met by defining so-called anchor points in the boundary region, which - at the same time - confine the system and provide a handle for coupling forces between the two domains. Requirements (iv) and (v) are met by including an area of stochastic dynamics at the edge of the MD domain which may or may not coincide with the boundary region[9-11]. In the following, we will refer to this collection of implemented features simply as stochastic boundary conditions (SBC). A sketch of the coupled SBC MD-FE system is provided in Fig. 3.1. The particle domain of

this hybrid method is tested by comparing the results of thermodynamic, structural and dynamic properties of a coarse-grained (CG)[36] model of polystyrene under normal periodic and the new stochastic boundary conditions.

3.3. Methods

In our stochastic boundary condition scheme, the particle domain is divided into three regions: the MD region, the stochastic or dissipative particle dynamics (DPD) region, and the boundary region (Fig. 3.1). We have employed the same coarse-grained resolution in the three domains. This mapping avoids a number of problems of multiscale simulations in which particle domains of different resolution are coupled. Strategies to perform these simulations have been described in the Ref 37. Let us continue with the present MD-FE scheme. Particles in the MD region move according to standard

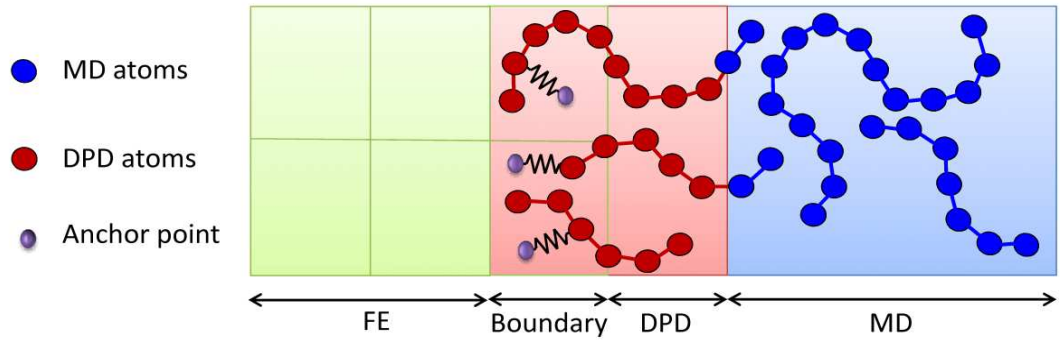

Figure 3.1 : The figure illustrates the stochastic boundary conditions and the coupling to finite element. All atoms in the disipative particle dynamic (DPD) and boundary region move according to the equations of the DPD thermostat. When a particle crosses the border from the DPD to the MD region the DPD thermostat is no longer acting on it and vice versa. In the boundary region, some particles are connected to anchor points via harmonic springs.

Newtonian mechanics. This is the core region, where properties of the system are analysed and where the interesting events are going to take place. Therefore, in this region the description of the material has to be as realistic as possible. The stochastic dynamics formalism used for the region surrounding the MD region is of the dissipative particle dynamics (DPD)[38] type, which has the advantage over other stochastic dynamics schemes such as Brownian dynamics to be locally momentum conserving, so that shear flows can be simulated if necessary. The DPD equations of motion are used for all particles located in this region. However, the conservative forces in this region are the same as in the

MD region, and not the usual linear forces often used in DPD schemes. The DPD region includes the boundary region (i.e. particles in the boundary region also follow the DPD equations of motion); however, the DPD region can be larger than the boundary region. If, on the other hand, the core part of the system (called above the MD region) could be also described by dissipative particle dynamics, there would be no reason not to use DPD in the whole particle simulation box. The third region, the boundary region, provides for the containment of the MD and DPD regions and it will later be used to communicate forces and displacements between the particle and the continuum domain. These purposes are served by space-fixed anchor points, which are distributed exclusively in the boundary region. In the following, we will discuss the model and implementation issues of the different regions.

The boundary area is the outermost region. It contains particles which are mobile and follow the DPD equations of motion. This is in contrast to some other SBC schemes where the boundary region is formed by rigidly fixed particles[5] or by a static external potential of the hollow-sphere type[4,6]. In order to be able to exert an external force on the particle domain, we introduce so-called anchor points. To each anchor point, one of the mobile particles is connected by a harmonic potential $V(\mathbf{r},\mathbf{r}_0)=\frac{k}{2}(\mathbf{r}-\mathbf{r}_0)^2$. The force constant k can be considered as a penalty factor in the suggested coupling scheme which does not represent a material property. The actual position of the particle is defined by the vector $\mathbf{r}$. The anchor point is presently space-fixed at the position $\mathbf{r}_0$. (Later, when the coupling to the FE surroundings is introduced, the anchor point will be fixed to a relative position in the finite element, which overlaps the particle domain in the boundary region.) As the anchor point is not mobile, no equations of motion are solved for it. The force exerted on the anchor point by the molecular system is then given by $\mathbf{F}(\mathbf{r},\mathbf{r}_0)=-\frac{\partial V(\mathbf{r})}{\partial \mathbf{r}_0}=k(\mathbf{r}-\mathbf{r}_0)$ and the tensor of the force derivatives as $\frac{\partial \mathbf{F}}{\partial \mathbf{r}_0}=\begin{pmatrix}-k & 0 & 0\\ 0 & -k & 0\\ 0 & 0 & -k\end{pmatrix}=const.$ The forces and force derivatives will be needed in the MD-FE coupling scheme. The force gradients are a key parameter in the Newton-type energy minimization of the coupled scheme[34,35]. The advantage of using anchor points instead of space-fixing all or a subset of the atoms is that the force on the anchor point comes only from a simple harmonic potential. There are no many-body or curvilinear terms (bond angle and dihedral forces)[1] and no complex analytical[39] or tabulated numerical potentials[40,41] involved here. All these complicated interactions are allowed exclusively between particles, but not between particles and anchor points. We notice that a spherical

container made up of harmonically restrained particles has been used previously to implement nonperiodic boundary conditions[3].

The particles tethered to anchor points are allowed a local mobility which is defined by the force constant k of the harmonic potential, but they cannot leave the box. Thus, the particles feel the anchor points as a static external potential, and the sum of the harmonic forces from the anchor points determines the pressure inside the box. In other words, the anchor points assume the role of a wall around the particle domain. Particles exert forces on the wall and in turn the wall exerts a force on the particles.

If the system consists of polymers, it is not necessary to connect all particles in the boundary region to anchor points. For a polymer chain, it is sufficient to connect one or two of its monomers to anchor points to keep the whole molecule at its place (Fig. 3.1). This may be advantageous, as we intend to perturb the system as little as possible by the boundary conditions. Hence, both the number of anchored particles and the force constant k should be chosen as small as possible, the criterion being that their choice must still sufficiently confine the particles in the particle domain. We try to further minimize distortions under the influence of the anchor points by their spatial distribution. We use an exponential distribution for the anchor point density in the boundary region. It decreases from one at the outer surface of the box to zero at the inner end of the boundary region where it borders the DPD region. This exponential anchor point distribution places more confinement near the surface, where particles have a higher chance of escape, and less rigidity on the inner side, where anchor points could potentially disturb the properties in the analysis region.

An additional role of the anchor points will be in the future to couple the particle domain to the continuum domain. This will be described in detail elsewhere; only a short outline is given here. In the boundary region, particle domain and continuum domain overlap (Fig. 3.1). A deformation of the surrounding continuum region, which is modeled by finite elements, will entail a deformation of the elements of the boundary region, too. The anchor points will no longer be space-fixed but will be connected to the finite elements in the boundary region. Thus, a deformation of the finite elements will translate into a displacement of the anchor points. If the prescribed deformation of the FE domain is not too large, this displacement is small, but it creates a change of the external field felt by the particles via the spring constant k. In the intervening molecular dynamics steps (there will be many MD steps per one FE step) the particles move in this field and they exert forces on the anchor points (see above). These forces and their gradients, time-averaged over the MD steps after equilibration, are then used in the next FE step, representing the response of the particle region to a deformation by the

FE domain. Vice versa, the influence of the FE region on the MD part is expressed in the positions of anchor points which are updated in each FE step.

The second component of our boundary conditions is a region near the boundary where dissipative particle dynamics is operating, the DPD region for short. The particles in this region follow the equations of motion of DPD, i.e. in addition to the systematic forces, there are pairwise random forces and pairwise friction forces acting on them[42]. However, we are not using the conservative interparticle forces customarily associated with DPD, which are generic and soft-core. Instead, we use the interparticle forces of our coarse-grained polymer model. This combination of DPD equations of motion with a coarse-grained polymer model has been very successful in reproducing the correct polymer dynamics[43]. The DPD region's main raison d'être is to pretend that there is a large mass of polymer beyond the confines of the particle region. In addition, it serves as a canonical thermostat, since the combination of a random noise amplitude σ and a friction coefficient γ defines a temperature T by way of a fluctuation dissipation theorem: $\sigma^2 = 2\gamma k_B T$. [42] The performance of the thermostat defined by its ability to maintain the temperature in the central MD region at the target value depends on the length of the time step and the friction. We observe deviations of up to 12.5 K below the target temperature when using too large time steps (10 fs) and too large friction constants (1200 pN ps nm^{-1}). This behavior has been traced back to artifacts of the integrator[44]. Therefore, only in a certain range of the DPD friction, the DPD thermostat can control the temperature well[43]. To adopt large time steps in the simulation, a DPD friction as small as possible has to be chosen. We have found that the combination of a timestep of 5 fs and a friction of 12 pN ps nm^{-1} is a useful combination, as it maintains the target temperature of 300 K within a fluctuation of 1.5 K.

Particles inside the central MD region move according to Newton's equations of motion, all particles outside according to the DPD equations of motion (note that particles interact with the same potentials in both regions). Particles switch their dynamics when crossing between the regions: A particle which is near the border, but inside the MD region has only conservative interactions, even with those particles in the DPD region, which are within its cutoff. In contrast, a particle in the DPD region has conservative interactions with all particles in its cutoff, but friction and random interactions only with particles, which are also located in the DPD region. The passage of particles between the DPD and MD region implies that the number of particles in the MD region is not constant, but should fluctuate around an equilibrium value. The exchange of particles between the two domains is important to preserve the equilibrium structure and the structural fluctuations in the MD region.

3.4. Simulation details and results

To derive the coarse-grained potential for test calculations under stochastic boundary conditions we followed a strategy described previously for amorphous polystyrene (PS)[45]. The tabulated potential has been obtained by Iterative Boltzmann inversion[46], which optimises the coarse-grained (CG) potential to reproduce structural distribution functions of a reference atomistic model. It uses one superatom per chemical repeat unit placed at its center of mass[45]. In atactic PS, the repeat units have different absolute conformations (R and S), which are treated in the model as two different bead types. All simulations were carried out by our software package IBIsCO, which is able to handle tabulated potentials[47]. The new stochastic boundary conditions were also implemented into this code. The polymer was simulated both with SBC and, for comparison, with orthorhombic periodic boundary conditions (PBC).

Simulations under PBC were carried out to generate reference results for comparison as well as to generate initial configurations for the subsequent SBC simulations. The PBC simulations contained 4104 atactic PS chains of 20 monomers at 300 K. The Berendsen thermostat (coupling time 500 fs) and barostat (coupling time 5000 fs, isothermal compressibility 1.0×10^{-6} kPa^{-1}) were used[48]. Time steps of 5 fs have been chosen. A nonbonded cutoff of 1.7 nm has been combined with a neighbor list cutoff of 1.8 nm. The PBC system was simulated for 10 ns.

From the final configuration of the PBC simulation the starting configuration for the SBC simulations was generated by shifting all monomers into the original periodic cell. Polymer chains, which were not located completely in the box, were divided into smaller fragments. Therefore, there is a small number of polymers with different chain lengths near the surface of the box. The periodic cell after equilibration under NPT conditions had a length of about 24 nm, which is therefore also the length of the nonperiodic simulation box. Within this box, the central region of 19 nm was designated as MD region, cf. Fig. 3.1. Thus, on all sides the MD region is 2.5 nm away from the edge of the particle domain and, hence, from the vacuum. This distance is larger than the cutoff radius (1.7 nm) and avoids a direct influence of the vacuum boundary on the MD region. The thickness of the boundary region (containing anchor points, DPD equations of motion) was 1.7 nm, equal to the cutoff. The DPD region (no anchor points but DPD equations of motion) is therefore 0.8 nm wide. With these choices, we ended up with initially 41298 MD and 40782 DPD particles.

The next step was to define the anchor point positions. Every anchor point is attached to one particle. Hence, we took the anchor-point position to be the same as that of the particle it was attached to. The selection algorithm ensured that there was at least 1 anchor point per polymer chain in the

boundary region. In addition, an exponential density of anchor points falling from the outer to the inner end of the boundary region was imposed. We calculated the probability for every particle in the boundary region to be connected to an anchor point based on its position. The tethered particles were then selected with this probability using a random number. As it was discussed in the method section we would not like to perturb the MD region by using too much anchor points. Using a small number of

Condition	Number of anchor points	Density (kg/m^3)	Temperature (K)	Squared radius of gyration (nm^2)	Squared end to end distance (nm^2)
PBC	-	1020±0.43	300 ±0.36	1.004 ±0.02	6.17±0.22
SBC	7262	1015±2.5	300.7±0.91	1.006±0.0032	6.192±0.040
SBC	10954	1017±0.8	300.7±1.08	1.008±0.0015	6.181±0.019
SBC	13780	1019±2.5	301.3±1.12	1.006±0.0018	6.189±0.022

TABLE 3.1: Properties of melts of polystyrene chains of 20 monomers at 300 K. Comparison of properties evaluated in the molecular dynamics region calculated under nonperiodic stochastic boundary conditions (SBC) with different numbers of anchor points and under periodic boundary conditions (PBC). For all SBC simulations, the DPD parameters are σ=10 pN $ps^{1/2}$ and γ=12 pN ps nm^{-1} and the anchor point force constant is k=1400 kJ mol^{-1} nm^{-2}.

anchor points may be cause a deviation in density and pressure in the MD region from the target value. To solve this problem we have used a method to optimize the force constant. Furthermore we compressed the box for pressure correction without using too many anchor points.

The control parameters in the SBC simulations were essentially the same as described above for the MD calculations under PBC, save for a few changes and additions due to the boundary implementation. For the DPD equations of motion a random force amplitude σ=10 pN $ps^{1/2}$ and a friction coefficient γ=12 pN ps nm^{-1} were used. This combination was previously shown to control the temperature well in a similar system[43]. The temperature is controlled only in the DPD region, not in the MD region. However, the temperature of the MD region quickly equilibrates to that in the DPD region after an initial transient behavior (Table 3.1). We also found that the number of anchor points has no influence on the temperature and a minor influence on the density of the MD region. Even for the smallest number of anchor points, the density of the reference PBC simulation is reproduced to about 0.5 %.

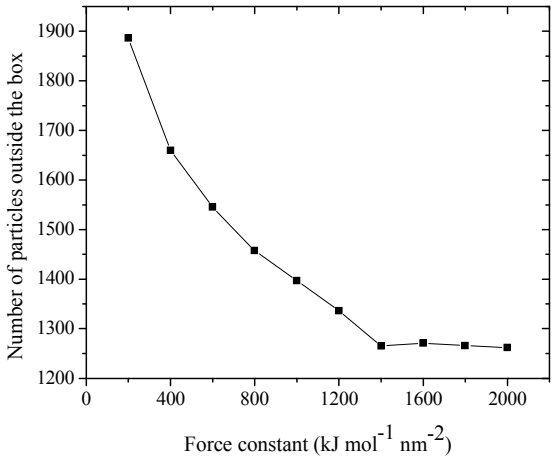

Figure 3.2 : The number of monomers, which leave the designated particle domain in a simulation of 5 ns duration at 300 K, depends on the harmonic force constant of the atoms tethered to the anchor points.

Also the force constant k of the anchor point potential is an important parameter of the method, as it has an influence on the number of particles that can leave the box, leading to polymer chains protruding into the continuum region. If the spring is too slack, the anchored particles can move out of the way, when un-anchored particles are squeezed out of the particle domain. This is clearly visible in Fig. 3.2, which shows the final number of monomers, which have escaped from the particle domain within 5 ns of simulation, as a function of the anchor point force constant, for an SBC simulation at 300 K with 7262 anchor points. The curve saturates at k=1400 kJ mol^{-1} nm^{-2}. Thus, this is the minimum force constant to be used. For the other number of anchor points collected in table 1 we found the same value for force constant. An additional requirement on the choice of k is that the tethering should not lead to an increase of the highest vibrational frequencies, so that no shorter timestep is necessary. This condition is fulfilled, since the stiffest effective force constants in the systems are those of the nearest-neighbour bonded interactions. From the curvature of this potential they are also estimated to be approximately 1400 kJ mol^{-1} nm^{-2}. As is shown in Table 3.1, the choice of k = 1400 kJ mol^{-1} nm^{-2} (used in this work if not indicated otherwise) not only minimizes the particle escape and allows to maintain the time step, but also keeps the correct density in the central MD region.

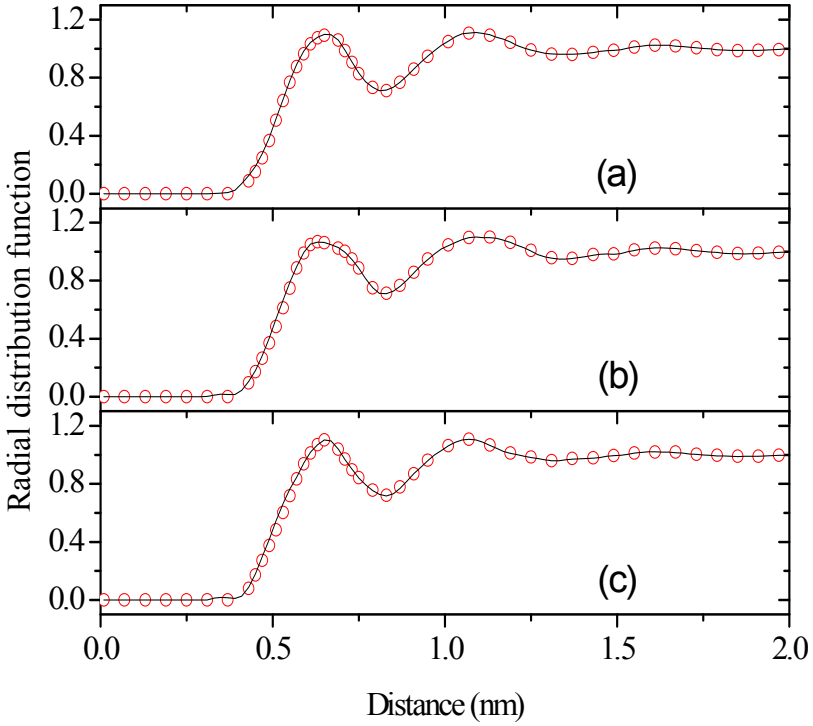

Figure 3.3. Nonbonded radial distribution functions (excluding first and second neighbours on the same chain) for polystyrene chains of 20 monomers at 300 K; solid line: periodic boundary conditions; circles: stochastic boundary conditions, molecular dynamics region only. (a) between R monomers; (b) between S monomers; (c) between R and S monomers.

Also the global structure of the polymer chains in the MD region (end-to-end distance and radius of gyration, Table 3.1) is identical in PBC and SBC simulations and is independent of the number of anchor points. The same holds for the short-range structure as captured by the radial distribution functions (RDF). This is shown in Fig. 3.3, where the three RDFs (RR, SS, and RS, corresponding to superatoms describing monomers of different chirality) are shown. The SBC curves displayed were obtained from the simulation with 7262 anchor points; the agreement is equally perfect for the other SBC simulations.

The dynamical behavior of the polymer chains is characterized by the autocorrelation function of the end-to-end vector $\frac{<\boldsymbol{R}(0).\boldsymbol{R}(t)>}{<R^2>}$. In Fig. 3.4 we compare the SBC (MD region only, simulation with 7262 anchor points) and PBC results. In both cases the autocorrelation function decays to zero in 800 ps. To determine the relaxation time (τ), the autocorrelation functions were fitted to exponential curves $\exp(-t/\tau)$. The relaxation times amount to 162.5 ps for PBC and 161.8 ps for SBC. A similar agreement is found for other numbers of anchor points.

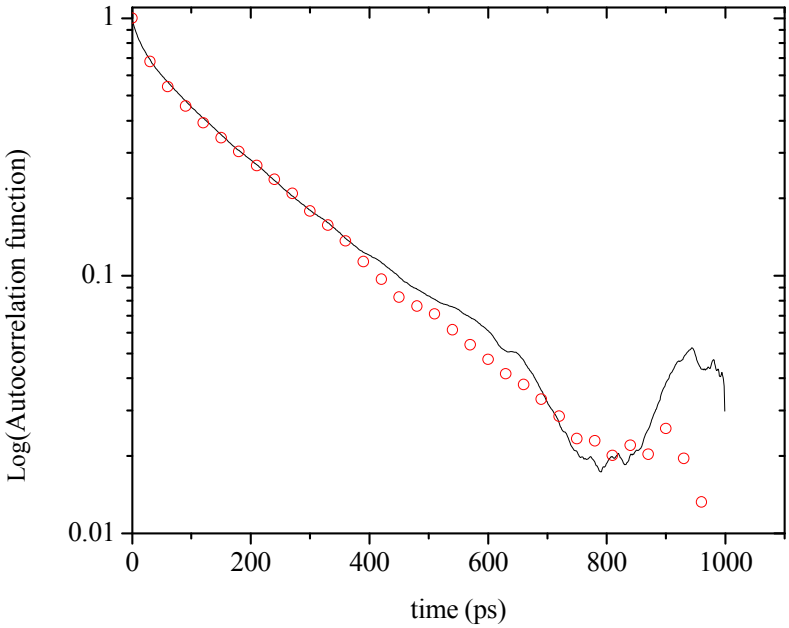

Figure 3.4. Autocorrelation function of the end-to-end vector for polystyrene chains of 20 monomers at 300 K. Solid line: periodic boundary conditions; circles: stochastic boundary conditions, molecular dynamics region only.

Condition	Number of anchor points	Density (kg/m^3)	Temperature (K)
PBC	-	932.0±1.2	500±0.87
SBC	6219	(924.6±1.9) 930.8±1.9	(500.4±2.5) 501.8±2.2
SBC	9158	(925.9±1.3) 931.8±1.3	(500.6±1.4) 500.6±2.1
SBC	11593	(925.7±0.3) 931.7±1.5	(499.9±2.2) 500.9±2.1

TABLE 3.2: Properties of melts of polystyrene chains of 10 monomers at 500 K. Comparison of properties evaluated in the molecular dynamics region calculated under nonperiodic stochastic-boundary conditions (SBC) with different numbers of anchor points and under periodic boundary conditions (PBC). For all SBC simulations, the DPD parameters are σ=10 pN ps$^{1/2}$ and γ=7.2 pN ps nm^{-1} and the anchor point force constant is k=1400 kJ mol^{-1} nm^{-2}. Values in parentheses refer to the systems before compression (see text).

In order to further check the correctness of the SBC approach, we conducted a second set of simulations with a different chain length (6000 chains of 10 monomers) and temperature (500 K). In the preparation of the PBC and SBC systems, we proceeded analogously to the previous case (20-mers, 300 K). The final box length in equilibrium was ~22.3 nm. The cutoff radius was kept and, thus,

the setup of the SBC box was the same. The thicknesses of the boundary and DPD regions were again 1.7 nm and 0.8 nm, respectively. With these dimensions the length of the MD region was roughly 17.3 nm, and there were 31874 DPD and 28126 MD particles. We simulated this system with different numbers of anchor points. In Table 3.2 it can be seen that the outer DPD thermostat provides an efficient temperature control in the inner region. After the optimization of the force constant there is a small deviation in the density, which is about 0.8% too low, irrespective of the number of anchor points used (Table 3.2, values in parentheses). This small deviation has, however, a large influence on the pressure in the MD region (which is calculated to be between -1100 and -2500 kPa) and also on the forces on the anchor points. To overcome these problems, we equilibrated the box until the desired pressure of 101.3 kPa was reached. During the correction of pressure we fixed the number of anchor points and the value of the force constant. This approach is similar in spirit to *NpT* simulations with a Berendsen barostat[48]. Instead of changing the box size in a periodic simulation, however, we scaled the positions of the anchor points and all atoms in a weak-coupling scheme with coupling time 5000 fs and isothermal compressibility 1.0×10^{-6} kPa^{-1}. In contrast to the periodic *NpT* approach, we calculated the local pressure[49] only in the MD region. After 5 ns of *NpT* equilibration we fixed the anchor points to their positions averaged over another 5 ns. Then we simulated for another 10 ns. The average densities (Table 3.2; values without parentheses) agree with the PBC reference value within the error bars. Note that the manual adjustment of the anchor points to reproduce the pressure in the interior of the MD region was only necessary because of the still missing external pressure. In the final hybrid FE-MD scheme, the FE environment will take the role of moving the anchor points in response to deformation forces, which include the pressure components in the MD region.

Due to the exchange between the MD and DPD region, the particle number in the MD domain was not constant (Fig. 3.5). It fluctuated between 27600 and 27900 (about 1%) around its equilibrium average. Thus, the migration between the MD and DPD region did not lead to a flow into one direction.

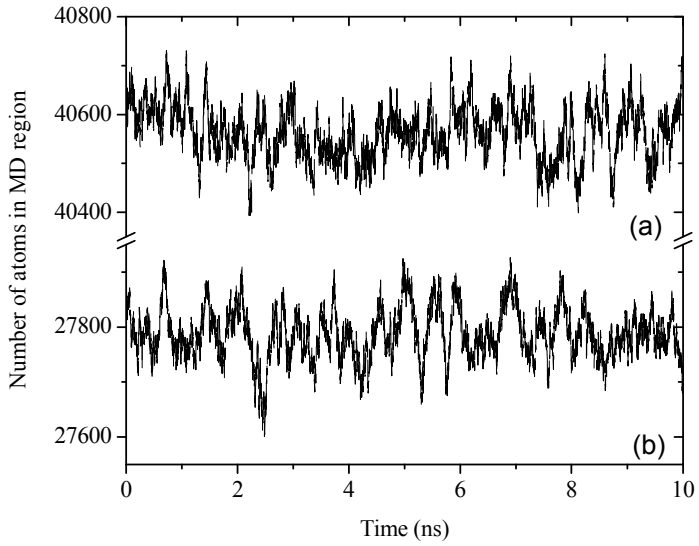

Figure 3.5. Number of atoms in the MD region from stochastic-boundary simulations for polystyrene chains of (a) 20 monomers at 300 K (b) 10 monomers at 500 K.

3.5. Summary

A scheme has been developed for performing molecular dynamics simulations on polymeric materials under nonperiodic stochastic boundary conditions. It has been designed to allow the embedding of a particle domain treated by molecular dynamics into a continuum environment treated by finite elements. The scheme combines the use of anchor points, to which a small number of particles in the boundary region is harmonically tethered, as a means of confining the particle region, with the use of dissipative particle dynamics as stochastic equations of motion to ensure the dissipation of energy and to thermostat the simulation. While none of the individual ingredients is new, the combination described here is particularly suited for hybrid simulations. The use of flexibly tethered particles as confinement is less perturbative to the core of the particle region than the sometimes used position-constrained particles. The employment of anchor points allows an efficient and flexible transmission of forces into the finite-element domain, much more than containers based on hard walls or static potentials of mean force. It also provides a mechanism to allow - within certain limits - shapes and deformations of the particle domain, in contrast to some nonperiodic schemes, which enforce, for example, a spherical shape. Dissipative-particle dynamics near the boundary ensures that the particle dynamics is sufficiently randomized and that the heat bath of the degrees of freedom, which are missing beyond the boundary, is better emulated than with straight molecular dynamics.

Moreover, its ability to remedy the artificially enhanced mobility of coarse-grained polymer models is well documented.

The nonperiodic boundary conditions have been tested for two systems of atactic short-chain polystyrene described with a standard coarse-grained model. In both cases, the nonperiodic boundary conditions reproduce excellently thermodynamic quantities such as the density and temperature, the global structure (radius of gyration, end-to-end distance), local structure (radial distribution functions) and the dynamics (relaxation time of the end-to-end vector) of molecular dynamics simulations of these systems under regular periodic boundary conditions. Note that in both cases, the nonperiodic simulation cells were rectangular. It may be concluded that the polystyrene in the inner region of the particle domain (called MD region above) behaves as though it were surrounded by an infinite mass of particulate polystyrene. We thus feel well equipped to combine the present treatment of the particle domain with a finite element surrounding to a hybrid method. Its implementation and testing is underway and will be described in a later paper.

References

1 M. P. Allen and D. J. Tildesley, *Computer Simulation of Liquids* (Oxford, Clarendon, 1987).
2 G. King and A. Warshel, J. Chem. Phys. **91,** 3647 (1989).
3 A. H. Juffer and H. C. J. Berendsen, Mol. Phys **79,** 623 (1993).
4 D. Beglov and B. Roux, J. Chem. Phys. **100,** 9050 (1994).
5 V. Lounnas, S. K. Lüdemann, and R. C. Wade, Biophys. Chem. **78,** 157 (1999).
6 G. Petraglio, M. Ceccarelli, and M. Parrinello, J. Chem. Phys. **123,** 044103 (2005).
7 G. Brancato, A. D. Nola, V. Barone, and A. Amadei, J. Chem. Phys. **122,** 154109 (2005).
8 G. Brancato, N. Rega, and V. Barone, Chem. Phys. Lett. **483,** 177 (2009).
9 M. Berkowitz and J. A. McCammon, Chem. Phys. Lett. **90,** 215 (1982).
10 C. L. Brooks and M. Karplus, J. Chem. Phys. **79,** 6312-6324 (1983).
11 A. Brünger, C. L. Brooks, and M. Karplus, Chem. Phys. Lett. **105,** 495 (1984).
12 M. J. Mandell, J. Stat. Phys. **15,** 299 (1976).
13 L. R. Pratt and S. W. Haan, J. Chem. Phys. **74,** 1864 (1981).
14 L. R. Pratt and S. W. Haan, J. Chem. Phys. **74,** 1873 (1981).
15 B. Dünweg and K. Kremer, Phys. Rev. Lett. **66,** 2996 (1991).
16 I.-C. Yeh and G. Hummer, J. Chem. Phys. B **108,** 15873 (2004).
17 M. González-Melchor, P. Orea, J. López-Lemus, F. Bresme, and J. Alejandre, J. Chem. Phys. **122,** 094503 (2005).
18 P. E. Smith and B. M. Pettitt, J. Chem. Phys. **105,** 4289 (1996).
19 P. H. Hünenberger and J. A. McCammon, J. Chem. Phys. **110,** 1856 (1999).
20 P. Wriggers, *Nonlinear finite element methods* (Springer, Heidelberg, 2008).
21 K. M. Mohamed and A. A. Mohamad, Microfluid. Nanofluid. **8,** 283 (2010).
22 S. Attinger and P. Koumoutsakos(Eds), *Multiscale Modelling and Simulation, Lecture Notes in Computational Science and Engineering 39* (Springer, Heidelberg, 2004).
23 S. T. O'Connell and P. A. Thompson, Phys. Rev. E **52,** R5792 (1995).

24 E. M. Kotsalis, J. H. Walther, and P. Koumoutsakos, Phys. Rev. E **76,** 016709 (2007).
25 T. Werder, J. H. Walther, and P. Koumoutsakos, J. Comput. Phys. **205,** 373 (2005).
26 R. Delgado-Buscalioni, K. Kremer, and M. Praprotnik, J. Chem. Phys. **131,** 244107 (2009).
27 E. G. Flekkøy, R. Delgado-Buscalioni, and P. V. Coveney, Phys. Rev. E **72,** 026703 (2005).
28 E. B. Tadmor, M. Ortiz, and R. Phillips, Philosophical Magazine A **73,** 1529 (1996).
29 R. Miller, M. Ortiz, R. Phillips, V. Shenoy, and E. B. Tadmor, Engineering Fracture Mechanics **61,** 1899 (1998).
30 M. Ortiz and J. Knap, J. Mech. Phys. Solids **49,** 2085 (2001).
31 L. E. Shilkrot, W. A. Curtin, and R. E. Miller, J. Mech. Phys. Solids **50,** 2085 (2002).
32 L. E. Shilkrot, R. E. Miller, and W. A. Curtin, J. Mech. Phys. Solids **52,** 755 (2004).
33 T. Belytschko and S. P. Xiao, International Journal for Multiscale Computational Engineering **1,** 115-126 (2003).
34 P. T. Bauman, H. B. Dhia, N. Elkhodja, J. T. Oden, and S. Prudhomme, Comput. Mech. **42,** 511 (2008).
35 S. Pfaller, G. Possart, P. Steinmann, M. Rahimi, F. Müller-Plathe, and M. C. Böhm, Comput. Mech. (submitted).
36 F. Müller-Plathe, ChemPhysChem **3,** 754-769 (2002).
37 R. Delgado-Buscalioni, K. Kremer, and M. Praprotnik, Journal of Chemical Physics **128** (2008).
38 R. D. Groot and P. B. Warren, J. Chem. Phys. **107,** 4423 (1997).
39 H. Meyer, O. Biermann, R. Faller, D. Reith, and F. Müller-Plathe, J. Chem. Phys. **113,** 6265 (2000).
40 F. Müller-Plathe, Soft Materials **1,** 1 (2003).
41 T. Spyriouni, C. Tzoumanekas, D. Theodorou, F. Müller-Plathe, and G. Milano, Macromolecules **40,** 3876 (2007).
42 P. Español and P. Warren, Europhys. Lett. **30,** 191 (1995).
43 H.-J. Qian, C. C. Liew, and F. Müller-Plathe, Phys. Chem. Chem. Phys **11,** 1962 (2009).
44 I. Vattulainen, M. Karttunen, G. Besold, and J. M. Polson, J. Chem. Phys. **116,** 3967 (2002).
45 H. Qian, P. Carbone, X. Chen, H. A. Karimi-Varzaneh, and F. Müller-Plathe, Macromolecules **41,** 9919 (2008).
46 G. Milano and F. Müller-Plathe, J. Chem. Phys. B **109,** 18609 (2005).
47 H. A. Karimi-Varzaneh, H.-J. Qian, X. Chen, P. Carbone, and F. Müller-Plathe, J. Comp. Chem. (in press).
48 H. J. C. Berendsen, J. P. M. Postma, W. F. v. Gunsteren, A. DiNola, and J. R. Haak, J. Chem. Phys. **81,** 3684 (1984).
49 H. Heinz, W. Paul, and K. Binder, Phys. Rev. E **72,** 066704 (2005).

4. An Arlequin-based method to couple molecular dynamics and finite element simulations of amorphous polymers and nanocomposites*

Abstract

A new simulation technique is introduced to couple a flexible particle domain as encountered in soft-matter systems and a continuum which is solved by the Finite Element (FE) method. The particle domain is simulated by a molecular dynamics (MD) method in coarse grained (CG) representation. On the basis of computational experiences from a previous study, a staggered coupling procedure has been chosen. The proposed MD-FE coupling approximates the continuum as a static region while the MD particle space is treated as a dynamical ensemble. The information transfer between MD and FE domains is realized by a coupling region which contains, in particular, additional auxiliary particles, so-called anchor points. Each anchor point is harmonically bonded to a standard MD particle in the coupling region. This type of interaction offers a straightforward access to force gradients at the anchor points that are required in the developed hybrid approach. Time-averaged forces and force gradients from the MD domain are transmitted to the continuum. A static coupling procedure, based on the Arlequin framework, between the FE domain and the anchor points provides new anchor point positions in the MD-FE coupling region. The capability of the new simulation procedure has been quantified for an atactic polystyrene (PS) sample and for a PS–silica nanocomposite, both simulated in CG representation. Numerical data are given in the linear elastic regime which is conserved up to 3% strain. The convergence of the MD-FE coupling procedure has been demonstrated for quantities such as reaction forces or the Cauchy stress which have been determined both in the bare FE domain and in the coupled system. Possible applications of the hybrid method are shortly mentioned.

4.1. Introduction and outline

Continuum mechanics, a field-based theory that can be treated numerically by the widely used Finite Element (FE) method, is a very powerful tool to simulate the macroscopic mechanical behaviour

*Pfaller, S. (corresponding author), Rahimi, M. (corresponding author), Possart, G., Steinmann, P., Müller-Plathe, F., & Böhm, M. C. Submitted to Computer Methods in Applied Mechanics and Engineering. Sections 2.1, 2.2 and 4.1 have been contributed by Rahimi, M.

of e.g. solids. Unfortunately, it is less suited in cases where molecular or even atomistic details become important to capture the phenomena of interest. On the other hand, such particle-based information becomes accessible either by Monte Carlo (MC) or molecular dynamics (MD) calculations. The application of MC or MD simulations for macroscale problems, however, is computationally prohibitive due to the large number of particles required and the corresponding degrees of freedom. Typical system sizes in MD calculations are in the range of nanometers, while typical orders of magnitude in the time steps amount to femtoseconds, which allow simulation times of some nanoseconds. Compared to the time scales and system sizes relevant in engineering problems of continuum mechanics, the time and length scales considered in MD simulations are, thus, orders of magnitude smaller. The advantages of both theoretical tools can be combined within hybrid techniques which allow the coupling of a particle description to a continuum one or the coupling of particle domains with different resolutions. Such methods are particularly useful under conditions where molecular details are relevant only in smaller spatial regions of the studied sample such as solid-fluid or solid-polymer interfaces, while particle properties are not required in the remaining regions which have bulk behaviour. In such systems the efficiency of continuum mechanics can be combined with the accuracy of MD simulations.

In the past years an increasing number of publications have proposed combinations of particle-based models with field-based models in hybrid schemes. Within this contribution, we will concentrate on hybrid schemes which are based on a spatial decomposition into a particle region and a much larger continuum. Unlike this, so-called parameter inheritance schemes have become more popular since they can be formulated more easily. These methods allow computing material parameters at the molecular level and use them as input in the subsequent continuum simulations. Quite similarly, single-chain-in-mean-field models have been developed, cf. e.g. [1], [2], and [3]. Hybrid approaches can be divided into a group for hydrodynamics problems and one for structural mechanics problems. We will focus here on the second type, which often deal with the failure of crystalline systems. However, there are only few adaptions to amorphous systems, which we will concentrate on in this contribution. Well-known examples are the quasi-continuum methods as they were introduced and employed e.g. in [4], [5], and [6]. Here, selected particles are moved by an affine deformation of the elements since they are attached to FE nodes or edges.

Beyond these kinds of coupling methods, extensions towards amorphous materials have been made by the so-called bridging domain method introduced by Belytschko and co-workers e.g. in [7] and [8], employed in modelling studies of carbon nanotubes as well as other systems, cf. [9] and [10]. Quite similar, Ben Dhia and Rateau developed a hybrid scheme called the Arlequin method, cf. [11],

[12], and [13]. Originally used as a tool to couple FE domains of different resolutions, the Arlequin method has been employed later in hybrid simulations of atomistic and continuum models, cf. e.g. [14].

The Arlequin method considers a pure particle region without any underlying FE description, i.e. it does not require the particles to be arranged in a lattice. Instead, a handshake region is introduced in which the FE domain and the particle region overlap. Here the deformation of the continuum and the displacements of the particles are required to match in a weak sense. Thus, it is a suitable candidate to model amorphous materials like polymers. Although there is already a small number of publications available dealing with generic polymer models, by e.g. the group of Prudhomme, cf. [15] and [16], no procedure has been described yet that allows a coupling between an FE domain and a particle system computed with the commonly used MD tools at finite temperature.

As mentioned above, engineering problems captured by continuum mechanics and microscopic considerations treated by particle-based methods differ tremendously in time and length scales. Thus, both aspects have to be considered carefully here: on the one hand, the spatial scale bridging as introduced here seems to be feasible. Its formulation is supported by the publications on static continuum–particle coupling procedures discussed above. On the other hand, the coupling of time scales that are orders of magnitude different is a very crucial part of any coupling scheme, and it has not been solved yet. In this context, we refer to the group of de Borst and co-workers, which has investigated the spatial and temporal coupling and discussed its advantages and drawbacks in [17].

In this contribution, we have developed a new hybrid technique for polymers to couple a particle domain to a continuum. In order to avoid conceptual problems arising from the different time scales in the respective regions, the continuum is treated purely static while only the particle domain is computed dynamically. This seems to be reasonable due to the large difference between the dynamics on the macroscale and that of the particles: any time-dependent processes on a scale relevant for engineering problems would be quasi-static compared to the dynamics at the level of particles. In the following, we will sketch the main components of the coupling procedure and point to the corresponding sections where these aspects will be discussed in detail.

First, the MD domain treated in the present coupling scheme is large in comparison to dimensions usually encountered in atomistic MD simulations. Therefore the MD region has to be treated by a coarse grained (CG) technique [18], [19], [20] which reduces the degrees of freedom by grouping a number of atoms together into so-called superatoms or CG beads. The CG potentials used in the present work have been derived by iterative Boltzmann inversion (IBI) of atomistic potentials [21]. Quite generally the CG mapping offers access to simulations which are computationally

unfeasible in a purely atomistic model. To perform coupled MD-FE simulations the conventional periodic boundary conditions (PBCs) had to be replaced by nonperiodic stochastic ones (SBCs) [22]. In the boundary region of the developed coupling scheme we have defined a set of auxiliary particles, so-called anchor points. They are harmonically coupled to the MD particles. The anchor points form a set of fixed particles without interaction between them that do not move during the MD equilibration procedure. Hence, they can be coupled to a static continuum as mediators between the different domains. This static coupling will be realized with the help of the Arlequin method mentioned above. Thus, the spatial set-up of our hybrid method consists of three main regions as sketched in Figure 1:

1. a pure particle domain Ω^d;
2. a bridging domain Ω^b where the particle region overlaps with the continuum. This region contains the anchor points;
3. a pure continuum Ω^c, discretized by finite elements.

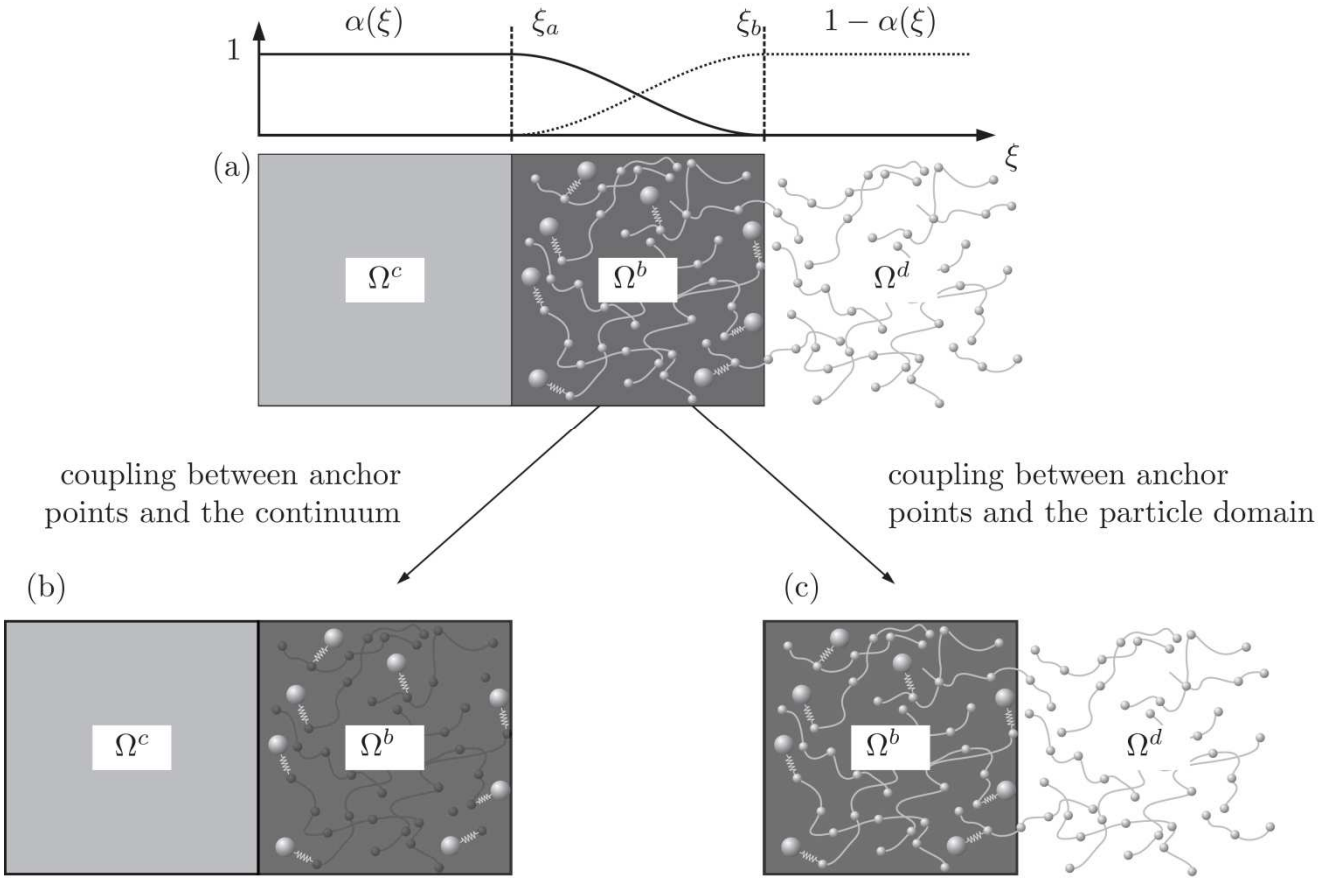

Figure 1: Spatial coupling: continuum Ω^c, bridging domain Ω^b, and particle domain Ω^d; small spheres: MD particles, large spheres: anchor points; the weighting factor $\alpha(\xi)$ as well the variable ξ will be explained later; the complete spatial setup (a) is separated into a coupling between the anchor

points and the continuum (b) and into a coupling between the anchor points and the particle domain (c).

The scale bridging procedure proposed here is subdivided into a static coupling between the anchor points and the continuum (cf. part (b) in Figure 1) and into its counterpart which tethers the anchor points to the particle domain (cf. part (c) in Figure 1). We will subsequently discuss the respective schemes as follows:

- Sections 4.2.1 and 4.2.2: dynamic coupling between anchor points and particles as well as necessary modifications of the particle domain
- Sections 4.2.2, 4.2.3.1, and 4.2.3.2: static coupling between anchor points and the continuum, introduction of the Arlequin method

It has to be remarked here that, due to the subdivision into a static and a dynamic scheme, the usual tools to solve the continuum and the particle domain, i.e. the conventional FE and MD procedures, can be applied with rather small modifications. Thus, algorithms and machines highly specialized for the respective tools can be employed which is important especially with respect to the very time consuming MD simulations.

In order to embed both schemes into a single computational procedure, a staggered algorithm is used that will be presented later. Without going into detail, only the conceptual ideas are discussed here, for a detailed description we refer to Section 3 and Figure 5.

After applying a load to the undeformed continuum, the resulting deformation is transferred via the bridging region and anchor points to the MD domain which is thus distorted. Consequently, a new equilibrium has to be computed for the MD domain. This leads to reaction forces acting on the anchor points and, therefore, also on the continuum. Then, the FE domain has to be re-equilibrated, too, and takes a new configuration. This causes another distortion of the MD domain which implies that the coupling procedure has to be continued until the coupled system takes its global energy minimum.

Since the present article intends to introduce and demonstrate a new hybrid method, it is applied to an established system. We have chosen atactic polystyrene (PS) as well as a PS–silica nanocomposite in CG representation as model systems. The mapping scheme of Qian et al. [23] is used for the coarse graining of the polymer, i.e. each molecular repeat unit is described by a single bead. In atactic PS two different absolute configurations are found in the molecular fragments; they cause two types of CG beads which differ in their potential. In the coarse graining of the silica nanoparticle each SiO_2 unit is mapped by a CG bead. Details of the CG procedure can be found in a recent paper of Rahimi et al. [24]. For all MD simulations the in-house computer code IBiSCO [25] working with tabulated potentials is employed.

4.2 Modeling foundations

In this section, a short overview of the basics of continuum mechanical and particle-based modeling is given. Additionally, some aspects of coupling different domains are discussed. Beginning from the particle system and its extension by anchor points, the coupling between anchor points and the continuum which is realized by the Arlequin method is presented.

4.2.1 Particle system and its dynamic coupling to anchor points

Since the particle domain is surrounded by a continuum, PBCs as the usual procedure to avoid surface effects in MD cannot be used. Thus, we had to introduce non-periodic boundary conditions which should meet two main requirements:

1. it has to be ensured that artefacts of the dynamics are kept to a minimum;
2. an information transfer (forces and deformations) between the continuum and the particle region has to be realized.

As stated in the introduction, we have developed a modified MD tool based on stochastic boundary conditions, which satisfies these demands. The procedure was described in detail in [22], where it had been applied to polystyrene. Thus, we here only give a brief description of its features.

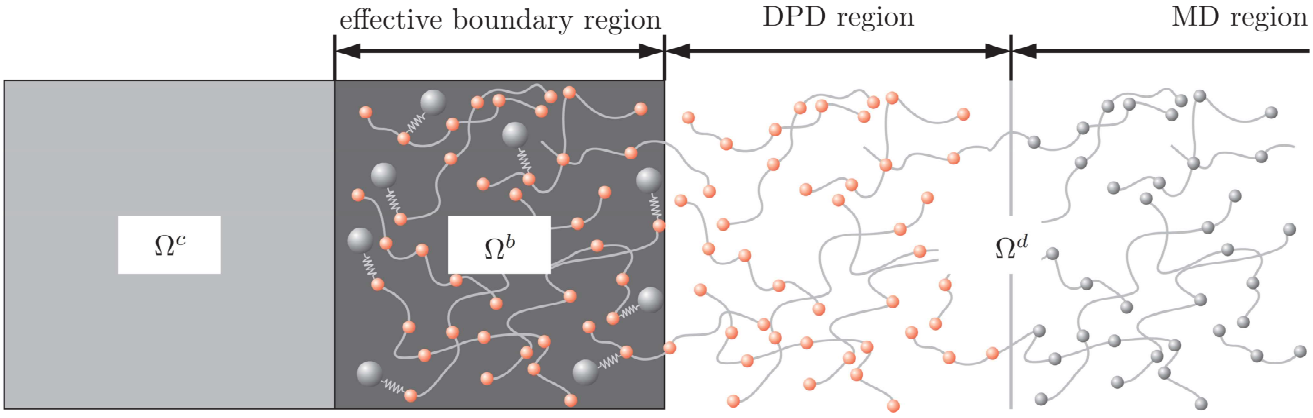

Figure 2: Spatial setup of stochastic boundary conditions: continuum Ω^c, bridging domain Ω^b, and particle domain Ω^d as introduced in Section 4.1; large spheres: anchor points; small spheres (gray): particles moving due to MD equations of motion in the MD region; small spheres (red): particles moving due to DPD equations of motion in the effective boundary region as well as in the DPD region.

Two regions are defined in the boundary layer, cf. Figure 2: on the one hand the effective boundary region, on the other hand a dissipative particle dynamics (DPD) region, cf. e.g. [25], [26], and [27]. Using SBCs, the actual MD domain is embedded into the DPD region, which itself is enclosed by the effective boundary region. To minimize the surface effects at the interface with the

continuum, stochastic dynamics is employed. Therefore, the particles in the DPD region as well as in the effective boundary region move according to the DPD equations of motion which we will not comment on in detail here. The stochastic dynamics pretends a large number of particles outside the MD region and acts as an external bath that is able to control the temperature of the MD region. The effective boundary region, which overlaps with the continuum, coincides with the bridging domain Ω^b of the static coupling between the particle domain and the continuum. In this region, anchor points are introduced as auxiliary particles which do not move during the MD equilibration. They confine the particles to the designated MD region and prevent them from escaping. Furthermore, the anchor points exert a pressure on the system to define a certain thermodynamic state in the MD region. To each anchor point I, one particle is connected by a harmonic potential

$$E_{MD\,I}^{int} = \frac{1}{2} k_I \,|\, \mathbf{R}_I^{MS} - \mathbf{r}_I^{MD} \,|^2, \tag{1}$$

with the force constant k_I, which is of the same order of magnitude as the bond force constant used in the pure MD domain, the position of the anchor point $\mathbf{R}_I^{MS}$, and the current position $\mathbf{r}_I^{MD}$ of the MD particle it is tethered to. In the next section, we will explain in detail the terminology used here. By this harmonic potential, the evaluation of the non-trivial interactions in the adopted force field is simplified significantly. Thus, the gradients of forces acting on anchor points are available to second order optimization methods that are used to solve the system of equations that describes the static coupling between anchor points and the continuum. Furthermore, it has to be mentioned that in our investigations the force constants k_I are all identical. As stated above, the static anchor points are coupled to the continuum based on the Arlequin method which makes them transmitters for the information transfer between the continuum and the pure particle domain: on the one hand, the particle domain exerts forces on the anchor points which can be transferred as a time average to the continuum. On the other hand, the continuum is able to pass its deformation to the particle domain by changing the positions of anchor points. Another benefit of introducing anchor points is the fact that their number is much lower than that of the remaining MD particles, which leads to a significant reduction of degrees of freedom that have to be coupled to the continuum. The details will be given below.

4.2.2 Interaction between anchor points and superatoms

In order to prepare the coupling of anchor points to the continuum, the interaction between anchor points and superatoms as discussed in Section 4.2.1 are described more in detail. Here, the focus is on

the change of anchor point positions due to the continuum deformation. Without knowing yet the relation between anchor point displacements and the continuous displacement field, cf. Section 4.2.3.2, the change of anchor point positions with respect to the positions of the MD particles is investigated. Please note that during the equilibration of the continuum the MD particles remain fixed which will be presented in detail in Section 4.3. In order to distinguish between anchor points and superatoms, we use the following terminology: variables referring to superatoms, i.e. "real" MD particles, are denoted by the superscript "MD", whereas variables describing anchor point values are labelled by the superscript "MS", which marks them as static particles, being part of a "molecular statics" region.

Figure 3 displays the interaction of an arbitrary MD particle (position vector $\mathbf{R}_I^{MD}$) and the anchor point I it is tethered to (initial position $\mathbf{R}_I^{MS}$, position after deformation $\mathbf{r}_I^{MS}$). During the MD equilibration, the positions of anchor points are spatially fixed while the MD particles are allowed to move according to their interactions with other MD particles. Opposite to this, we focus here on the equilibration of the continuum, where the positions of the MD particles remain fixed and the anchor points are moved according to the deformation of the continuum.

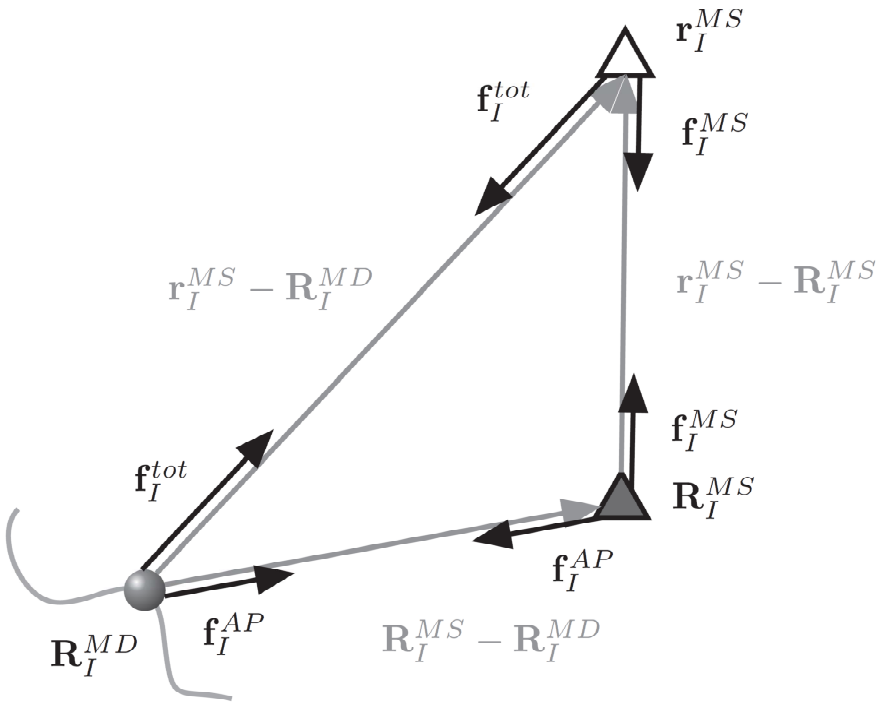

Figure 3: Interaction between superatom I (position $\mathbf{R}_I^{MD}$) and its associated anchor point (initial position $\mathbf{R}_I^{MS}$, current position after deformation of the continuum $\mathbf{r}_I^{MS}$); force $\mathbf{f}_I^{AP}$ between superatom and anchor point before deformation, force $\mathbf{f}_I^{tot}$ between superatom and anchor point after deformation, and $\mathbf{f}_I^{MS} = \mathbf{f}_I^{tot} - \mathbf{f}_I^{AP}$

The interaction between an anchor point and its MD coupling partner is realized by a harmonic interaction potential

$$E_{MS\,I}^{int} = \frac{1}{2} k_I \,|\, \mathbf{r}_I^{MS} - \mathbf{R}_I^{MD} \,|^2, \tag{2}$$

which is similar to (1), but formulated from the continuum point of view. Here, the anchor points are moved according to the continuum deformation whereby the superatoms remain fixed. The derivative of (2) with respect to the current anchor point position, i.e. the section force, can be written as

$$\begin{aligned} \mathbf{f}_I^{tot} &= -\frac{\partial E_{MS\,I}^{int}}{\partial \mathbf{r}_I^{MS}} = -k_I \left[\mathbf{r}_I^{MS} - \mathbf{R}_I^{MD} \right] \\ &= -k_I \left[\mathbf{r}_I^{MS} - \mathbf{R}_I^{MS} \right] - k_I \left[\mathbf{R}_I^{MS} - \mathbf{R}_I^{MD} \right] = \mathbf{f}_I^{MS} + \mathbf{f}_I^{AP} \end{aligned} \tag{3}$$

In (3), the force $\mathbf{f}_I^{tot}$ acting on the anchor point due to its interaction with the related MD particle, is separated into $\mathbf{f}_I^{AP} \neq \mathbf{f}_I^{AP}\left(\mathbf{r}_I^{MS}\right)$ and $\mathbf{f}_I^{MS} = \mathbf{f}_I^{MS}\left(\mathbf{r}_I^{MS}, \mathbf{R}_I^{MS}\right)$ which will be used in Section 4.3 when setting up the detailed coupling algorithm.

Furthermore, $\mathbf{f}_I^{MS}$ can be rewritten as

$$\begin{aligned} \mathbf{f}_I^{MS} &= -\mathbf{K}_I^{AP} \cdot \left[\mathbf{r}_I^{MS} - \mathbf{R}_I^{MS} \right] = -\mathbf{K}_I^{AP} \cdot \mathbf{w}_I \quad \textit{with} \\ \mathbf{K}_I^{AP} &= \begin{bmatrix} k_I & 0 & 0 \\ 0 & k_I & 0 \\ 0 & 0 & k_I \end{bmatrix}, \end{aligned} \tag{4}$$

where $\mathbf{w}_I = \mathbf{r}_I^{MS} - \mathbf{R}_I^{MS}$ denotes the displacement of the anchor point and $\mathbf{K}_I^{AP}$ is the diagonal matrix of force constants. Since there is no interaction with other anchor points considered, the force acting on each anchor point is only a function of its relative position to the respective superatom.

4.2.3 Continuum and its static coupling to anchor points

In this section, the static coupling between the continuum and the anchor points is described. First of all, the basics of continuum mechanics will be sketched, followed by the introduction of the Arlequin method. After that, both, the continuum formulations as well as the results from Section 4.2.2 will be embedded into the Arlequin framework and the spatial discretization of the static coupling will be discussed.

4.2.3.1 Continuum modeling

In continuum mechanics, a vector-valued function

$$: \mathbf{X} \mapsto \mathbf{x} = \quad (\mathbf{X}, t) \tag{5}$$

is considered which maps the material configuration Ω_0^c of a continuous body to the spatial configuration Ω_t^c as sketched in Figure 4. $\mathbf{X}$ denotes a point in the undeformed material configuration, whereas $\mathbf{x}$ is the same point in the deformed spatial configuration. Furthermore, the deformation gradient

$$\mathbf{F} = \frac{\partial}{\partial \mathbf{X}} = \frac{\partial}{\partial \mathbf{X}}[\mathbf{X} + \mathbf{u}] = \mathbf{I} + \frac{\partial \mathbf{u}}{\partial \mathbf{X}} \tag{6}$$

is introduced with displacement vector $\mathbf{u} = \mathbf{x} - \mathbf{X}$ and identity $\mathbf{I}$. In order to describe the deformation of a body, the internal potential energy

$$E_c^{int} = \int_{\Omega_0^c} \Psi(\mathbf{F}) dV \tag{7}$$

is used, whereby the scalar function $\Psi = \Psi(\mathbf{F})$ denotes the strain or stored energy density while V is the volume of the body in the material configuration. Each deformation of the body results in a change of the internal potential energy. In case of conservative systems as investigated here, there is no dissipation of energy due to the deformation.

The external energy introduced to the body results from surface tractions $\mathbf{T}$ and body forces $\mathbf{b}$. With dA denoting area elements in the material configuration we obtain

$$E_c^{ext} = \int_{\partial_\sigma \Omega_0^c} \mathbf{u} \cdot \mathbf{T} \, dA + \int_{\Omega_0^c} \rho_0 \, \mathbf{u} \cdot \mathbf{b} \, dV. \tag{8}$$

In (8), the Neumann boundary $\partial_\sigma \Omega_0^c$ is assumed to be distinct from the Dirichlet boundary $\partial_{\mathbf{u}} \Omega_0^c$, i.e.

$$\partial_\sigma \Omega_0^c \cap \partial_{\mathbf{u}} \Omega_0^c = \varnothing. \tag{9}$$

The total potential energy of a static system finally follows as

$$E_c^{tot} = E_c^{int} - E_c^{ext}. \tag{10}$$

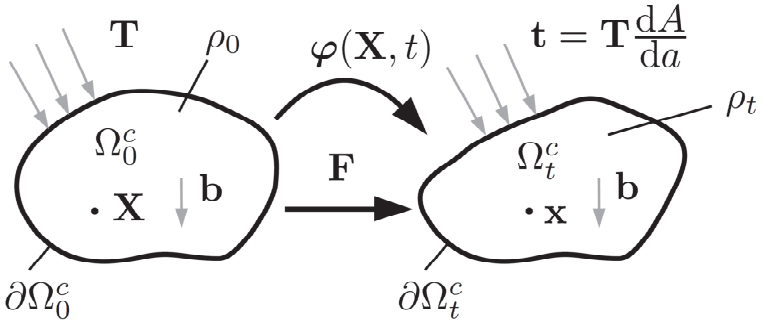

Figure 4: Continuum mechanical setting: deformation map φ from material configuration Ω_0^c to spatial configuration Ω_t^c; quantities are defined in the text

The body is considered as mechanically equilibrated if E_c^{tot} takes its global minimum, i.e. the variation of (10) vanishes:

$$\delta_{\mathbf{u}} E_c^{tot} = \delta_{\mathbf{u}} E_c^{int} - \delta_{\mathbf{u}} E_c^{ext} = 0 \quad \forall \delta\mathbf{u}, \; with \tag{11}$$

$$\begin{aligned} \delta_{\mathbf{u}} E_c^{int} &= \frac{d}{d\varepsilon} \int_{\Omega_0^c} \Psi(\mathbf{F}(\mathbf{u} + \varepsilon\delta\mathbf{u})) dV \,|_{\varepsilon=0} = \\ &= \int_{\Omega_0^c} \underbrace{\frac{\partial}{\partial \mathbf{F}} \Psi(\mathbf{F})}_{\mathbf{P}} : \underbrace{\frac{d}{d\varepsilon} \mathbf{F}(\mathbf{u} + \varepsilon\delta\mathbf{u}) \,|_{\varepsilon=0}}_{\delta\mathbf{F}} dV \quad and \end{aligned} \tag{12}$$

$$\begin{aligned} \delta_{\mathbf{u}} E_c^{ext} &= \frac{d}{d\varepsilon} \int_{\partial_\sigma \Omega_0^c} [\mathbf{u} + \varepsilon\delta\mathbf{u}] \cdot \mathbf{T} \; dA \,|_{\varepsilon=0} + \frac{d}{d\varepsilon} \int_{\Omega_0^c} \rho_0 \, [\mathbf{u} + \varepsilon\delta\mathbf{u}] \cdot \mathbf{b} \; dV \,|_{\varepsilon=0} = \\ &= \int_{\partial_\sigma \Omega_0^c} \delta\mathbf{u} \cdot \mathbf{T} \; dA + \int_{\Omega_0^c} \rho_0 \; \delta\mathbf{u} \cdot \mathbf{b} \; dV \end{aligned} \tag{13}$$

Finally, it has to be remarked that we concentrate in this work on linear elastic systems and small strains. Consequently, the stored energy density can be expressed in terms of the symmetric strain tensor

$$\boldsymbol{\varepsilon} = \frac{1}{2} \left[\frac{\partial \mathbf{u}}{\partial \mathbf{X}} + \left[\frac{\partial \mathbf{u}}{\partial \mathbf{X}} \right]^T \right] \tag{14}$$

(with $\bullet^T$ denoting the transpose) and the material constants λ and μ via

$$\Psi(\boldsymbol{\varepsilon}) = \frac{\lambda}{2} [\boldsymbol{\varepsilon} : \mathbf{I}]^2 + \mu [\boldsymbol{\varepsilon}^2 : \mathbf{I}] \tag{15}$$

4.2.3.2 Arlequin method

As described in Sections 4.2.1 and 4.2.2, the information transfer between continuum and particle domain is realized by anchor points. Since they are not moved within an MD calculation, their coupling to the continuum is of a static nature. We employ the "Arlequin" approach as introduced by Ben Dhia and Rateau, cf. [11], [12] and [13].

The Arlequin framework uses a blending of the energies of the particles and of the continuum via a weighting factor α. Furthermore, a kinematic constraint is introduced to enforce a match of particle and continuum displacements. In the first part of this section, we focus on the necessary modifications of (2) and (10).

The coupling is sketched in Figure 1: the continuum domain Ω^c is coupled to the particle domain Ω^d via a bridging domain Ω^b. Since we focus here on the static coupling of the anchor points to the continuum, the DPD region as defined in Section 4.2.1 is not considered in the following discussion.

In order to weight the energies in the respective domains, we introduce a weighting factor $\alpha(\xi)$ with $\xi = \xi(\mathbf{X})$ in the continuum domain and $\xi = \xi(\mathbf{R}_I)$ in the particle domain. The following conditions hold:

$$\alpha(\xi)\begin{cases} = 1 & in\ \Omega^c \setminus \Omega^b \\ \in [0,1] & in\ \Omega^b \\ = 0 & in\ \Omega^d \setminus \Omega^b \end{cases}. \tag{16}$$

According to [14] and [28], in the bridging domain $\alpha(\xi)$ can be chosen to be constant, linear, cubic or as a trigonometric function:

$$\begin{aligned} \alpha(\xi) &= \frac{1}{2}, \\ \alpha(\xi) &= 1 - \frac{\xi - \xi_a}{\xi_b - \xi_a}, \\ \alpha(\xi) &= \frac{-[\xi - \xi_b]^2 [2\xi - 3\xi_a + \xi_b]}{[\xi_a - \xi_b]^3}, \\ \alpha(\xi) &= 1 - \cos^2\left(\frac{\xi_b - \xi}{2[\xi_b - \xi_a]}\pi\right), \end{aligned} \tag{17}$$

where ξ_a and ξ_b denote the values of ξ at the interface between continuum domain and bridging domain as well as between particle domain and bridging domain.

Adapted energy functions

The energy contributions of the continuum are weighted by the factor α as follows:

$$\hat{E}_c^{int} = \int_{\Omega_0^c} \alpha(\xi(\mathbf{X}))\, \Psi(\mathbf{F})\, dV \tag{18}$$

$$\hat{E}_c^{ext} = \int_{\partial_\sigma \Omega_0^c} \alpha(\xi(\mathbf{X}))\, \mathbf{u} \cdot \mathbf{T}\, dA + \int_{\Omega_0^c} \alpha(\xi(\mathbf{X}))\, \rho_0\, \mathbf{u} \cdot \mathbf{b}\, dV \tag{19}$$

In the particle domain, the weighted energy can be formulated as

$$\hat{E}_d^{int} = \hat{E}_{MS}^{int} + \hat{E}_{MD}^{int}. \tag{20}$$

While the energy of the interaction between the MD particles is denoted by $\hat{E}_{MD}^{int}$, the energy of the harmonic bonds between anchor points and MD particles is subsumed in

$$\hat{E}_{MS}^{int} = \frac{1}{2} \sum_{I=1}^{n^{MS}} \left[1 - \alpha(\xi(\mathbf{R}_I^{MS}))\right] E_{MS\,I}^{int}(\mathbf{R}_I^{MD}, \mathbf{r}_I^{MS}), \tag{21}$$

with n^{MS} being the total number of anchor points. As far as the Arlequin coupling is concerned, it is not necessary to know the exact formulation of $\hat{E}_{MD}^{int}$. Since a change of MD particle positions is not

allowed during the continuum equilibration, $\hat{E}_{MD}^{int}$ remains constant. For sake of completeness, the weighted external energy is given:

$$\hat{E}_d^{ext} = \hat{E}_{MS}^{ext} + \hat{E}_{MD}^{ext} \tag{22}$$

The external energy of the anchor points can be rewritten as

$$\hat{E}_{MS}^{ext} = \sum_{I=1}^{n^{MS}} \left[1 - \alpha(\xi(\mathbf{R}_I^{MS}))\right] \mathbf{f}_I^{AP\,ext} \cdot \mathbf{w}_I, \tag{23}$$

while the term $\hat{E}_{MD}^{ext}$ does not change during a continuum equilibration step. Hence, the total energy of the coupled static system can be formulated as follows:

$$\hat{E}^{tot} = \hat{E}_c^{int} + \hat{E}_d^{int} - \hat{E}_c^{ext} - \hat{E}_d^{ext}. \tag{24}$$

It has to be remarked that the coupled systems discussed in this contribution do not consider external forces acting on anchor points nor on MD particles.

Coupling constraint

In addition to the blended energies, a coupling constraint is required to ensure matching of continuum and anchor point displacements in the bridging domain. Only the anchor points are considered when formulating the coupling constraint, since the remaining MD particles are not visible for the continuum. The match of displacements is realized by evaluating the difference between the continuous displacement field **u** and a fictitious displacement field $\mathbf{w}^*$ which has to be computed similarly to [14], since there are only discrete displacements available:

$$\mathbf{w}^* = \Pi \mathbf{w}. \tag{25}$$

In (25), the displacements are defined as

$$\mathbf{w} = \left\{\mathbf{w}_1, \cdots \mathbf{w}_I, \cdots \mathbf{w}_{n^{MS}}\right\}^T = \mathbf{r}^{MS} - \mathbf{R}^{MS} \tag{26}$$

with $\mathbf{R}^{MS}$ and $\mathbf{r}^{MS}$ given in terms of position vectors before ($\mathbf{R}_I^{MS}$) and after ($\mathbf{r}_I^{MS}$) deformation:

$$\begin{aligned} \mathbf{R}^{MS} &= \left\{\mathbf{R}_1^{MS}, \cdots \mathbf{R}_I^{MS}, \cdots \mathbf{R}_{n^{MS}}^{MS}\right\}^T \; and \\ \mathbf{r}^{MS} &= \left\{\mathbf{r}_1^{MS}, \cdots \mathbf{r}_I^{MS}, \cdots \mathbf{r}_{n^{MS}}^{MS}\right\}^T. \end{aligned} \tag{27}$$

The moving least-square approximation Π is discussed in [29]:

$$\mathbf{w}^*(\mathbf{X}) = \mathbf{\Phi}(\mathbf{X}) \cdot \mathbf{w} = \sum_{I=1}^{n^{MS}} \Phi_I(\mathbf{X}) \left[\mathbf{r}_I^{MS} - \mathbf{R}_I^{MS}\right], \tag{28}$$

employing the shape function

$$\mathbf{\Phi}(\mathbf{X}) = \left[\Phi_1(\mathbf{X}) \ldots \Phi_{n^{MS}}(\mathbf{X})\right] = \mathbf{p}^T(\mathbf{X}) \cdot \mathbf{A}^{-1}(\mathbf{X}) \cdot \mathbf{P}^T \cdot \mathbf{W}(\mathbf{X}) \tag{29}$$

with the linear basis

$$\mathbf{p}^T = [1, X, Y, Z], \quad \mathbf{X} = [X, Y, Z]^T, \tag{30}$$

$$\mathbf{P} = \begin{bmatrix} \mathbf{p}^T(\mathbf{R}_1^{MS}) \\ \vdots \\ \mathbf{p}^T(\mathbf{R}_{n^{MS}}^{MS}) \end{bmatrix}, \tag{31}$$

the moment matrix

$$\mathbf{A}(\mathbf{X}) = \mathbf{P}^T \cdot \mathbf{W}(\mathbf{X}) \cdot \mathbf{P}, \tag{32}$$

and the weight function matrix

$$\mathbf{W}(\mathbf{X}) = \begin{bmatrix} w_1(\mathbf{X}) & 0 & \cdots & 0 \\ 0 & w_2(\mathbf{X}) & \cdots & 0 \\ \vdots & \vdots & \ddots & \vdots \\ 0 & 0 & \cdots & w_{n^{MS}}(\mathbf{X}) \end{bmatrix}. \tag{33}$$

The weight function used here is a quartic spline

$$w_I(\mathbf{X}) = \begin{cases} 1 - 6r_I^2 + 8r_I^3 - 3r_I^4 & for\ r_I \le 1 \\ 0 & for\ r_I > 1 \end{cases} \tag{34}$$

with

$$r_I = \frac{1}{\rho} \| \mathbf{X} - \mathbf{R}_I^{MS} \|, \tag{35}$$

where ρ is the radius of support.

Using $\mathbf{w}^*$, the following coupling constraint is defined to enforce matching displacements:

$$\| \mathbf{u} \quad - \mathbf{w}^* \|^2 = \beta_1 \int_{\Omega^b} \left[\mathbf{u} - \mathbf{w}^*\right] \cdot \left[\mathbf{u} - \mathbf{w}^*\right] dV + \beta_2 \int_{\Omega^b} \frac{\partial \left[\mathbf{u} - \mathbf{w}^*\right]}{\partial \mathbf{X}} : \frac{\partial \left[\mathbf{u} - \mathbf{w}^*\right]}{\partial \mathbf{X}} dV \overset{!}{=} 0. \tag{36}$$

(36) refers to the L^2 norm for $(\beta_1, \beta_2) = (1,0)$ and to the H^1 norm for $(\beta_1, \beta_2) = (1,1)$. To minimize the total energy (24) of the coupled system and to enforce the coupling constraint, the Lagrange multiplier method is applied. Using Lagrange multipliers $\boldsymbol{\lambda}$, the coupling constraint can be rewritten as

$$b(\lambda, \mathbf{u}, \mathbf{r}^{MS}) = \beta_1 \int_{\Omega^b} \lambda \cdot \left[\mathbf{u} - \mathbf{w}^*\right] dV + \beta_2 \int_{\Omega^b} \frac{\partial \lambda}{\partial \mathbf{X}} : \frac{\partial \left[\mathbf{u} - \mathbf{w}^*\right]}{\partial \mathbf{X}} dV. \tag{37}$$

Thus, the optimization problem can be solved by computing the saddle point of

$$L(\lambda, \mathbf{u}, \mathbf{r}^{MS}) = \hat{E}_{tot} + b(\lambda, \mathbf{u}, \mathbf{r}^{MS}) \tag{38}$$

with L being a function of the displacement field $\mathbf{u}$, the Lagrange multiplier field $\boldsymbol{\lambda}$, and the anchor point positions $\mathbf{r}^{MS}$.

4.2.3.3 Discretization

In this section, the discretization of the displacement field $\mathbf{u}$ as well as the Lagrange multiplier field $\boldsymbol{\lambda}$ is discussed in order to solve the optimization problem (38). In both cases, linear basis functions are used:

$$\mathbf{u}(\mathbf{X}) \approx \sum_{i=1}^{n_c} N_i^c(\mathbf{X})\, \mathbf{u}_i^h = \mathbf{N}^c(\mathbf{X}) \cdot \mathbf{u}^h, \tag{39}$$

$$\boldsymbol{\lambda}(\mathbf{X}) \approx \sum_{j=1}^{n_\lambda} N_j^\lambda(\mathbf{X})\, \boldsymbol{\lambda}_j^h = \mathbf{N}^\lambda(\mathbf{X}) \cdot \boldsymbol{\lambda}^h. \tag{40}$$

$\mathbf{u}_i^h$ and $\boldsymbol{\lambda}_j^h$ denote the nodal values, N_i^c and N_j^λ are the respective basis functions, while n_c and n_λ describe the number of nodes in the discretized continuum and the Lagrange multiplier space. The nodal values are assembled into the vectors $\mathbf{u}^h$ and λ^h. Consequently, L becomes a function of the discretized displacements and Lagrange multipliers:

$$L(\lambda, \mathbf{u}, \mathbf{r}^{MS}) \approx L(\lambda^h, \mathbf{u}^h, \mathbf{r}^{MS}). \tag{41}$$

The set of variables can be summarized in a vector $\mathbf{d} = \left[\boldsymbol{\lambda}^h, \mathbf{u}^h, \mathbf{r}^{MS}\right]^T$ which allows to define the necessary condition for a saddle point of (38):

$$\delta_{\mathbf{d}} L(\mathbf{d}) = \delta_{\mathbf{d}} \hat{E}_{tot}(\mathbf{u}^h, \mathbf{r}^{MS}) + \delta_{\mathbf{d}} b(\mathbf{d}) = 0. \tag{42}$$

The resulting set of equations can be structured into three parts:

FE domain

The relations in the FE domain are obtained from the variation of L with respect to the nodal displacements $\mathbf{u}^h$:

$$\delta_{\mathbf{u}^h} L = 0 \rightarrow \quad \left\{ \begin{array}{lcl} \hat{\mathbf{f}}_c^{int}(\mathbf{u}^h) & = & \hat{\mathbf{f}}_c^{ext} \\ \mathbf{f}_b^{int}(\mathbf{u}^h) + \mathbf{f}^{cpl}(\boldsymbol{\lambda}^h) & = & \mathbf{f}_b^{ext} \end{array} \right\} \tag{43}$$

The internal forces in the pure FE domain and in the bridging domain are given by $\hat{\mathbf{f}}_c^{int}$ and $\mathbf{f}_b^{int}$, while $\mathbf{f}^{cpl}$ denotes the vector of coupling forces due to the coupling constraint. The external force vectors in the respective domains are represented by $\hat{\mathbf{f}}_c^{ext}$ and $\mathbf{f}_b^{ext}$. In case of a linear stress-strain relation in the continuum, the internal force vectors can be written as

$$\begin{bmatrix} \hat{\mathbf{f}}_c^{int} \\ \mathbf{f}_b^{int} \end{bmatrix} = \mathbf{K}^c \cdot \begin{bmatrix} \hat{\mathbf{u}}^c \\ \mathbf{u}^b \end{bmatrix} = \mathbf{K}^c \cdot \mathbf{u}^h \quad \textit{and} \tag{44}$$

$$\mathbf{f}^{cpl} = \mathbf{G}_{c\lambda} \cdot \boldsymbol{\lambda}^h. \tag{45}$$

Here, a $(n_c^{dof} \times n_c^{dof})$ stiffness matrix $\mathbf{K}^c$ in the continuum and a $(n_{cb}^{dof} \times n_\lambda^{dof})$ coupling matrix $\mathbf{G}_{c\lambda}$ in the bridging domain is used. n_c^{dof} is the number of FE degrees of freedom in the continuum Ω^c, n_{cb}^{dof} the number of FE degrees of freedom in the bridging domain Ω^b, and n_λ^{dof} the number of degrees of freedom of the Lagrange multipliers. Furthermore, the vector of nodal displacements $\mathbf{u}^h$ is separated into a vector of nodal displacements in the pure FE domain $\hat{\mathbf{u}}^c$ and a vector of displacements in the bridging domain $\mathbf{u}^b$.

Particle domain

The system of equations for the particle domain follows as:

$$\delta_{\mathbf{w}} L = 0 \rightarrow \left\{ -\mathbf{f}^{MS}(\mathbf{w}) + \mathbf{f}^{AP\,cpl}(\boldsymbol{\lambda}^h) - \mathbf{f}^{AP} = \mathbf{f}^{AP\,ext} \right\} \tag{46}$$

In (46), the vectors $\mathbf{f}^{MS}$ and $\mathbf{f}^{AP}$ subsume all anchor point forces as introduced in (??), multiplied by $[1-\alpha]$, while $\mathbf{f}^{AP\,cpl}$ is the vector of all forces that are exerted on anchor points due to the coupling constraint. For sake of completeness, the vector of external forces $\mathbf{f}^{AP\,ext}$ acting on anchor points is given as well:

$$\begin{aligned} I-th\,component\,of\ \mathbf{f}^{AP}(force\,vector\,of\ anchor\ point\ I) &: \left[1-\alpha\left(\xi\left(\mathbf{R}_I^{MS}\right)\right)\right]\mathbf{f}_I^{AP}, \\ I-th\,component\,of\ \mathbf{f}^{AP\,ext}(force\,vector\,of\ anchor\ point\ I) &: \left[1-\alpha\left(\xi\left(\mathbf{R}_I^{MS}\right)\right)\right]\mathbf{f}_I^{AP\,ext}. \end{aligned} \tag{47}$$

Since only harmonic interaction potentials between anchor points and superatoms are considered in the present formalism, a $(n_d^{dof} \times n_d^{dof})$ stiffness matrix $\mathbf{K}^d$ can be introduced with $n_d^{dof} = 3n^{MS}$. Based on (4) it reads

$$\mathbf{f}^{MS}(\mathbf{w}) = -\mathbf{K}^d \cdot \mathbf{w} \quad with$$

$$\mathbf{K}^d = \begin{bmatrix} \mathbf{K}_{\alpha 1}^{AP} & 0 & 0 \\ 0 & \ddots & 0 \\ 0 & 0 & \mathbf{K}_{\alpha\, n^{MS}}^{AP} \end{bmatrix}; \quad \mathbf{K}_{\alpha I}^{AP} = \left[1-\alpha\left(\xi\left(\mathbf{R}_I^{MS}\right)\right)\right]\mathbf{K}_I^{AP}. \tag{48}$$

Furthermore, a $(n_d^{dof} \times n_\lambda^{dof})$ coupling matrix $\mathbf{G}_{d\lambda}$ is used as follows:

$$\mathbf{f}^{AP\,cpl} = \mathbf{G}_{d\lambda} \cdot \boldsymbol{\lambda}^h \tag{49}$$

Lagrange multipliers

The variation of L with respect to the Lagrange multipliers leads to:

$$\begin{aligned} \delta_{\boldsymbol{\lambda}^h} L = 0 \rightarrow \left\{ \mathbf{G}_{\lambda c} \cdot \mathbf{u}^b + \mathbf{G}_{\lambda d} \cdot \mathbf{w} = \mathbf{0} \right\} \quad with \\ \mathbf{G}_{\lambda c} = \mathbf{G}_{c\lambda}^T \quad and \quad \mathbf{G}_{\lambda d} = \mathbf{G}_{d\lambda}^T \end{aligned} \tag{50}$$

Thus, the complete system of equations can be formulated as follows:

$$\delta_{\mathbf{u}^h, \mathbf{w}, \boldsymbol{\lambda}^h} L = 0 \rightarrow \quad \left\{ \begin{array}{rcl} \hat{\mathbf{f}}_c^{int}(\mathbf{u}^h) & = & \hat{\mathbf{f}}_c^{ext} \\ 0cm\ \mathbf{f}_b^{int}(\mathbf{u}^h) + \mathbf{G}_{c\lambda} \cdot \boldsymbol{\lambda}^h & = & \mathbf{f}_b^{ext} \\ \mathbf{K}^d \cdot \mathbf{w} + \mathbf{G}_{d\lambda} \cdot \boldsymbol{\lambda}^h & = & \mathbf{f}^{AP\,ext} + \mathbf{f}^{AP} \\ \mathbf{G}_{\lambda c} \cdot \mathbf{u}^b + \mathbf{G}_{\lambda d} \cdot \mathbf{w} & = & \mathbf{0} \end{array} \right\} \tag{51}$$

In case of a linear elastic continuum and in absence of external forces acting on anchor points, the system of equations becomes linear and can be written as:

$$\begin{bmatrix} \mathbf{K}^c & \mathbf{0} & \begin{bmatrix} \mathbf{0} \\ \mathbf{G}_{c\lambda} \end{bmatrix} \\ \mathbf{0} & \mathbf{K}^d & \mathbf{G}_{d\lambda} \\ \mathbf{G}_{\lambda c} & \mathbf{G}_{\lambda d} & \mathbf{0} \end{bmatrix} \cdot \begin{bmatrix} \mathbf{u}^h \\ \mathbf{w} \\ \boldsymbol{\lambda}^h \end{bmatrix} = \begin{bmatrix} \begin{bmatrix} \hat{\mathbf{f}}_c^{ext} \\ \mathbf{f}_b^{ext} \end{bmatrix} \\ \mathbf{f}^{AP} \\ \mathbf{0} \end{bmatrix} \tag{52}$$

Concluding this section, (52) describes the coupling between the finite element domain and the anchor points, treating the MD region as a domain that interacts with its surrounding only via anchor points. Important quantities are, among others, the stiffness of the finite element domain and of the anchor points, represented by the stiffness matrices $\mathbf{K}^c$ and $\mathbf{K}^d$, the coupling forces $\mathbf{f}^{cpl}$ and $\mathbf{f}^{APcpl}$, expressed in terms of the Lagrange multipliers $\boldsymbol{\lambda}^h$ as well as the coupling matrices $\mathbf{G}_{c\lambda}$ and $\mathbf{G}_{d\lambda}$, the forces exterted on anchor points by the MD domain $\mathbf{f}^{AP}$, and, of course, the nodal displacements $\mathbf{u}^h$ and the displacements of anchor points $\mathbf{w}^h$. In the following section, we will focus on the implementation of the relations developed so far and discuss some important technical aspects.

4.3 Coupling Scheme

4.3.1 Staggered coupling of FE and MD

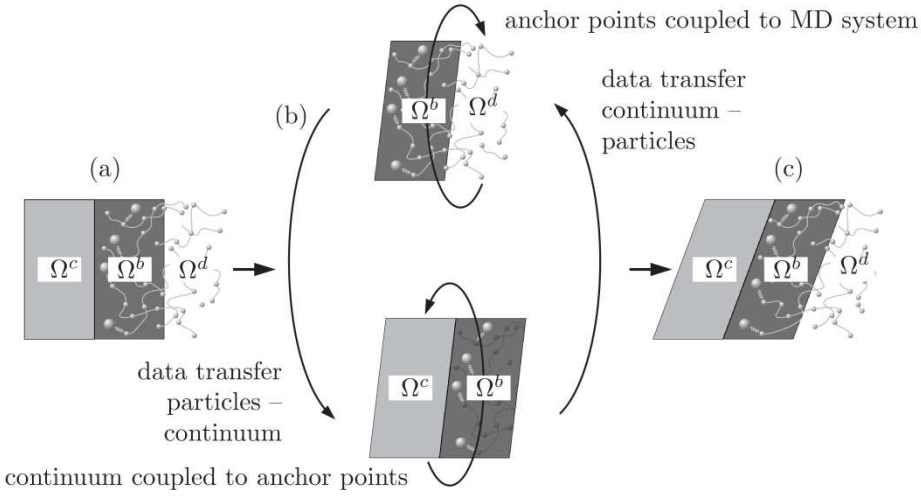

Figure 5: Concept of the staggered coupling scheme: initial configuration (a), coupling procedure (b): equilibration of continuum coupled to anchor points (bottom, merely the anchor points are "visible" to the continuum, the MD particles are fixed), data transfer (anchor point displacements) to the particle system, equilibration of the particle system (top, fixed anchor points represent the continuum enclosing the particles), data transfer (forces exerted by the particles on the anchor points) back to the continuum, deformed and equilibrated system (c)

Based on the definitions and equations introduced in the previous sections, the staggered coupling procedure is described in the following. As stated before, an iterative solution scheme is mandatory to solve the basic equations for the coupled system. On the one hand, the positions of anchor points change due to the deformation of the continuum while the superatoms of the MD domain remain fixed (coupling between continuum and anchor points). On the other hand, the MD particles move within a frame of fixed anchor points (anchor points tethered to MD system), cf. Figure 5, until the reaction forces on the anchor points are converged within their statistical-mechanical variation. This procedure has to be continued until the deformed coupled system is in equilibrium.

This contribution focusses on MD systems at small deformations, i.e. showing a nearly linear stress-strain relation. Thus, it is possible to consider a linear elastic FE system that can be computed by solving the system (52) of linear equations. The staggered algorithm is set up as follows:

1. **initial MD-FE iteration step:** $n = 1$

   a) **initial MD run:** the MD system is set up, the anchor points are defined, the system is equilibrated, the reaction forces are sampled;

   output data:

   - $\mathbf{r}_{(1)}^{MD}$: current positions of superatoms in the first MD-FE iteration step $n = 1$
   - $\mathbf{R}_{(1)}^{MS}$: initial anchor point positions in the first MD-FE iteration step $n = 1$ (chosen according to [22])
   - $\left\langle \hat{\mathbf{f}}^{AP} \right\rangle_{\tau(1)}$: time average of forces exerted on anchor points by superatoms, i.e. by the MD domain ("reaction forces")

   b) **initial FE equilibration run:** the FE system is set up, the bridging domain is defined such that it contains all anchor points; the FE system is deformed due to Dirichlet and Neumann boundary conditions; thus, anchor points are moved and form a new boundary for the MD system;

   input data:

   - $\mathbf{X}^{FE}$, $\mathbf{R}_{(1)}^{MS}$: initial positions of FE nodes and anchor points
   - $\mathbf{f}_{(1)}^{AP} = \left\langle \hat{\mathbf{f}}^{AP} \right\rangle_{\mathsf{T}(1)}$: the time average of forces exerted on anchor points is interpreted as a static section force vector between anchor points and their associated superatoms

   output data (computed by solving (51) or (52)):

   - $\mathbf{x}_{(1)}^{FE}$: current positions of FE nodes after the first FE-MD iteration step
   - $\mathbf{r}_{(1)}^{MS}$: current anchor point positions after the first FE-MD iteration step

2. **i-th MD-FE iteration step:** $n = i$
   a) **i-th MD run:** MD equilibration according to updated anchor point positions followed by sampling of the reaction forces

   input data:
   - $\mathbf{R}_{(i)}^{MD} = \mathbf{r}_{(i-1)}^{MD}$: initial positions of superatoms in the i-th MD-FE iteration step
   - $\mathbf{R}_{(i)}^{MS} = \mathbf{r}_{(i-1)}^{MS}$: initial anchor point positions in the i-th MD-FE iteration step

   output data:
   - $\mathbf{r}_{(i)}^{MD}$: current positions of superatoms in the i-th MD-FE iteration step
   - $\left\langle \hat{\mathbf{f}}^{AP} \right\rangle_{\tau(i)}$

   b) **i-th FE equilibration run:** due to updated anchor point forces, the FE system is equilibrated;
   input data:
   - $\mathbf{X}^{FE}$: initial positions of FE nodes (independent of MD-FE iteration step)
   - $\mathbf{R}_{(i)}^{MS}$: initial anchor point positions in the i-th MD-FE iteration step
   - $\mathbf{f}_{(i)}^{AP} \left\langle \hat{\mathbf{f}}^{AP} \right\rangle_{\tau(i)}$

   output data (computed by solving (51) or (52)):
   - $\mathbf{x}_{(i)}^{FE}$: current positions of FE nodes after the i-th FE-MD iteration step
   - $\mathbf{r}_{(i)}^{MS}$: current anchor point positions after the i-th FE-MD iteration step

3. **continue** with subsequent MD-FE iteration steps until a criterion for convergence is met;

This procedure is visualized in Figure 6: the i-th MD-FE iteration step is defined by an MD run that provides updated positions of superatoms $\mathbf{r}_{(i)}^{MD}$ and the time average $\left\langle \hat{\mathbf{f}}^{AP} \right\rangle_{\tau(i)}$ of forces exerted on the anchor points by the superatoms. Both quantities are computed as a function of the initial positions of superatoms $\mathbf{R}_{(i)}^{MD}$ and anchor points $\mathbf{R}_{(i)}^{MS}$. During this MD run, the FE domain is not "visible" to the MD domain, since the influence of the FE domain is transferred into the MD region only by the anchor points. The time average $\left\langle \hat{\mathbf{f}}^{AP} \right\rangle_{\tau(i)}$ is used as input for the subsequent FE equilibration such that $\mathbf{f}_{(i)}^{AP} = \left\langle \hat{\mathbf{f}}^{AP} \right\rangle_{\tau(i)}$. In this step, the current positions of FE nodes $\mathbf{x}_{(i)}^{FE}$ as well as the positions of anchor points $\mathbf{r}_{(i)}^{MS}$ are determined as a function of the initial nodal positions $\mathbf{X}^{FE}$, the initial anchor point positions $\mathbf{R}_{(i)}^{MS}$ of the current FE-MD iteration step i, and $\mathbf{f}_{(i)}^{AP}$. Reciprocally to the MD run, now the particle domain is not "visible". Only the anchor points represent the MD system during the FE computation. In the next MD-FE iteration step, the updated anchor point positions serve as input for

the MD computation: $\mathbf{R}_{(i)}^{MS} = \mathbf{r}_{(i-1)}^{MS}$. This procedure is carried out until a criterion for convergence is met, which will be discussed later.

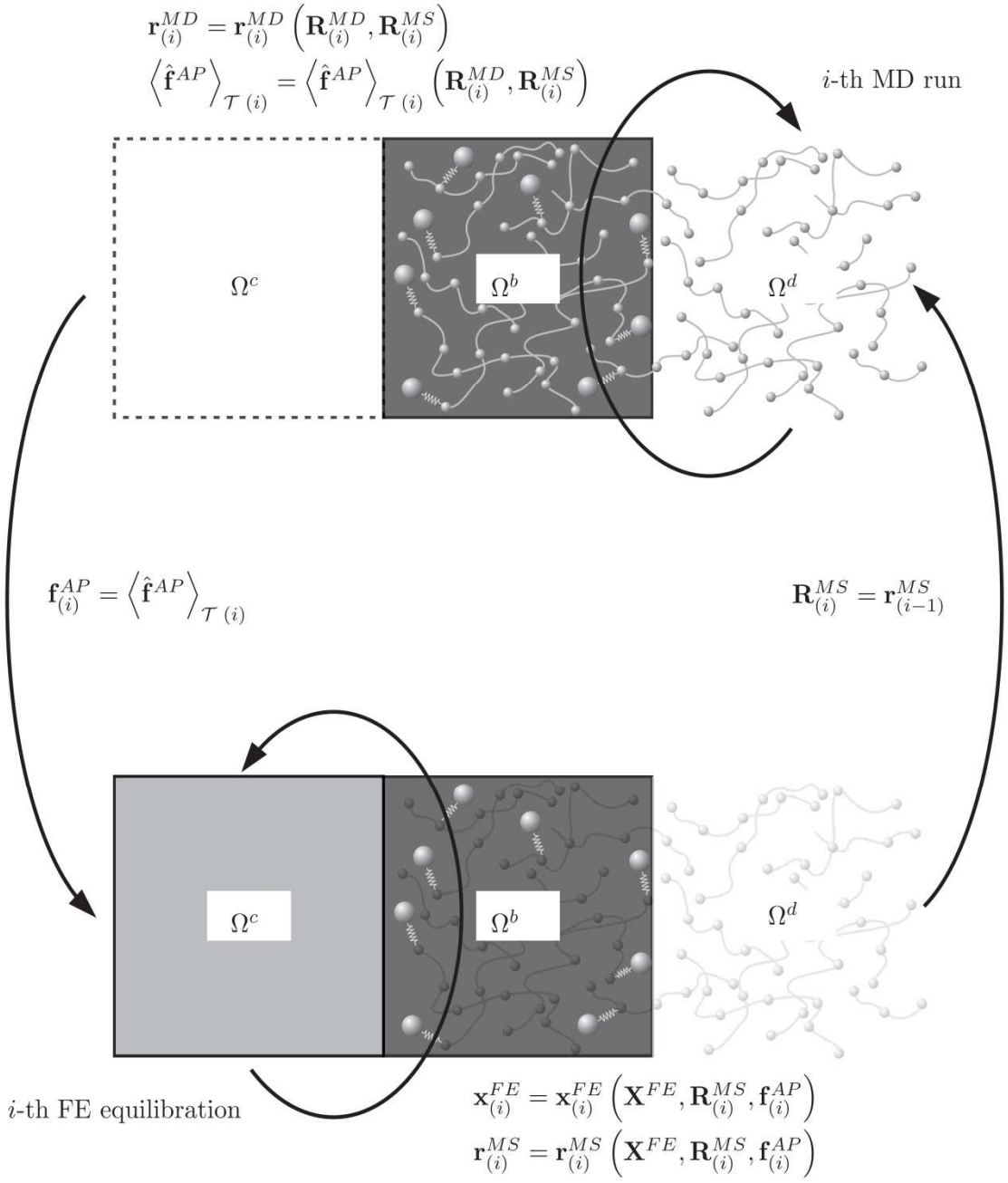

Figure 6: i-th MD-FE iteration step combines the i-th MD run (top) and the i-th FE equilibration (bottom): during the MD run an update of MD particle positions $\mathbf{r}_{(i)}^{MD}$ and computation of the time average of forces acting on anchor points $\left\langle \hat{\mathbf{f}}^{AP} \right\rangle_{\tau(i)}$ is performed, the FE equilibration run delivers updated positions of FE nodes and anchor points; data is transferred from MD to FE and vice versa

Remark on the displacements of anchor points

In order to apply (52) to a linear elastic FE system at an arbitrary MD-FE iteration step i, some adaptions are required: the third set of equations of (52), which essentially represents the geometric coupling constraint, is formulated with nodal displacements $\mathbf{u}^h = \mathbf{x}^{FE} - \mathbf{X}^{FE}$, representing the difference between current positions and the intial FE configuration.

Thus, at the i-th MD-FE iteration it reads

$$\mathbf{u}^h_{(i)} = \mathbf{x}^{FE}_{(i)} - \mathbf{X}^{FE}. \tag{53}$$

To fulfill the coupling constraint properly, the total displacement of anchor points with respect to their original positions $\mathbf{R}^{MS}_{(1)}$ at the first iteration step has to be considered:

$$\mathbf{w}^{tot}_{(i)} = \mathbf{r}^{MS}_{(i)} - \mathbf{R}^{MS}_{(1)}. \tag{54}$$

However, the energy of the particle region that is ”visible“ in the FE domain is restricted to the energy of bonds between anchor points and their associated superatoms, i.e. at the i-th MD-FE iteration step it reads

$$E^{int}_{MS\,I\,(i)} = \frac{1}{2} k_I \,|\, \mathbf{r}^{MS}_{I\,(i)} - \mathbf{R}^{MD}_{I\,(i)} \,|^2 \neq \frac{1}{2} k_I \,|\, \mathbf{w}^{tot}_{I\,(i)} \,|^2 . \tag{55}$$

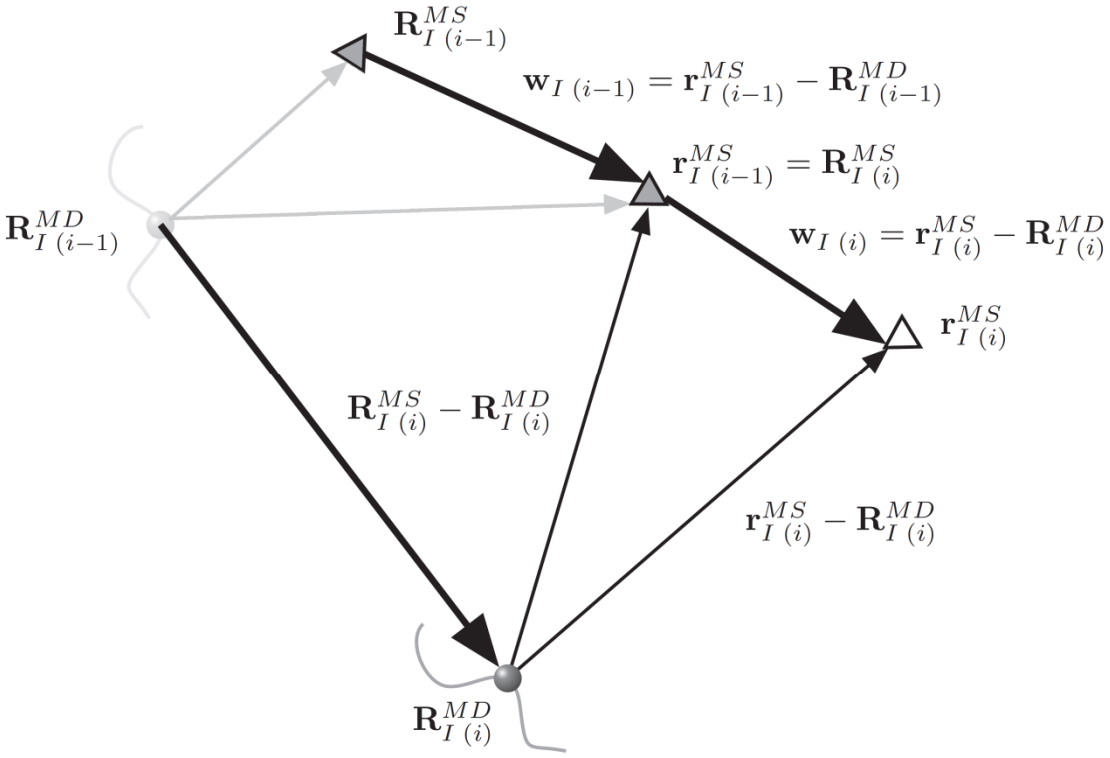

Figure 7: Positions of anchor point I and its associated superatom in the $(i-1)$-th (top) and i-th (bottom) MD-FE iteration step

Taking the derivative of (55) with respect to the position of the I-th anchor point in the i-th iteration step, it follows:

$$\begin{aligned}
\mathbf{f}_{I(i)}^{tot} &= -\frac{\partial E_{MS\,I(i)}^{int}}{\partial \mathbf{r}_{I(i)}^{MS}} \\
&= -k_I\left[\mathbf{r}_{I(i)}^{MS} - \mathbf{R}_{I(i)}^{MD}\right] = -k_I\left[\mathbf{r}_{I(i)}^{MS} - \mathbf{R}_{I(i)}^{MS}\right] - k_I\left[\mathbf{R}_{I(i)}^{MS} - \mathbf{R}_{I(i)}^{MD}\right] \\
&= -k_I\ \mathbf{w}_{I(i)} + \mathbf{f}_{I(i)}^{AP} = -k_I\ \mathbf{w}_{I(i)} - k_I\sum_{j=1}^{i-1}\mathbf{w}_{I(j)} + k_I\sum_{j=1}^{i-1}\mathbf{w}_{I(j)} + \mathbf{f}_{I(i)}^{AP} \\
&= -k_I\sum_{j=1}^{i}\mathbf{w}_{I(j)} + k_I\left[\mathbf{r}_{I(i-1)}^{MS} - \mathbf{R}_{I(1)}^{MS}\right] + \mathbf{f}_{I(i)}^{AP} \\
&= -k_I\ \mathbf{w}_{I(i)}^{tot} + k_I\left[\mathbf{R}_{I(i)}^{MS} - \mathbf{R}_{I(1)}^{MS}\right] + \mathbf{f}_{I(i)}^{AP}
\end{aligned} \tag{56}$$

With weighting factor $\alpha(\xi)$ this can be rewritten as

$$\mathbf{f}_{(i)}^{tot} = -\frac{\partial E_{MS\,(i)}^{int}}{\partial \mathbf{r}_{(i)}^{MS}} = -\mathbf{K}^d \cdot \mathbf{w}_{(i)}^{tot} + \mathbf{K}^d \cdot \left[\mathbf{R}_{(i)}^{MS} - \mathbf{R}_{(1)}^{MS}\right] + \mathbf{f}_{(i)}^{AP} \tag{57}$$

with

$$\begin{aligned}
I-th\ component\ of\ \mathbf{f}_{(i)}^{AP} \quad &: \quad \left[1-\alpha\left(\xi\left(\mathbf{R}_I^{MS}\right)\right)\right]\mathbf{f}_{I(i)}^{AP}, \\
I-th\ component\ of\ \mathbf{f}_{(i)}^{tot} \quad &: \quad \left[1-\alpha\left(\xi\left(\mathbf{R}_I^{MS}\right)\right)\right]\mathbf{f}_{I(i)}^{tot}.
\end{aligned} \tag{58}$$

Thus, (52) can be reformulated for the i-th MD-FE iteration step:

$$\begin{bmatrix} \mathbf{K}^c & \mathbf{0} & \begin{bmatrix}\mathbf{0}\\ \mathbf{G}_{c\lambda}\end{bmatrix} \\ \mathbf{0} & \mathbf{K}^d & \mathbf{G}_{d\lambda} \\ \mathbf{G}_{\lambda c} & \mathbf{G}_{\lambda d} & \mathbf{0} \end{bmatrix} \cdot \begin{bmatrix} \mathbf{u}_{(i)}^h \\ \mathbf{w}_{(i)}^{tot} \\ \boldsymbol{\lambda}_{(i)}^h \end{bmatrix} = \begin{bmatrix} \begin{bmatrix}\hat{\mathbf{f}}_c^{ext}\\ \mathbf{f}_b^{ext}\end{bmatrix} \\ \mathbf{f}_{(i)}^{AP} + \mathbf{K}^d \cdot \left[\mathbf{R}_{(i)}^{MS} - \mathbf{R}_{(1)}^{MS}\right] \\ \mathbf{0} \end{bmatrix} \tag{59}$$

4.3.2 Initialization of a coupled MD–FE simulation

In order to carry out a coupled MD-FE computation, some technical aspects have to be discussed. Before the coupling procedure can be applied as described in the previous section, the system has to be set up: on the one hand, the continuum has to be defined and a FE mesh must be created. On the other hand, it is necessary to prepare the particle domain in a way that it can replace a part of the FE domain. Furthermore, the match between the different regions has to be ensured by defining the bridging domain. The systems investigated in the following consist of a hollow cube discretized by finite elements and a cubic particle domain that is fully embedded into the FE domain, cf. Figure 8.

1. The cubic particle domain is set up by defining the box size of the MD system, and, among others, the kind of the particles, their interactions, temperature, pressure, etc. This system is equilibrated using standard periodic boundary conditions without defining any anchor points.

This first equilibration procedure generates the initial configuration of the particle domain, which is cooled down below the glass transition temperature. Furthermore, the elastic constants (Young's modulus and Poisson's ratio) of the polymer can be obtained from uni-axial tension tests (parameter identification).

2. The particles (or superatoms in case of coarse grained simulations as carried out here) tethered to anchor points are selected using a probability function in the boundary domain. Without going into detail here, this probability function can be chosen as constant, linear, or as an exponential decay function. After that, the corresponding anchor points are created. The particle domain is now surrounded by stochastic boundary conditions and ready to be coupled to the FE domain.
3. Since the initial anchor point positions are defined randomly, an equilibrium distribution cannot be expected. Thus, a coupled simulation has to be performed without applying any deformation to the FE domain which is chosen very weak (low Young's modulus). Hence, an equilibrium distribution of anchor points is obtained. The algorithm is the same as used in the actual MD-FE coupling procedure.
4. The coupled MD-FE simulation is carried out. For the FE domain, elastic constants as obtained from the parameter identification of the pure MD system (step 1) are used.

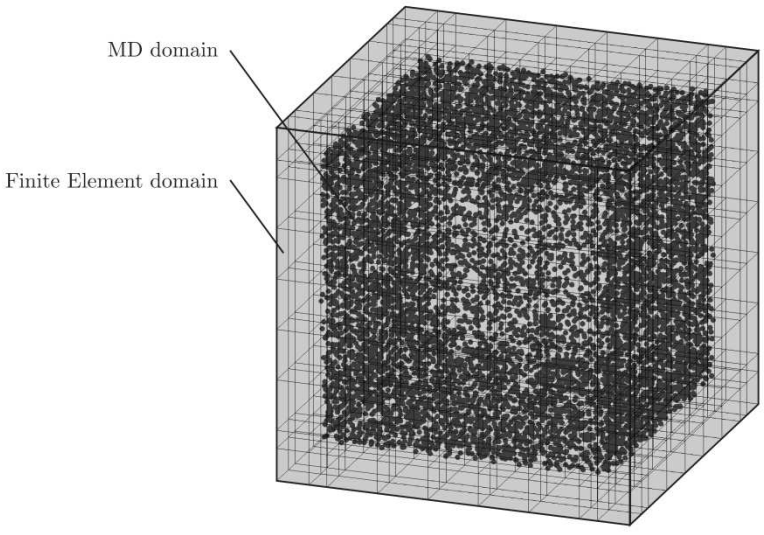

Figure 8: Considered simulation box: hollow FE cube filled with MD system

4.4 Numerical examples

In this section, coupled MD–FE simulations are benchmarked against pure FE simulations and some criteria suitable to demonstrate the capability of the new hybrid method are introduced. When considering homogeneous materials at small strains, similar results should be obtained in case of coupled simulations and pure FE computations.

4.4.1 System configuration

Atactic polystyrene (PS) in CG representation (1 CG bead per chemical repeat unit) [19] is employed to demonstrate the coupling method. The CG potentials, derived by iterative Boltzmann inversion at 590 K and 101.3 kPa, have been optimized by minimizing the difference between radial distribution functions of a chosen atomistic reference system and the CG profile. The PS sample is represented by 300 polymer chains, each consisting of 200 CG beads. The initial configurations are generated as self-avoiding random walks (SARW) at low density (0.7 kgm^{-3}) in order to avoid overlap of the CG beads. Under conventional PBCs, the equilibration of the polymer required up to 20 ns, using a time step $\Delta t = 5$ fs. In order to prepare the particle system for the coupling procedure, the temperature is reduced to 100 K, which is well below the glass transition temperature of PS in CG model (T_g = 170 K, [30]). The constant cooling rate is 10 Kns^{-1}, the equilibrated box size is 20.8 nm in each direction.

After that, the boundary conditions are switched from periodic to nonperiodic, using the final PBC configuration as the initial state for the subsequent SBC simulation. Polymer chains, which are not located completely in the final PBC box, are divided into smaller fragments. The presence of shorter polymer chains may lead to local differences in the material properties which will be discussed later. The thickness of the effective boundary region is chosen as 1.5 nm, which equals the cutoff radius of the particle simulation, whereas the size of the DPD region is 0.5 nm. Using the same overall box size as in case of PBC, the edge length of the central MD region consequently follows as 16.8 nm.

In the next step, the anchor points are defined. In order to prevent a loss of MD particles from the simulation box, an exponential decay of the anchor point density is chosen: the density is high at the interface between the bridging domain and the pure FE domain and decreases to zero at the interface with the DPD region.

The final simulation box contains 300 polymer chains, each consisting of 200 superatoms, which in total amounts to 60,000 superatoms, with approximately 29,000 of these being located in the boundary region. Furthermore, 9004 anchor points are defined and coupled to the MD particles using a

force constant $k_I = 1400\, kJmol^{-1}nm^{-2} = 2.32\, Nm^{-1}$. This value is of the same order of magnitude as employed between bonded CG beads in the MD region, a choice which prevents larger system perturbations and which allows to keep the timestep of 5 fs. Furthermore, the DPD equations of motion are solved with a friction coefficient of 10 pNpsnm^{-1}. With this setup an efficient temperature control is possible (T = 99.85 ± 0.4 K). Before coupling the particle system to the FE domain an additional equilibration of 5 ns is performed.

The material parameters to be used in the FE domain are identified from a pure MD simulation under PBCs. Recently we have studied the mechanical behaviour of PS in CG resolution under uniaxial deformation [30]. Figure 9 shows the stress-strain curve of PS at 100 K obtained from a numerical uniaxial tension test, employing a deformation rate of 10 nm/ns. Up to 3% strain, the stress–strain relation is approximately linear, after that it becomes clearly nonlinear and around 7% strain, the yield point can be observed. A Young's modulus of $E = 827\ MPa$ is computed from the slope of the stress–strain curve in the almost linear part. Furthermore, the Poisson's ratio is slightly higher than 0.3, which is close to the value identified from atomistic simulations [31]. It has to be mentioned that, due to the CG description, the Young's modulus is smaller than in atomistic simulations or experiments. The reasons for that, together with an appropriate scaling procedure, are discussed in detail in [30].

With the linear elastic material parameters at hand, the FE domain is set up according to the size of the particle domain. In this contribution, a hollow cube is chosen with an edge length of 30 nm, whereas the bridging domain Ω^b coincides with the effective boundary region of the particle system. The system is deformed symmetrically by prescribing displacements in y-direction at the upper and lower xz-surfaces, cf. Figure 10.

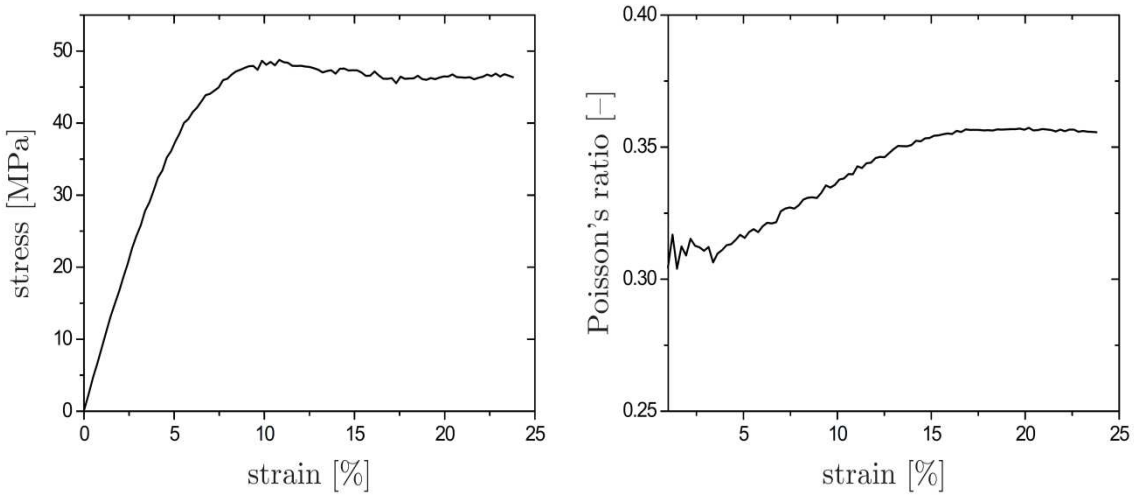

Figure 9: Parameter identification from the pure particle system: stress-strain curve (left) and Poisson's ratio as a function of strain (right). Both diagrams have been obtained from a uniaxial

tension test based on a coarse grained simulation of polystyrene at 100 K, $T_g = 170$ K, the deformation rate is 10 nm/ns, the stress is computed with respect to the deformed geometry, from [30].

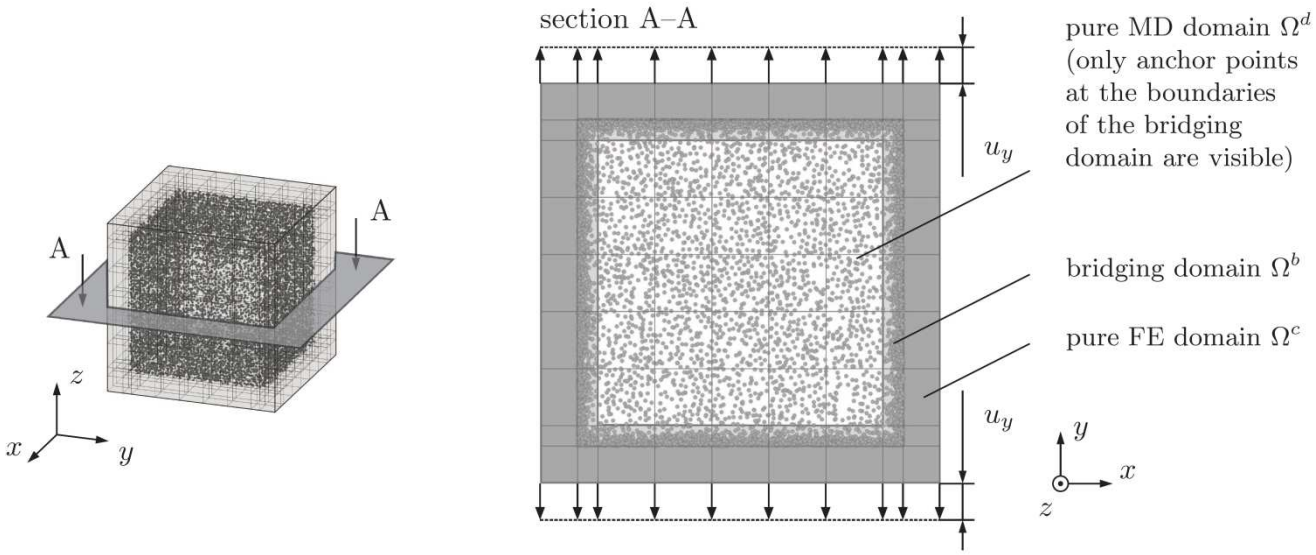

Figure 10: Coupled system subjected to prescribed displacements u_y at the top and bottom xz - surfaces, 3d view (left) and sectional view A–A (right)

However, before applying any deformation, an initial equilibration is required in order to find an appropriate starting configuration of the MD particles and anchor points. This is necessary due to the following reasons: on the one hand, the anchor point positions are not in equilibrium since they have been chosen randomly and on the other hand, shorter chain lengths caused by switching from PBCs to SBCs lead to density deviations in the boundary region. Thus, the staggered coupling algorithm as introduced in Section 4.3 is employed, using a very soft FE part, i.e. the Young's modulus chosen is very low ($E = 0.1$ MPa) and Poisson's ratio is set to zero. Furthermore, no Dirichlet boundary conditions are applied to the FE domain, except those required to avoid rigid body motion. Moreover, a simulation time of 0.5 ns in each MD–FE iteration step is chosen for the MD system.

The diagonal elements of the stress tensor in the MD domain were calculated with the help of the anchor point forces. They were obtained by collecting the components of the anchor point forces that are perpendicular to the surface of the box divided by the area of the surface, except for a region of 1.5 *nm* width at the margin of the simulation box which is equal to the thickness of the boundary region. Figure 11 shows the three diagonal elements of the stress tensor as a function of the number of MD-FE iterations. All three components have the same behaviour. They start at 6000 kPa and finally converge to zero. The stress fluctuates around zero after 125 iterations which means that the anchor points are in the equilibrium positions. The final configuration of this step was used for the next step to

apply a deformation to the box. During the initial equilibration the size of the box did not change too much and the density in the MD region has been reduced by only 0.1%.

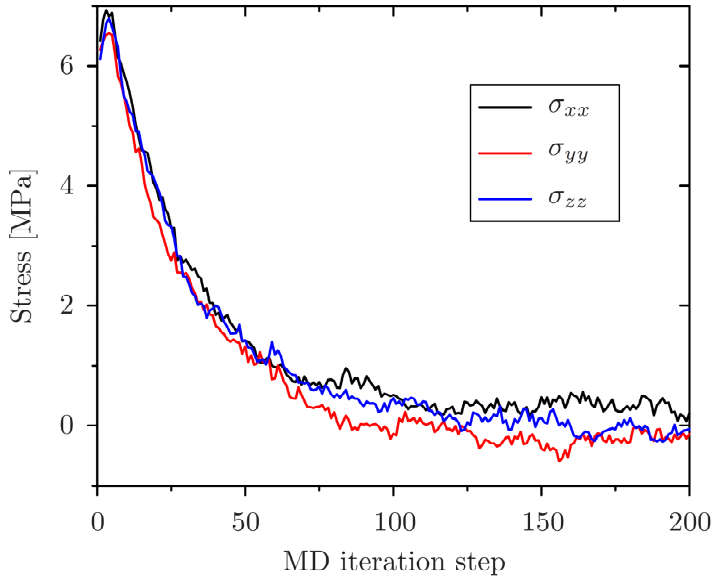

Figure 11: Three diagonal elements of stress tensor which were obtained from the anchor point forces in the MD-FE equilibration procedure.

4.4.2 Convergence criteria

In order to investigate the performance of the coupling procedure, a pure FE cube is used as a reference system. The overall edge length and the discretization is chosen identical to the FE part of the coupled system. Both the coupled and the pure FE cube are subjected to the same boundary conditions and material parameters. Thus, the reaction forces due to Dirichlet boundary conditions and the Cauchy stresses at the surfaces can be compared to each other. The reaction forces at the surface of the coupled system are defined as

$$\mathbf{f}_{cpl}^{ext} = \left\{ \mathbf{f}_{c\,I}^{ext} \right\} \quad I : \textit{node index at the surfaces}, \tag{60}$$

while the reaction forces at the surfaces of the pure FE system are introduced as $\mathbf{f}_{FE}^{ext}$. The relative deviation between reaction forces of the coupled and the pure FE system is defined as:

$$e_j^f = \frac{\sum_I \left| f_{cpl\,I\,j}^{ext} - f_{FE\,I\,j}^{ext} \right|}{\sum_I \left| f_{FE\,I\,j}^{ext} \right|}, \qquad j = x, y, z, \quad I : \textit{node index at the surfaces} \tag{61}$$

In (61), the sum of nodal deviations in reaction forces is divided by the sum of reaction forces computed in the pure FE simulation. In order to avoid neutralization of positive and negative contributions, the absolute values are employed to define e_j^f. Similarly, the deviation between Cauchy stresses is introduced as

$$e^{\sigma}_{jk} = \frac{\sum_I \left| \sigma_{cpl\,jk}(\mathbf{X}_I) - \sigma_{FE\,jk}(\mathbf{X}_I) \right|}{\sum_I \left| \sigma_{FE\,jk}(\mathbf{X}_I) \right|}, \quad j,k = x,y,z, \quad I: \textit{node index at the surfaces} \tag{62}$$

which considers each node at the surfaces. Again, the nodal contributions of stress deviations are evaluated with respect to the stresses of the pure FE cube. Nonzero values e^{f}_{j} and e^{σ}_{jk} indicate differences in the description accessible by a bare continuum model and the coupled system under consideration of particle effects. In the following we will concentrate on deviations in the y-direction in which the system is stretched: thus we will focus on e^{f}_{y} and on e^{σ}_{yy}. With these measures at hand, convergence criteria can be formulated which are based on the comparison to a pure FE system:

a) Convergence in the deviation of the reaction forces in the y-direction at iteration step i:

$$\Delta e^{f}_{y(i)} = e^{f}_{y(i)} - e^{f}_{y(i-1)}; \quad |\Delta e^{f}_{y(i)}| < tol_a \tag{63}$$

b) Convergence in the deviation of the Cauchy stress σ_{yy} at iteration step i:

$$\Delta e^{\sigma}_{yy(i)} = e^{\sigma}_{yy(i)} - e^{\sigma}_{yy(i-1)}; \quad |\Delta e^{\sigma}_{yy(i)}| < tol_b \tag{64}$$

Convergence of a coupled simulation is reached if one (or both) of these conditions is met, i.e. if $\Delta e^{f}_{y(i)}$ or $\Delta e^{\sigma}_{yy(i)}$ are lower than a predefined threshold, see (62) and (63).

In addition to these criteria, which require comparison to a reference system, break conditions can be introduced that use data inherent to the system under consideration. For example, the mean value of the Cauchy stress σ_{jk} at surface nodes (number: n_I) of the FE cube can be computed:

$$\bar{\sigma}_{jk} = \frac{1}{n_I} \sum_I \sigma_{cpl\,jk}(\mathbf{X}_I), \quad j,k = x,y,z, \quad I: \textit{node index at the surfaces} \tag{65}$$

Consequently, a third convergence criterion for the investigations in this contribution is the relative difference of $\bar{\sigma}_{yy}$ in two subsequent iteration steps:

c) Convergence in $\bar{\sigma}_{yy}$ at iteration step i:

$$\Delta \bar{\sigma}_{yy(i)} = \frac{\bar{\sigma}_{yy(i)} - \bar{\sigma}_{yy(i-1)}}{\bar{\sigma}_{yy(i-1)}}; \quad |\Delta \bar{\sigma}_{yy(i)}| < tol_c \tag{66}$$

In analogy to the cases discussed above, convergence is reached if $|\Delta \bar{\sigma}_{yy(i)}|$ is smaller than tol_c.

The suitability of these criteria will be discussed subsequently at the example of a polystyrene system coupled to FE. The parameters are:

Young's modulus (FE)	$E = 800\ MPa$
Poisson's ratio (FE)	$\nu = 0.3$
spring constant (between anchor points and MD beads)	$k_1 = 2.32\ \frac{N}{m}$
weighting factor	$\alpha = 0.5$
strain	$\varepsilon_{yy} = 1\%$
number of anchor points	$n^{MS} = 9004$
number of FE nodes	936
number of nodes in Lagrangian multiplier space	448
total number of DOFs	31164
L_2-norm	

The discretization of the Lagrangian multipliers is the same as for the geometry of the continuum and for the displacements. In the system under consideration, the boundary region contains 448 FE nodes as well as the same number of nodes in the Lagrangian multiplier space. Furthermore, the pure FE system is computed with the same Young's modulus and Poisson's ratio, but consists of 1000 FE nodes.

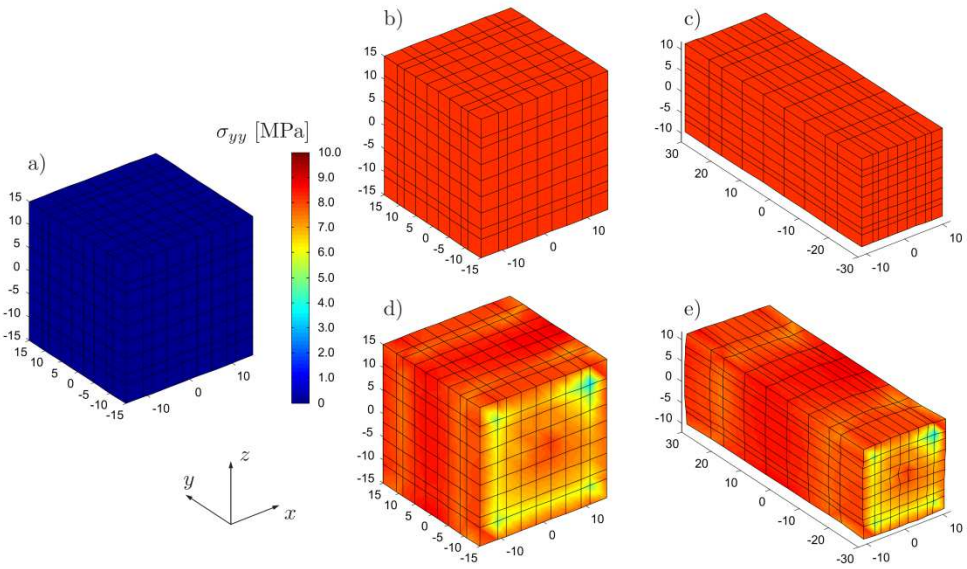

Figure 12: Uniaxial tension test, comparison of pure FE (b, c) and coupled MD–FE (d, e) simulation: $E = 800\ MPa$, $\varepsilon_{yy} = 1\%$, after 100 iteration steps between MD and FE, the unit of stress is $[MPa]$, the unit of length is [nm]: a) undeformed system, b) and c) $\sigma_{FE\,yy}$ of the deformed system, d) and e) $\sigma_{cpl\,yy}$ of the deformed system; in c) and e) the displacements are scaled by 100.

In Figure 12, the normal stresses in the y-direction are plotted in case of a pure FE simulation, cf. b) and c), as well as for a coupled simulation, cf. d) and e). In order to demonstrate the deformation behaviour, the displacements are scaled by factor of 100 in c) and e). As expected, the pure FE cube deforms to a cuboid and shows a uniform normal stress distribution $\sigma_{FE\,yy} = E\,\varepsilon_{yy} = 8.0\ MPa$. In case of the coupled simulation, the deformed configuration is very similar to a cuboid, while the stress distribution is not longer uniform. In the vicinity of the boundary region, the stress of the coupled system is lower (lowest value approximately $3.60\ MPa$), while it is very close to that of the pure FE domain in the centre of the xz-surface (approximately $7.98\ MPa$). Furthermore, the stress at the yz- and xy-surfaces is distributed quite uniformly and does not deviate very much from that of the pure FE system. In order to quantitatively investigate this, the relative deviation between the stresses of the pure and coupled simulations is introduced:

$$\delta\sigma_{jk}(\mathbf{X}_I) = \frac{\sigma_{cpl\,jk}(\mathbf{X}_I) - \sigma_{FE\,jk}(\mathbf{X}_I)}{\sigma_{FE\,jk}(\mathbf{X}_I)}, \quad j,k = x,y,z, \quad I: \textit{node index at the surfaces} \tag{67}$$

This deviation is plotted in Figure 13. In accordance with Figure 12, there is a non-negligible deviation near the bridging domain, especially at the corners, while it is much lower in the remaining parts of the system.

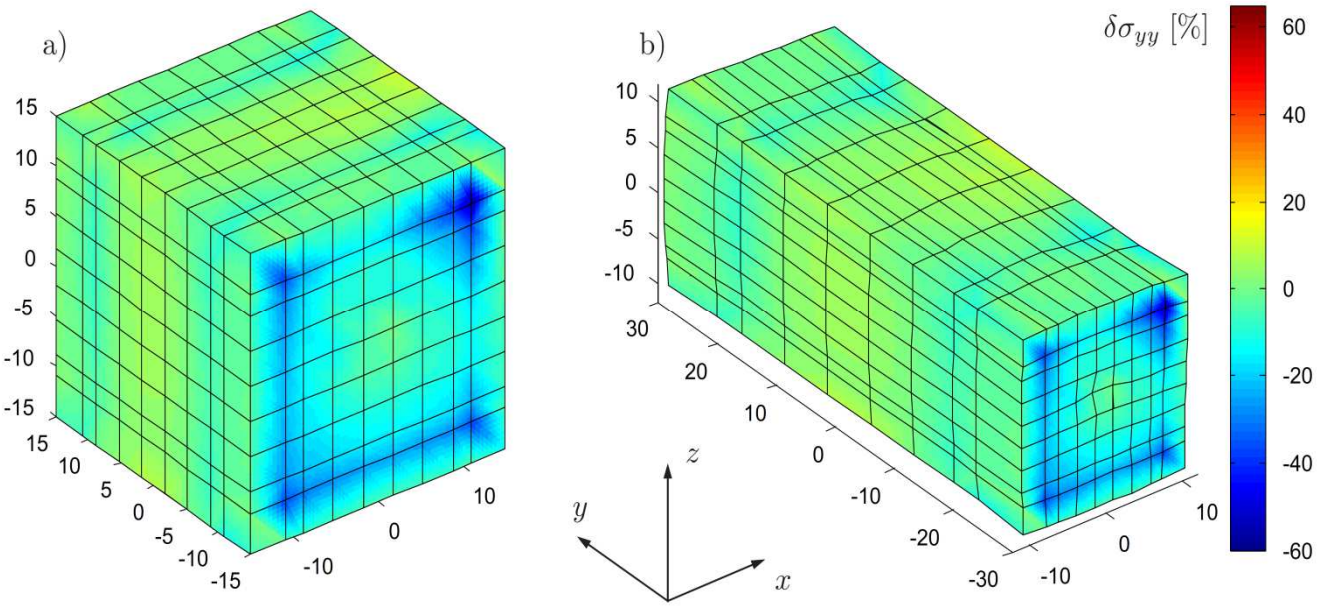

Figure 13: Uniaxial tension test, $E = 800\ MPa$, $\varepsilon_{yy} = 1\%$, after 100 iteration steps between MD and FE: $\delta\sigma_{yy}$ [%] interpolated between nodes at the surfaces, a) actual deformation, b) displacements scaled by 100

Furthermore, convergence criterion a), cf. (63), is given in Figure 12: the initial deviation of 227.6% decreases to 12.8%, while Δe_y^f amounts to only 0.058% after 100 MD–FE iteration steps. Thus, the system does not change significantly any more and convergence can be assumed.

Roughly the same behaviour is obtained in case of convergence criterion b), cf. (64) and Figure 13. Here, the initial deviation is 123.0% and decreases to 8.0%. After 100 MD–FE iteration steps, Δe_{yy}^{σ} is 0.0039%.

In contrast to the criteria discussed above, convergence of the system can be obtained independently of a pure FE simulation by evaluating $\overline{\sigma}_{yy}$ as well as $\Delta\overline{\sigma}_{yy}$, cf. (65) and (66). The results are plotted in Figure 16: starting at $15.81\ MPa$, $\overline{\sigma}_{yy}$ decreases to $7.56\ MPa$ after 100 iteration steps. Compared to a pure FE simulation with a constant value of $8.00\ MPa$, which is equal to the analytic result, there is a relative deviation of approximately 5.5%. After 100 iteration steps $\overline{\sigma}_{yy}$ amounts to only -0.024% which makes it a suitable convergence criterion since it does not require comparison to a pure FE system.

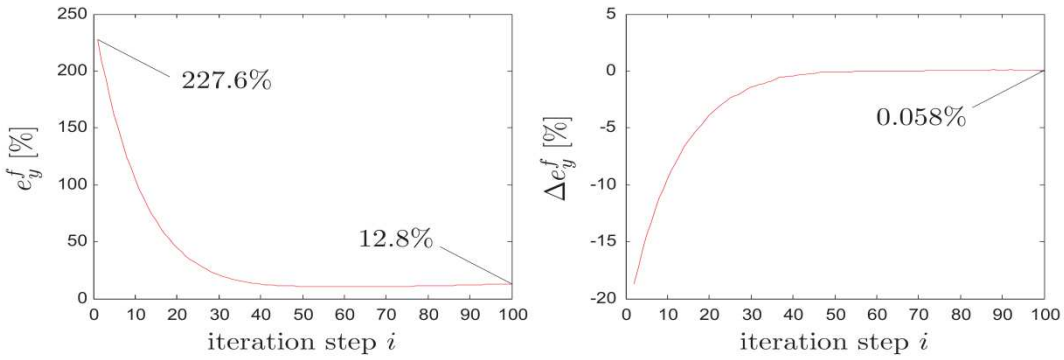

Figure 14: Coupled simulation, uniaxial tension test, $E = 800\ MPa$, $\varepsilon_{yy} = 1\%$: deviation of reaction forces e_y^f and convergence behaviour of Δe_y^f versus MD–FE iteration step i

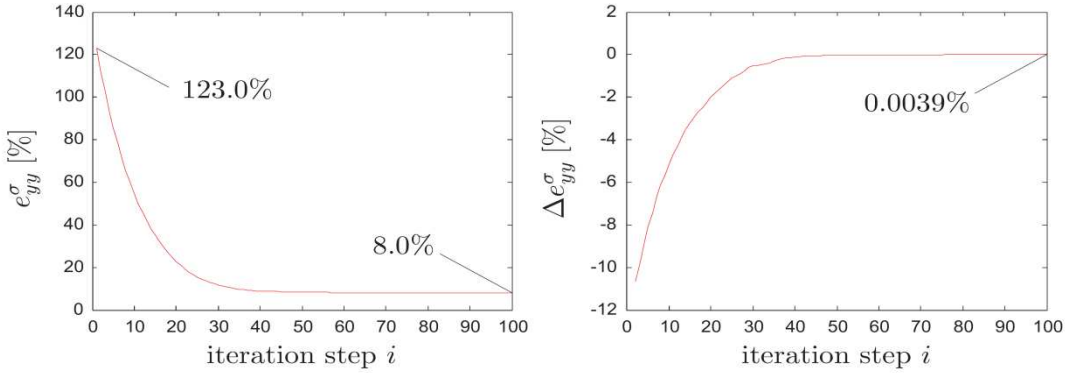

Figure 15: Coupled simulation, uniaxial tension test, $E = 800\ MPa$, $\varepsilon_{yy} = 1\%$: deviation of normal stress e_{yy}^{σ} and convergence behaviour of Δe_{yy}^{σ} versus MD–FE iteration step i

After 100 iteration steps, $|\Delta\bar{\sigma}_{yy}|$ is significantly lower than 0.1%, thus, the number of iteration steps chosen for this investigation seems to be reasonable. Consequently, at least 100 iteration steps are computed for each system and the convergence is checked based on a comparison to a reference system by using criteria a) and b) as well as c). All three criteria are used in consideration of the following reasons:

- Criterion a) is based on reaction forces as a direct output of the simulation; due to the comparison to a reference system, performance and results of the coupled computation can be investigated and evaluated;
- Criterion b) allows for a better understanding and visualization of the deviations between the coupled and the pure FE system, especially in case of uniaxial tension tests;
- Criterion c) does not depend on the comparison to a reference system. Thus, it is a well suited criterion for systems that cannot be computed using a pure FE approach, which is exactly the intention of the coupling method;

It has to be mentioned here, that the focus of this contribution lies on the methodology and performance of the coupling method proposed here. This, of course, requires a quantification of convergence which can be evaluated using the criteria given above. Nevertheless, this work does not yet aim at a specification of the threshold parameters tol_a, tol_b, and tol_c, which would necessitate much more experience in the application of the method. Instead, we decided, based on the findings presented in this section, that a number of 100 MD–FE iteration steps is a reasonable choice for the very first investigations. On the one hand, already quite a good convergence is obtained; on the other hand, the computational time is still acceptable.

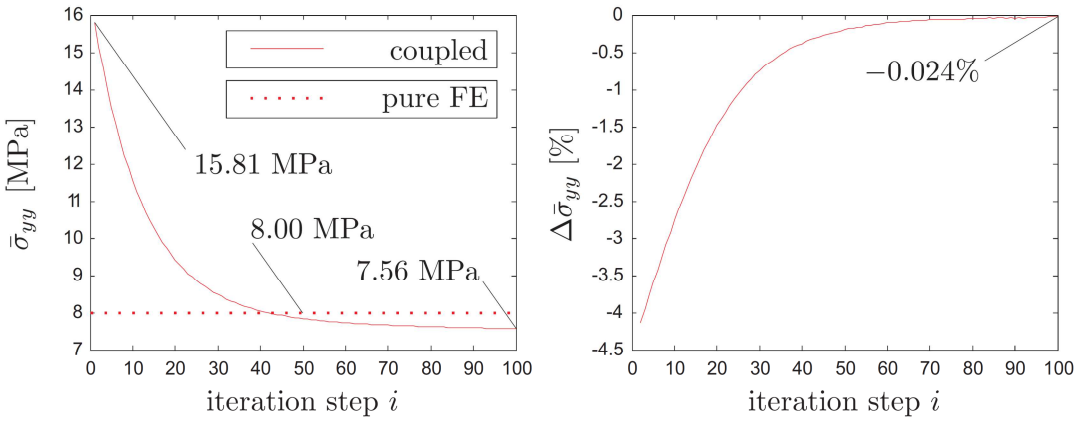

Figure 16: Uniaxial tension test, $E = 800\ MPa$, $\varepsilon_{yy} = 1\%$: mean value of normal stress $\bar{\sigma}_{yy}$ (coupled and pure FE simulation) and convergence behaviour of $\Delta\bar{\sigma}_{yy}$ versus MD–FE iteration step i

4.4.3 Example 1: coupled simulation of pure polystyrene

In this section, we systematically investigate a system of pure polystyrene coupled to a finite element domain. The main focus is on the influence of Young's modulus on the coupled simulation and on the observed differences to the pure FE system. The parameters are the same as introduced in Section 4.1, except Young's modulus which is varied from 400 *MPa* to 1500 *MPa* on the FE side. The Young's modulus on the MD side is constant 827 *MPa* .

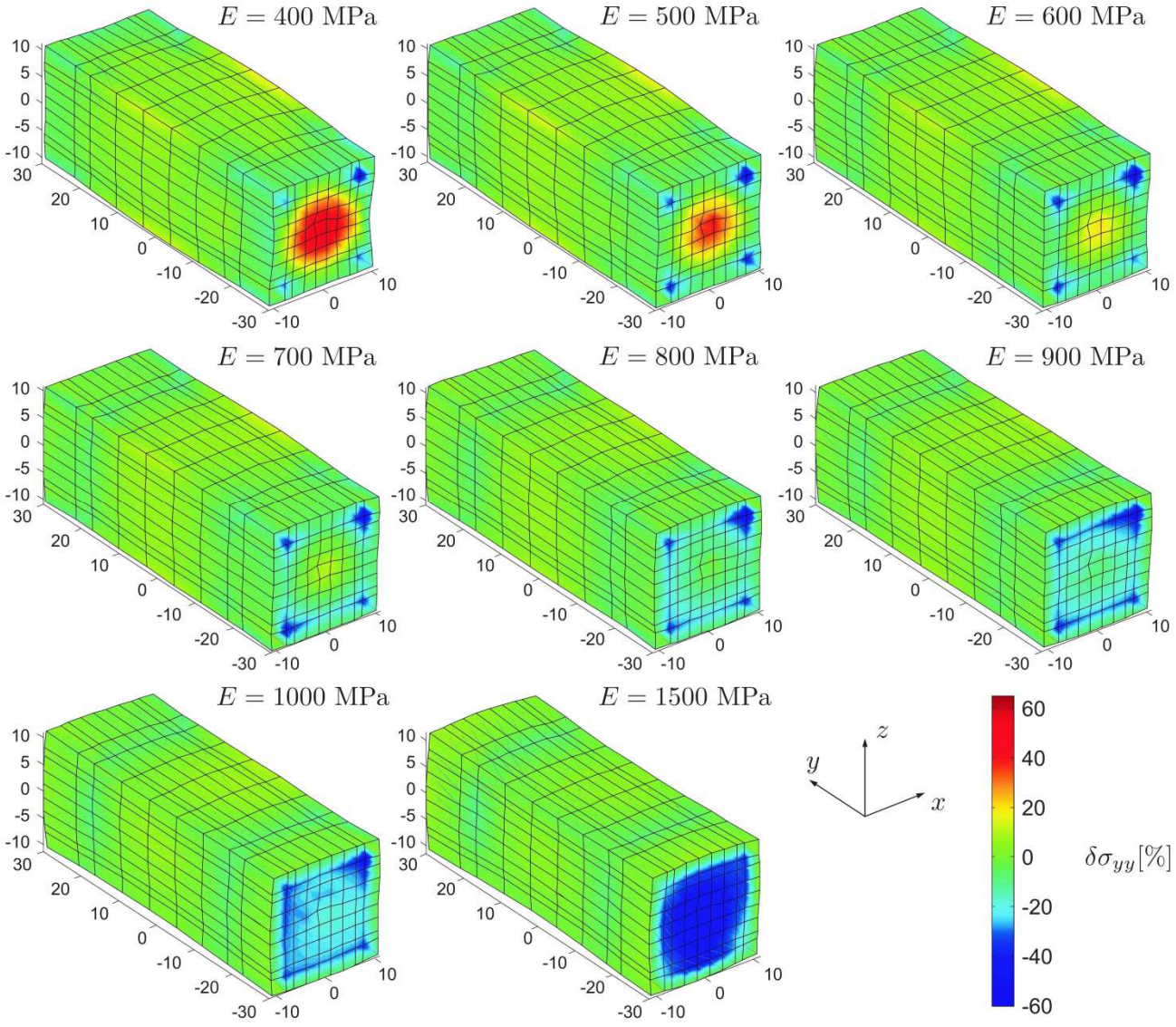

Figure 17: Deviation e^{σ}_{yy} *of the normal stress* σ_{yy} *of polystyrene, coupled to an FE domain; the Young's modulus of the FE part varies from* 400 *MPa (top left) to* 1500 *MPa (bottom centre), the displacements are scaled by 100*

First, the deformation behaviour of the coupled system is investigated qualitatively: to do so, the actual displacements of the FE nodes are scaled by factor of 100. In Figure 17, the deformation of the pure polystyrene system is plotted together with the deviation $\delta\sigma_{yy}$ of normal stresses in the y-direction. In case of $E = 400\ MPa$, the particle domain is stiffer than the finite element part which, on the one hand, causes higher normal stresses in the centre of the xz-surfaces and, on the other hand, less contraction in the middle of the system. Both effects are clearly visible in Figure 17, whereby positive values of $\delta\sigma_{yy}$ express higher stress of the coupled simulation due to definition (67). For $E = 1500\ MPa$, the particle domain is significantly softer than the continuum which leads to a higher contraction in the middle and lower stresses in the centre of the xz-surfaces. Again, this is supported by the results shown in Figure 17. The smallest deviation $\delta\sigma_{yy}$ as well as the most uniform contraction perpendicular to the load direction are obtained for Young's moduli between $E = 600\ MPa$ and $E = 900\ MPa$.

In order to quantify these observations, the deviations of reaction forces e_y^f and of normal stress e_{yy}^σ are investigated. In Figure 18, e_y^f and e_{yy}^σ are plotted as a function of E: qualitatively, both curves show the same behaviour. A minimum for $E = 600\ MPa$ is observed in both cases. At $E = 400\ MPa$, e_y^f is 9.40% and decreases with larger Young's moduli to a minimum of 6.80% at $E = 600\ MPa$. After that, e_y^f increases and becomes 11.80% at $E = 1500\ MPa$. It is expected that for Young's moduli smaller than $E = 400\ MPa$ or larger than $E = 1500\ MPa$, a further increase of e_y^f would be observed. Very similar, although at a higher level, e_{yy}^σ is 14.0% at $E = 400\ MPa$, decreases to its minimum of 8.90% at $E = 600\ MPa$, and increases to 22.80% at $E = 1500\ MPa$.

These results support the qualitative findings discussed above, where the best fit between the coupled and the FE reference simulation has been observed for E between $600\ MPa$ and $900\ MPa$. Furthermore, this is in line and of the same order of magnitude obtained from the parameter identification of a pure MD simulation, see Section 4.4.1. There, a Young's modulus of $E = 827\ MPa$ has been determined, which, however, is not exactly the same.

In order to understand this, the particle system as well as the coupling parameters used here should be considered carefully. For sure, they have a strong influence on the performance and the results of the coupled simulation. First qualitative hints can be obtained from Figure 17: in case of a Young's modulus between $E = 600\ MPa$ and $E = 900\ MPa$, quite a uniform distribution of deviations is obvious from the plots, even at the xz–surfaces. An exception are the corners near the

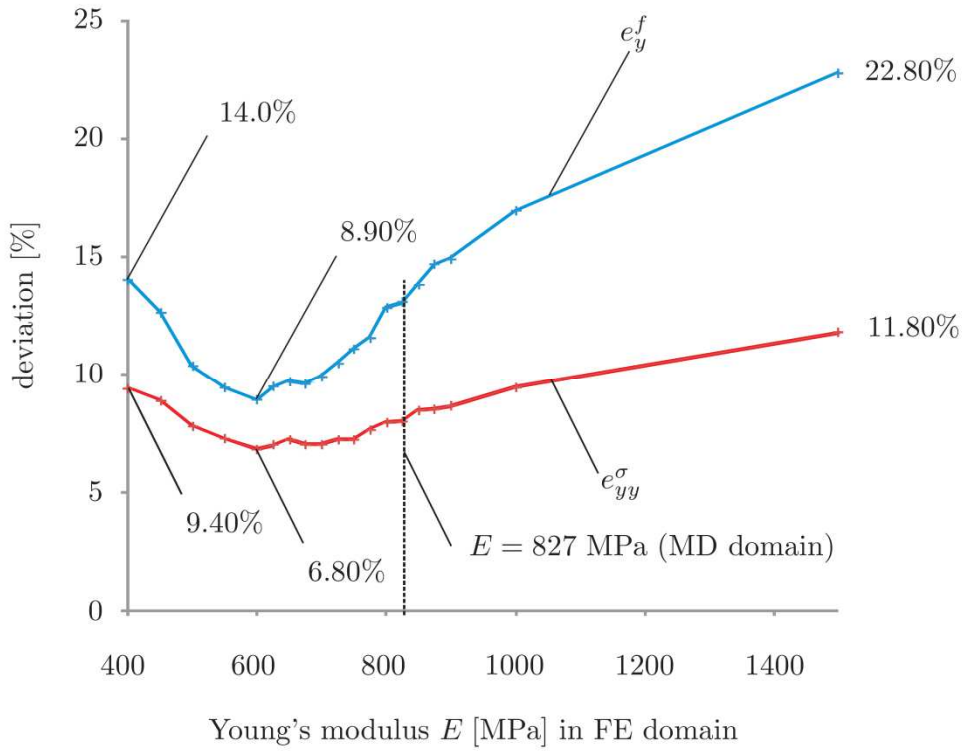

Figure 18: Coupled simulation of polystyrene: deviation of normal stress e_{yy}^σ and reaction forces e_y^f as a function of the Young's modulus of the FE domain, evaluated after 100 MD–FE iteration steps

bridging domain. Here, the deviation differs significantly which could be caused by the choice of coupling parameters, e.g. the weighting function α, but, most likely, also by the geometry of the system. Due to the cubic shape of the particle domain, sharp edges and corners occur which most likely have considerable influence on the behaviour of the particle system in these regions. The systematic investigation of theses factors is postponed to later contributions since this would exceed the scope of this work. Nevertheless, from the molecular dynamics point of view, it is assumed that the deviations in the bridging domain and especially nearby the corners are mainly caused by the following reasons:

- Since the polymer chains in the boundary region are located nearby the interface to the pure FE domain, it is supposed that their elastic behaviour differs from that of the bulk polymer. This is more pronounced at the corners since the polymer is in contact with three adjacent interfaces. Additionally, due to the artificial dynamics in the boundary region caused by the anchor point definition, it cannot be expected that the polymer in this region shows exactly the same behaviour as in the bulk.
- By construction of the MD box, the averaged chain length in the boundary region is 8 monomers per chain, which is very short compared to the pure MD region where it amounts to

200 monomers per chain. Especially near the interface to the FE domain the chain length is further reduced. Some chains are shorter than the entanglement length which has significant influence on the elastic properties of polymers [32], [33]. Usually, Young's modulus increases with the chain length. This coincides with the qualitative findings in Figure 17: near the corners of the bridging domain, $\delta\sigma_{yy}$ is negative for all Young's moduli considered. This means that the particle domain is softer than the FE domain, which could be caused by the reduced chain length in this region.

Finally, the convergence behaviour is investigated by comparing the criteria introduced above. All systems have been computed for 100 MD–FE iteration steps, not yet employing any break condition based on certain thresholds. Instead, the convergence criteria are evaluated at iteration step 100 and presented as a function of the Young's modulus of the FE domain, cf. Table 1. It is observed that all values of $|\Delta e^{f}_{y(100)}|$, $|\Delta e^{\sigma}_{yy(100)}|$, and $|\Delta \overline{\sigma}_{yy(100)}|$ are significantly lower than 1% , which is very promising. Thus, all systems have reached an equilibrium configuration, i.e. convergence can be stated. Furthermore, $\Delta e^{f}_{y(100)}$ and $\Delta e^{\sigma}_{yy(100)}$ show the lowest absolute values for Young's moduli between $E = 600\ MPa$ and $E = 900\ MPa$, which is the same range as for the stress deviations in Figure 17. Additionally, the lowest values of e^{f}_{y} and e^{σ}_{yy} lie in the same interval, cf. Figure 18. Pending further investigations, it can be assumed that there is a certain relation between the convergence behaviour and the lowest deviation with respect to a pure FE simulation. However, further decrease of $|\Delta e^{f}_{y(100)}|$ and $|\Delta e^{\sigma}_{yy(100)}|$ values for higher Young's moduli have to be noted as well. This is caused probably by the fact that the stiffness of the system is increasingly dominated by the FE region when the Young's modulus is chosen larger while the influence of the particle region is reduced. Thus, we assume that the system's response becomes more similar to the pure, static FE system which requires less MD–FE iteration steps to reach any convergence criterion. From our point of view, the same reason can be assumed for the decrease of $|\Delta \overline{\sigma}_{yy(100)}|$ with increasing Young's moduli.

E [MPa]	$\Delta e^{f}_{y(100)}$ [%]	$\Delta e^{\sigma}_{yy(100)}$ [%]	$\Delta \overline{\sigma}_{yy(100)}$ [%]
400	-0.1687	-0.0765	-0.0909
500	-0.0694	-0.0386	-0.0581
600	-0.0140	-0.0288	-0.0422
700	0.0356	-0.0038	-0.0338
800	0.0578	0.0039	-0.0236
900	0.0547	0.0058	-0.0233
1000	0.0528	0.0167	-0.0234
1500	0.0259	0.0118	-0.0076

Table 1: Coupled simulation of pure polystyrene: convergence criteria evaluated after 100 MD–FE iteration steps for different FE-Young's moduli E

4.4.4 Example 2: coupled simulation of a nanocomposite

In this section, the system under consideration is polystyrene enclosing a single silica nano–filler particle. The interaction parameters used for the polystyrene part are the same as described in Section 4.4.3. For silica we have used a setup that had been adopted already in a CG MD study of PS-silica nanocomposites [34]. In the mapping scheme of silica a SiO_2 unit is represented by a CG bead, the centre of which is located at the Si site. The nanoparticle of a 4 nm diameter is defined by 873 beads. The interaction potentials between polystyrene and the silica nanoparticle were again obtained by Iterative Boltzmann Inversion [21]. The surface beads of the nanoparticle have a dominant contribution to the interaction with the polymer matrix. The interaction of the polymer with the inner core beads is weaker. This behaviour is considered by different interaction potentials between PS and surface beads as well as between PS and core beads. The mapping scheme, the method to develop the CG potential and also the validation of the CG potential were explained with more detail in [34]. A qualitative representation of the nanocomposite is shown in Figure 19. The filler particle is located in the centre of the particle region; it is surrounded by the PS matrix. The volume fraction of the nanoparticle is approximately 0.6%, which is rather small. Nevertheless, this seems to be sufficient to estimate the capability of the new MD-FE coupling technique in such inhomogeneous systems which cannot be treated by pure FE methods with an accuracy as accessible by particle-based computations. Coupled simulations with an enlarged volume fraction of the nanoparticle should, in principle, cause no computational problems. The model parameters of the nanocomposite such as temperature, pressure, length and number of the polymer chains, etc. are the same as adopted in the pure PS example.

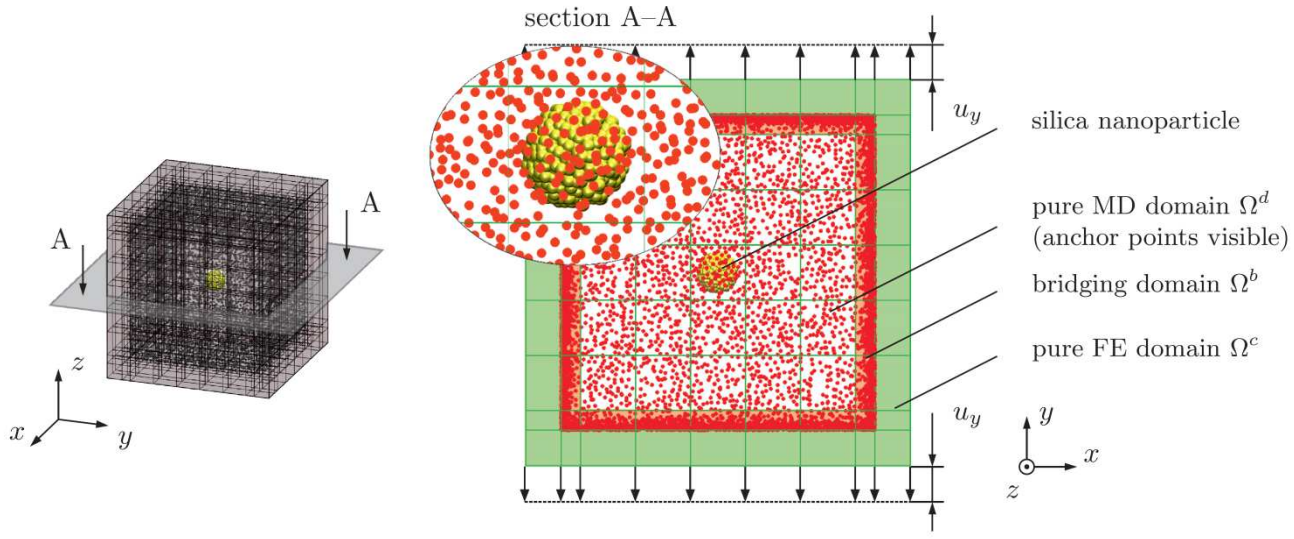

Figure 19: Coupled system with silica nanoparticle subjected to prescribed displacements u_y at the upper and lower xz -surfaces; for proper visualization, only the anchor points and the silica particle are plotted schematically, 3d view (left) and sectional view A–A (right)

For the nanocomposite the same simulations have been carried out as for pure polystyrene. Due to the small volume fraction, no qualitative differences have been obtained, only small quantitative deviations occurred. Thus, we do not discuss these results in detail. In extension to the previous simulations, the system is now subjected to several load steps, each of 1% in order to investigate the performance beyond the approximately linear elastic region. Due to the small volume fraction of the filler particle, the Young's modulus of the MD domain remains at $E = 827\ MPa$ which is the same value as obtained for the pure PS system.

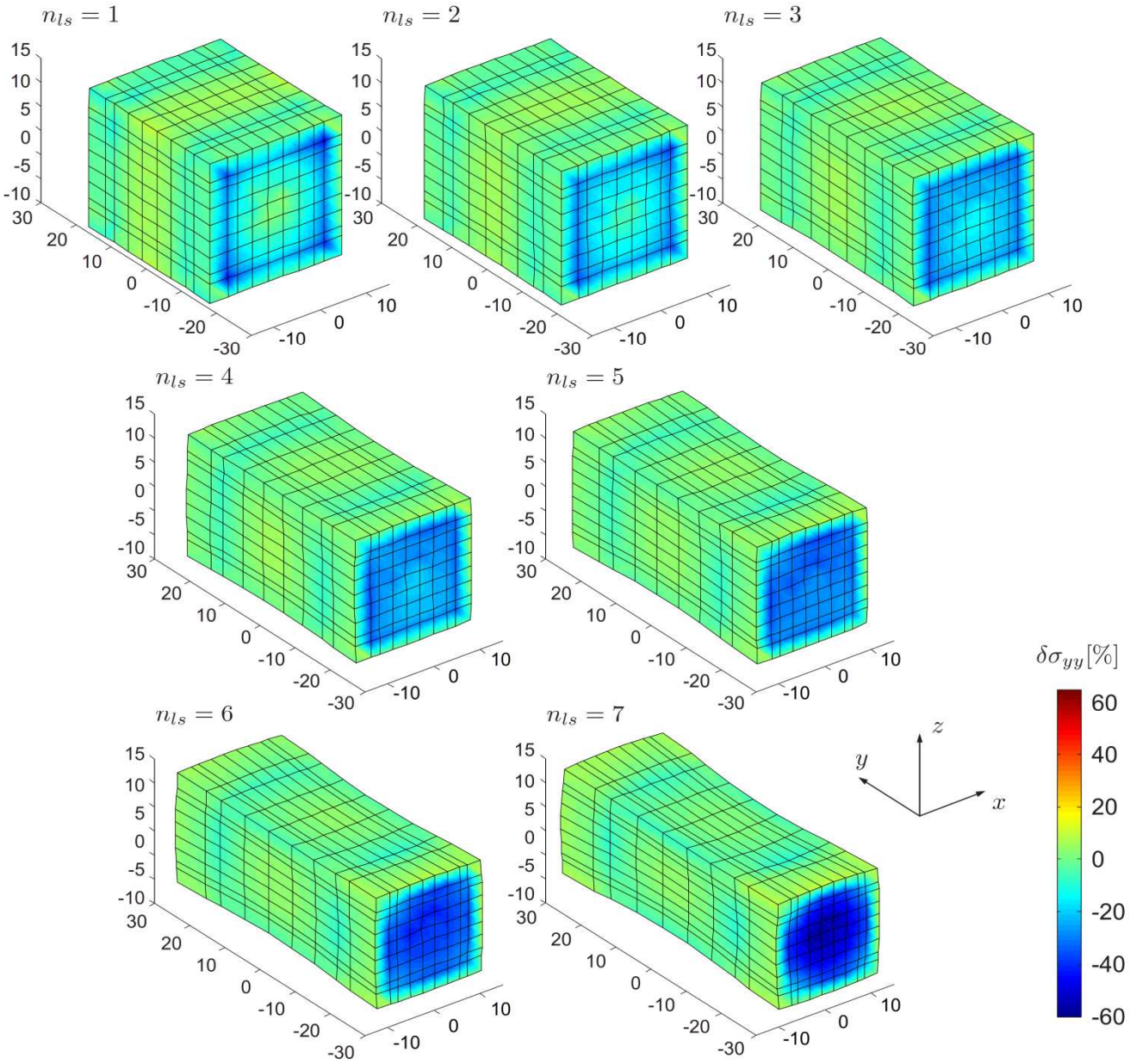

Figure 20: Coupled simulation of polystyrene with a silica nanoparticle; Young's modulus of the FE system: $E = 800\ MPa$, *number of load steps:* $n_{ls} = 7$, *number of MD–FE iteration steps per load step:* $n_{MD} = 100$; *deviation* $\delta\sigma_{yy}$ *of normal stress* σ_{yy} *plotted after each load step, displacements are scaled by factor of 15*

In Figure 20 the normal stress deviations $\delta\sigma_{yy}$ are plotted at the surfaces of the FE domain in case of $E = 800\ MPa$. Due to the findings of the pure PS system it can be expected that the minimum deviations e_y^f and e_{yy}^σ would be obtained for Young's moduli of the FE system significantly lower than that from the parameter identification of the MD system, cf. Figure 18. Furthermore, in order to get results comparable to those of the pure PS system, a Young's modulus of $E = 800\ MPa$ is chosen which is slightly lower than that of the MD system. The displacements shown here are scaled by a factor of 15. As in case of pure polystyrene, the deviations are close to zero at the xz – and at the yz – surfaces, whereas its absolute values are larger at the xz –surfaces which are perpendicular to the load direction. At these surfaces it is clearly visible that the absolute deviations increase with an increasing number of load steps. The actual deviations are mainly negative which means that the particle domain is softer than the FE region, in particular for strains larger than three percent.

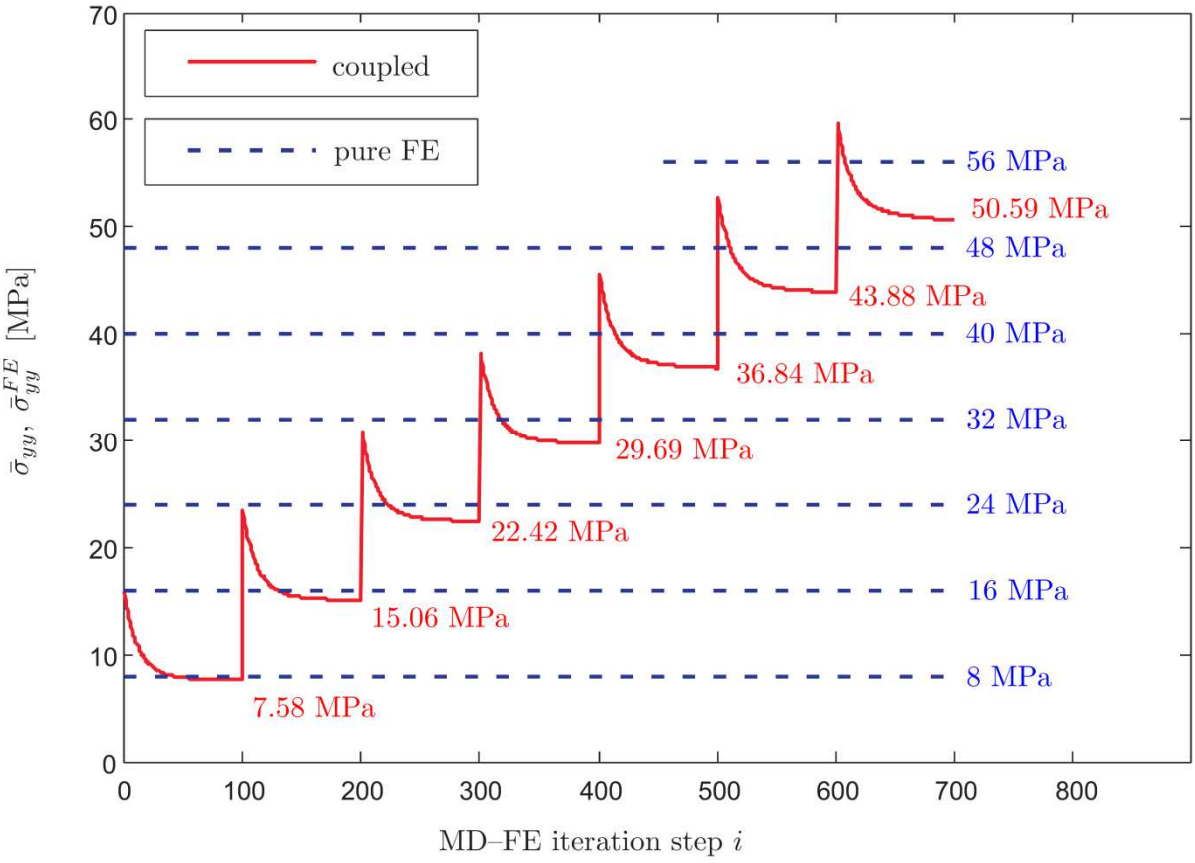

Figure 21: Coupled simulation with silica nanoparticle, seven loads steps, 1% strain each, Young's modulus of the FE domain: 800 *MPa ; mean values of normal stress* $\bar{\sigma}_{yy}$ *(coupled nanocomposite) and* $\bar{\sigma}_{yy}^{FE}$ *(pure FE simulation) versus iteration steps, 100 MD–FE iterations equal one load step*

This observation is quantified in Figure 21: the mean values of the tensile normal stress from the coupled and the FE reference simulation, $\overline{\sigma}_{yy}$ and $\overline{\sigma}_{yy}^{FE}$, are plotted versus iteration and load steps. It is clearly visible that the coupled simulation converges to approximately constant values of $\overline{\sigma}_{yy}$ within 100 MD–FE iterations for each load step. Thus, the system reaches an equilibrated configuration in each load step, which demonstrates that the coupling method is also able to treat polymer systems with filler particles. The absolute deviation between the results of the coupled and the reference simulation increases with the strain level applied. This is not surprising since the strain considered here is beyond the linear elastic part of the stress–strain curve, cf. Figure 9. In order to capture the nonlinear behaviour of the particle system, the FE domain has to be extended to geometrical and physical nonlinearity, which is work in progress.

Furthermore, the curves plotted in Figure 21 are very similar to those known from stress relaxation experiments of viscoelastic materials: the stress decreases when the specimen is subjected to constant strain. In the coupled simulation, the conditions are similar: a certain strain is applied to the FE domain and is kept constant during all MD–FE iteration steps within each load step. Thus, the MD domain has to follow this deformation which is not possible instantly, but requires time for relaxation. It is not clear yet up to which part or whether at all the stress decreases observed in Figure 21 are caused simply by artefacts of the coupling procedure or if they result from the viscoelasticity of the polystyrene reproduced by the MD-part. Possibly, the reason is a combination of both; however, careful and intense investigations are required to work out the effects taking place and thus to understand these findings. Though, this would exceed the purpose of this work and has to be postponed to a later contribution.

A quantitative overview of the deviations and convergence criteria introduced in Section 4.4.2 is given in Table 2 which supports the qualitative observations. It is obvious that the deviation of stresses e_{yy}^{σ} is much more sensitive to the mismatch between the coupled and the reference system. Compared to e_y^f, it renders a smaller deviation of 7.58% in the first load step, but it increases to 50.59% in the seventh load step which is about twice the value of e_y^f. Generally, all convergence criteria are significantly lower than 0.1% such that convergence can be assumed.

Figure 22 depicts the mean values of the normal stress after 100 MD–FE iterations per load step for the coupled simulation ($\overline{\sigma}_{yy\,(100)}$) and for the FE simulation ($\overline{\sigma}_{yy\,(100)}^{FE}$). From this plot, the nonlinear behaviour of the coupled system is clearly visible.

load step i_{ls}	1	2	3	4	5	6	7
$e^{f}_{y\,(100)}[\%]$	12.16	13.79	15.63	17.24	19.07	20.97	24.09
$e^{\sigma}_{yy\,(100)}[\%]$	7.58	15.06	22.42	29.69	36.84	43.88	50.59
$\Delta e^{f}_{y\,(100)}[\%]$	0.0674	0.0413	0.0240	0.0305	0.0315	0.0301	0.0521
$\Delta e^{\sigma}_{yy\,(100)}[\%]$	0.0043	0.0075	0.0040	0.0130	0.0153	0.0177	0.0271
$\Delta\overline{\sigma}_{yy\,(100)}[\%]$	-0.0283	-0.0161	-0.0089	-0.0121	-0.0120	-0.0120	-0.0186

Table 4: Coupled simulation of polystyrene with nanoparticle: e^{f}_{y}, e^{σ}_{yy}, $\Delta e^{f}_{y\,(100)}$, $\Delta e^{\sigma}_{yy\,(100)}$, and $\Delta\overline{\sigma}_{yy\,(100)}$ after 100 MD–FE iterations per load step

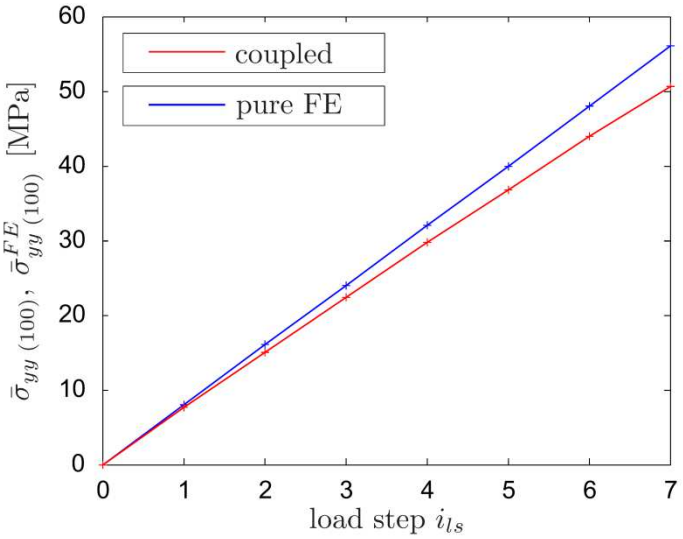

Figure 22: Comparison of the coupled nanocomposite and the pure FE simulation: mean values of the normal stress in load direction $\overline{\sigma}_{yy\,(100)}$ (coupled system) and $\overline{\sigma}^{FE}_{yy\,(100)}$ (pure FE system) after 100 MD–FE iterations for each load step versus load step i_{ls}; the Young's modulus is $E = 800$ MPa and a strain of 1% is applied in each load step

In the subsequent section the results obtained so far are summarized and an outlook for future investigations is given.

4.5 Summary and outlook

A number of hybrid simulation techniques to couple a particle domain to a continuum has been developed in recent years. The large majority of these simulation procedures is however restricted to particle regions that are crystalline, e.g. [6]. The complexity of this type of hybrid simulations is largely simplified for the case of space-fixed particles. Coupled particle–continuum simulations for amorphous polymers, polymer nanocomposites, liquid crystals or liquids are still an exception. Recent

hybrid simulation studies of these materials only allowed the coupling of particle domains which are mapped in different resolutions (atomistic versus coarse grained picture) [35]. This deficit in particle–continuum simulations for soft–matter systems motivated us to develop a hybrid technique allowing for a true coupling of continuum and particle domains with flexible atoms or CG beads. Such an approach would fill the gap between continuum models and particle approaches in new soft-matter materials such as nanocomposites which are in the focus of intensive academic and industrial research. To couple the two "worlds", a number of theoretical steps which are non-standard in both domains considered had to be implemented or even developed. For the description of the particle space a molecular dynamics formalism working with stochastic boundary conditions has been employed [22], [36]. The conventional periodic boundary conditions adopted in the majority of M simulations are incompatible with the spatial arrangement of the different domains of the coupled system. Nonperiodic stochastic boundary conditions have proven to be a suitable choice for the present hybrid approach.

To perform simulations of large particle domains, which is the final aim of the present long–term research, a coarse grained resolution has been chosen [18]. Standard Newton's equations of motion in a classical MD description are solved in the inner core part of the coupled system which only contains the particles - in the present realization CG beads - of the soft-matter sample. Our test simulations have shown that the method works best when inserting a dissipative particle domain [22], [37] to dissipate energy and to control the temperature during the simulation. The spatial region surrounding the inner MD core and the DPD domain is the actual coupling region between particle and continuum description. The information transfer between both is provided by so-called anchor points, a set of auxiliary particles that are harmonically connected to the MD particles in the coupling region. The insertion of these anchor points has two advantages: on the one hand, the flexibly tethered MD particles perturb the MD particles in the core region less than strictly position-constrained particles. On the other hand, the harmonic description for the anchor point–MD particle interaction facilitates a fast calculation of force derivatives at the anchor points, a key ingredient of the proposed iterative coupling scheme. Forces and force gradients at the anchor points are transmitted from the particle to the continuum domain. The key parameters for the opposite information transfer are the anchor point positions which can change under the influence of the surrounding continuum being subjected to any Dirichlet or Neumann boundary conditions. The anchor point concept developed for the present hybrid method implies that the continuum is treated quasi-statically while the MD domain is dynamic.

The continuum is numerically solved by the Finite Element method and connected to the MD domain using the Arlequin approach [11], [12], [13]. In order to solve the coupled system, a staggered iteration procedure has been set up together with an appropriate implementation of the information transfer between both domains. Test calculations on simple one-dimensional model systems [38] have

shown possible staggered schemes to treat coupled systems. To blend the MD and FE energies in the coupling region several weighting functions have been suggested. The best choice, however, will require a careful optimization of the whole MD and FE parameter space in the present hybrid approach.

To verify the proposed method, we have performed coupled simulations on a sample of pure amorphous polystyrene as well as on a PS–silica nanocomposite. To quantify the accuracy of the coupling approach three different system descriptions have been correlated. First we have analyzed the pure PS sample in the framework of conventional MD simulations under periodic boundary conditions. These calculations provided a parameter identification, such as the evaluation of stress–strain curves and the calculation of Poisson's ratio under stress. The MD based parameters have been adopted for the second series of calculations, namely a FE simulation with input data from the particle domain.

Heart of the present study is, however, the performance of coupled MD–FE simulations. To estimate the accuracy and stability of the hybrid method several convergence criteria have been employed. Detailed discussions of the two deviations e_y^f and e_{yy}^σ of the reaction forces in the y–direction and of the Cauchy stress between a pure FE calculation and the coupled one have been given. Thereby we have verified that the stress in the coupling region is not homogeneously distributed as observed in the FE approach; it shows certain geometrical patterns. We are aware of the fact that an explanation of this phenomenon requires additional studies with the aim to optimize the design of the MD–FE coupling approach. This covers the spatial extension of the different domains, the number and position of the anchor points as well as the magnitude of the harmonic force constant between MD particles and anchor points.

Finally, plans for future research shall be mentioned. As it became obvious from this contribution, even nanocomposites can be simulated using the method developed here. Nevertheless, more complex systems as well as different load cases will have to be investigated carefully. With the coupling scheme presented and a coarse grained description, system sizes should be in reach that are useful in engineering analyses on a macroscopic scale. Finally we hope that calculations of the present type will offer an access to continuum material parameters that can be justified on the basis of particle interactions. A first step into this direction has been made within the manuscript at hand.

References

[1] Daoulas KC, Müller M, Stoykovich MP, Park SM, Papakonstantopoulos YJ, de Pablo JJ, Nealey PF, Solak HH. Fabrication of complex three-dimensional nanostructures from self-assembling block copolymer materials on two-dimensional chemically patterned templates with mismatched symmetry. *Physical Review Letters* 2006; **96**:036 104.

[2] Daoulas KC, Müller M. Single chain in mean field simulations: Quasi-instantaneous field approximation and quantitative comparison with monte carlo simulations. *The Journal of Chemical Physics* 2006; **125**:184 904.

[3] Müller M, Smith GD. Phase separation in binary mixtures containing polymers: A quantitative comparison of single-chain-in-mean-field simulations and computer simulations of the corresponding multichain systems. *Journal of Polymer Science Part B: Polymer Physics* 2005; **43**(8):934–958.

[4] Shilkrot LE, Curtin WA, Miller RE. A coupled atomistic/continuum model of defects in solids. *Journal of the Mechanics and Physics of Solids* 2002; **50**(10):2085–2106.

[5] Shilkrot LE, Miller RE, Curtin WA. Multiscale plasticity modeling: coupled atomistics and discrete location mechanics. *Journal of the Mechanics and Physics of Solids* 2004; **52**(4):755 – 787.

[6] Tadmor EB, Ortiz M, Phillips R. Quasicontinuum analysis of defects in solids. *Philosophical Magazine A* 1996; **73**(6):1529–1563.

[7] Belytschko T, Xiao SP. Coupling methods for continuum model with molecular model. *International Journal for Multiscale Computational Engineering* 2003; **1**:115–126.

[8] Guidault PA, Belytschko T. On the l^2 and h^1 couplings for an overlapping domain decomposition method using lagrange multipliers. *International Journal for Numerical Methods in Engineering* 2007; **70**:322–350.

[9] Khare R, Mielke SL, Paci JT, Zhang S, Ballarini R, Schatz GC, Belytschko T. Coupled quantum mechanical/molecular mechanical modeling of the fracture of defective carbon nanotubes and graphene sheets. *Physical Review B* 2007; **75**:075 412.

[10] Zhang S, Khare R, Lu Q, Belytschko T. A bridging domain and strain computation method for coupled atomistic-continuum modelling of solids. *International Journal for Numerical Methods in Engineering* 2007; **70**:913–933.

[11] Ben Dhia H. Problèmes méchaniques multi-échelles: la méthode arlequin. *Comptes Rendus de l'Académie des Science, Series II b* 1998; **326**:899–904.

[12] Ben Dhia H, Rateau G. Analyse mathématique de la méthode arlequin mixte. *Comptes Rendus de l'Académie des Science, Series I* 2001; **332**:649–654.

[13] Ben Dhia H, Rateau G. The arlequin method as a flexible engineering design tool. *International Journal for Numerical Methods in Engineering* 2005; **62**:1442–1462.

[14] Bauman PT, Ben Dhia H, Elkhodja N, Oden JT, Prudhomme S. On the application of the arlequin method to the coupling of particle and continuum models. *Computational Mechanics* 2008; **42**:511–530.

[15] Bauman PT, Oden JT, Prudhomme S. Adaptive multiscale modeling of polymeric materials with arlequin coupling and goals algorithms. *Computer Methods in Applied Mechanics and Engineering* 2009; **198**:799–818.

[16] Chamoin L, Oden JT, Prudhomme S. A stochastic coupling method for atomic-to-continuum monte-carlo simulations. *Computer Methods in Applied Mechanics and Engineering* 2008; **197**:3530–3546.

[17] Aubertin P, Rethore J, de Borst R. Energy conservation of atomistic/continuum coupling. *International Journal for Numerical Methods in Engineering* 2009; **78**:1365–1386.

[18] Müller-Plathe F. Coarse-graining in polymer simulation: From the atomistic to the mesoscopic scale and back. *ChemPhysChem* 2002; **3**(9):754–769.

[19] Müller-Plathe F. Scale-hopping in computer simulations of polymers. *Soft Materials* 2003; **1**(1):1–31.

[20] Reith D, Pütz M, Müller-Plathe F. Deriving effective mesoscale potentials from atomistic simulations. *Journal of Computational Chemistry* 2003; **24**(13):1624–1636.

[21] Milano G, Müller-Plathe F. Mapping atomistic simulations to mesoscopic models: A systematic coarse-graining procedure for vinyl polymer chains. *The Journal of Physical Chemistry B* 2005; **109**(39):18 609–18 619.

[22] Rahimi M, Karimi-Varzaneh HA, Böhm MC, Müller-Plathe F, Pfaller S, Possart G, Steinmann P. Nonperiodic stochastic boundary conditions for molecular dynamics simulations of materials embedded into a continuum domain. *Journal of Physical Chemistry* 2011; **134**:154 108.

[23] Qian H, Carbone P, Chen X, Karimi-Varzaneh HA, Müller-Plathe F. Temperature-transferable coarse-grained potentials for ethylbenzene, polystyrene, and their mixtures. *Macromolecules* 2008; **41**(24):9919–9929.

[24] Rahimi A, Rahimi M, Böhm MC, Müller-Plathe F. Coarse grained molecular dynamics simulation of polystyrene–silica nanocomposite: Dynamics in the interphase and polymer–mediated interactions of nanoparticles ; **in preparation**.

[25] Karimi-Varzaneh HA, Qian HJ, Chen X, Carbone P, Müller-Plathe F. Ibisco: A molecular dynamics simulation package for coarse-grained simulation. *Journal of Computational Chemistry* 2011; **32**:1475–1487.

[26] Español P, Warren P. Statistical mechanics of dissipative particle dynamics. *Europhysics Letters* 1995; **30**:191.

[27] Koelman JMVA, Hoogerbrugge PJ. Dynamic simulations of hard-sphere suspensions under steady shear. *Europhysics Letters* 1993; **21**:363.

[28] Delgado-Buscalioni R, Kremer K, Praprotnik M. Concurrent triple-scale simulation of molecular liquids. *The Journal of Chemical Physics* 2008; **128**:114 110.

[29] Belytschko T, Krongauz Y, Organ D, Fleming M, Krysl P. Meshless methods: An overview and recent developments. *Computer Methods in Applied Mechanics and Engineering* 1996; **139**:3–47.

[30] Rahimi M, Iriarte-Carretero I, Rahimi A, Böhm MC, Müller–Plathe F. Mechanical behavior and interphase structure in a silica-polystyrene nanocomposite under uniaxial deformation. *Nanotechnology* 2012; **23**:305 702.

[31] Lyulin AV, Balabaev NK, Mazo MA, Michels MAJ. Molecular dynamics simulation of uniaxial deformation of glassy amorphous atactic polystyrene. *Macromolecules* 2004; **37**(23):8785–8793.

[32] Heinrich G, Vilgis TA. Contribution of entanglements to the mechanical properties of carbon black-filled polymer networks. *Macromolecules* 1993; **26**(5):1109–1119.

[33] Everaers R, Kremer K. Elastic properties of polymer networks. *Journal of Molecular Modeling* ; **2**:293–299.

[34] Rahimi A, Ndoro TVM, Leroy F, Rahimi M, Böhm MC, Müller-Plathe F. Interphase structure in silica–polystyrene nanocomposites: A coarse-grained molecular dynamics study. *Macromolecules* 2011; **45**:572–584.

[35] Abrams CF, Delle Site L, Kremer K. Dual-resolution coarse-grained simulation of the bisphenol-*a* -polycarbonate/nickel interface. *Physical Review E* Feb 2003; **67**:021 807.

[36] Allen P, Tildesley D. *Computer Simulation of Liquids*. Oxford Science Publications, Clarendon Press, 1987.

[37] Qian HJ, Liew CC, Müller-Plathe F. Effective control of the transport coefficients of a coarse-grained liquid and polymer models using the dissipative particle dynamics and lowe-andersen equations of motion. *Phys. Chem. Chem. Phys.* 2009; **11**:1962.

[38] Pfaller S, Possart G, Steinmann P, Rahimi M, Müller-Plathe F, Böhm MC. A comparison of staggered solution schemes for coupled particle–continuum systems modeled with the arlequin method. *Computational Mechanics* 2012; **49**:565–579.

Conclusions and Outlook

The present PhD thesis has been focused on developing a new hybrid scheme to couple a molecular dynamics (MD) to a continuum mechanics which is described by finite elements (FE). To achieve this goal a lot of modifications have been done in both MD and FE domains. The main part of the current study was focused on modifications in the MD domain. New nonperiodic boundary conditions were developed in order to couple the MD to the FE description. These boundary conditions, so-called stochastic boundary conditions, can transfer information (forces and displacements) between two domains by using some auxiliary particles i.e. so-called anchor points. To remove the artificial effects of the vacuum and anchor points, a stochastic dynamics algorithm has to be used in the boundary region. Therefore, we used the dissipative particle dynamics in the boundary regions. Thermodynamic, structural and dynamic properties of polystyrene melts were calculated under nonperiodic boundary conditions. Excellent agreement is found with periodic boundary results.

Finite element parameters were obtained from pure MD simulations. We have performed uniaxial tests by applying strain to one direction and coupling the two other directions to a barostat. The stress-strain curves of a pure polystyrene matrix as well as a polystyrene matrix filled with a bare silica nanoparticle were calculated at the coarse-grained level. The Young's modulus obtained from stress-strain curves and the Poisson ratio were used as FE parameters in the hybrid scheme.

A staggered coupling procedure was employed to couple the MD to the FE domain. This is the appropriate strategy to overcome the significant difference between the time steps in the two domains. The Arlequin method, which is a static method, has been used to find the equilibrium of the FE domain, while the MD domain has been treated dynamically. The two domains have an overlap in the bridging region and the total energy is blended here by a weighting factor. Information transfer between two domains in the bridging region takes place by using anchor points. In each iteration, time averaged forces on the anchor points are calculated in the MD domain. After that the FE domain changes the position of the anchor points according to the force on each anchor point and the external boundary conditions. This iterative procedure continues until having reached equilibrium. The hybrid scheme has been tested by simulating a pure polystyrene matrix as well as a polystyrene matrix filled with a bare silica nanoparticle at the coarse-grained level. We have validated the hybrid scheme by comparing the results of a hybrid simulation and a pure FE simulation. Reasonable agreement between hybrid and pure FE simulations is found by comparing quantities such as reaction forces and the Cauchy stress. However, there are some stress deviations in the boundary region between hybrid and pure FE simulations. They occur prevailingly in the corner of the MD domain. These deviations are not important for small deformations since they do not affect the results in the center of MD box. For

large deformations, however, the deformation in the MD domain might become completely unrealistic since the boundary is much softer than the center of the box. Therefore it affects the results in the center of the box.

In spite of the modifications and developments done in this work, many new challenges still wait to be tackled. As an example, it was shown that the stress deviation between the hybrid system and the pure FE system is high in the boundary region. This occurs especially in the corner of the MD domain. The main reason for this deviation is that chains in the boundary region are shorter than in the MD region and therefore they have a lower stiffness. This problem might be solved by using different weighting factors. The stiffness of the boundary region is the result of the weighted combination of the stiffness of the MD and FE domains. In our simulations, the two models have the same contribution, or in other words the weighting factor had a constant value of ½. By using different weighting factors, we can reduce the effect of the MD domain in the boundary region and therefore can reduce the stress deviation in the boundary region. We are currently working on this idea to see if it is possible to minimize the stress deviations between hybrid and pure FE simulations. Another possibility is that we increase the stiffness of this region artificially by employing artificial potentials. This solution needs a lot of modifications in the code. We also have to be sure that the artificial potentials do not affect the bulk properties of the polymers in the center of the box. For instance, such potentials might generate local structure near the interface of the boundary region and the MD region which both have an influence on polymers in the center of the box. It should be mention that the difference in the chain length in the boundary region and the center of the box is not the only reason for the stress deviations. It might have others sources that have to be traced. This topic needs more investigations to study the source of errors and how to fix them.

The method developed in the present PhD thesis is limited to small deformations (elastic regime) which can be described by Hooke's law. For a small deformation, the stored energy density can be expressed by the Young's modulus, and the Poisson ratio obtained from atomistic simulations. This approximation is not valid for a large deformation since amorphous polymers have a nonlinear behavior in this case. To solve this problem, we have to express the stored energy density by neo-hookean parameters[1]. They can be calculated by fitting a neo-hookean equation to the stress-strain curves obtained from atomistic simulations. The new method can be validated by comparing neo-hookean and hookean methods in the small deformation limit. It is worth mentioning that the neo-hookean method cannot predict the yielding point. It is valid only below the yielding point. However, we might be able to apply large deformations to study crazing and failure phenomena. The FE domain experiences only non-linear behavior while the MD domain can describe the yielding point, the softening regime and crazing. The continuity of the two descriptions in the boundary region should be

checked during the deformation. Modifications of the FE code for non-liner simulations are already finished and we are currently validating the modified code.

Applying a large deformation to a system which contains a polystyrene matrix filled with a bare silica nanoparticle would be an interesting topic to study. In this case, the MD domain must contain enough polymers to mimic the bulk behavior in the boundary region. Therefore, the FE parameters are the same as obtained for pure polystyrene. By applying a deformation we are able to study the mechanical properties of a nanocomposite which can be compared with a pure polystyrene. We can analyze the behavior of the polymer near the nanoparticle surface under the deformation by measuring molecular structural properties such as gyration radii, orientations, or the free volume. The present work can be extended by simulating systems with more than one nanoparticle and again studying the interphase region. One of the advantages of our model in comparison to other deformation methods with periodic boundary conditions is that the MD domain is flexible. For nanocomposites which are inhomogeneous materials this might be extremely important during the deformation. Therefore, the rectangular MD domain might deform to an arbitrary shape. Thus, it would be intriguing to compare the results obtained from simulations with flexible boundary conditions with those derived under periodic boundary conditions which are not flexible.

Another interesting work that can be done is to identify the FE parameters for the interface with the help of hybrid results. To this end, a pure FE system should be defined with one nanoparticle surrounded by polymers. The nanoparticle should be covered with a layer of zero thickness elements which are controlled by a properly defined potential. Actually this potential is the free interface energy density, which replaces the interphase in the FE system[2–5]. The potential should be adjusted in the way that we have the same mechanical behavior in the hybrid method as the FE method. Thus the free interface energy density will be identified according to the stress-strain curves obtained from the hybrid simulations of the nanocomposite,. The FE parameters are adjusted iteratively until the deformation behavior coincides to that obtained from hybrid simulations. Once we reproduce the interphase in the pure FE system, we can simulate systems with many nanoparticles in a macroscopic scale.

References

(1) Holzapfel, G. A. *Nonlinear Solid Mechanics: A Continuum Approach for Engineering*; John Wiley, 2000.

(2) Javili, A.; Steinmann, P. *Computer Methods in Applied Mechanics and Engineering* **2009**, *198*, 2198-2208.

(3) Javili, A.; Steinmann, P. *Computer Methods in Applied Mechanics and Engineering* **2011**, *200*, 1963-1977.

(4) Javili, A.; McBride, A.; Steinmann, P.; Reddy, B. D. *Philosophical Magazine* **2012**, 1-24.

(5) Javili, A.; Steinmann, P. *Computer Methods in Applied Mechanics and Engineering* **2010**, *199*, 755-765.

Publications

(1) Rahimi, M., Karimi-Varzaneh, H. A., Böhm, M. C., Müller-Plathe, F., Pfaller, S., Possart, G., & Steinmann, P. (2011). Nonperiodic stochastic boundary conditions for molecular dynamics simulations of materials embedded into a continuum mechanics domain. *The Journal of chemical physics*, *134*(15), 154108. doi:10.1063/1.3576122

(2) Pfaller, S., Possart, G., Steinmann, P., Rahimi, M., Müller-Plathe, F., & Böhm, M. C. (2011). A comparison of staggered solution schemes for coupled particle–continuum systems modeled with the Arlequin method. *Computational Mechanics*, 1-15. Springer Berlin / Heidelberg. doi:10.1007/s00466-011-0657-7

(3) Ghanbari, A., Ndoro, T. V. M., Leroy, F. D., Rahimi, M., Böhm, M. C., Müller-Plathe, F. (2012). Interphase Structure in Silica − Polystyrene Nanocomposites : A Coarse-Grained Molecular Dynamics Study. *Macromolecules*, *45*, 572-584.

(4) Rahimi, M., Iriarte-Carretero, I., Ghanbari, A., Böhm, M. C., & Müller-Plathe, F. (2012). Mechanical behavior and interphase structure in a silica - polystyrene nanocomposite under uniaxial deformation. Nanothechnology *23* 305702

(5) Ghanbari, A., Rahimi, M., Böhm, M. C., Müller-Plathe, F. A Coarse-Grained Molecular Dynamics Simulation of Polystyrene-Silica Nanocomposite: Dynamics in the Interphase and Polymer-Mediated Interactions of Nanoparticles. Submitted

(6) Pfaller, S., Rahimi, M., Possart, G., Steinmann, P., Müller-Plathe, F., & Böhm, M. C. An Arelequin-based method to couple molecular dynamics and finite element simulations of amorphous polymers and nanocomposites. Submitted to Computer Methods in Applied Mechanics and Engineering

Financial Support

This work has been funded by the EU project NanoModel (211778) as well as by the Deutsche Forschungsgemeinschaft through the Priority Programme 1369 “Polymer-Solid Contacts: Interfaces and Interphases”.

Acknowledgments

I am very grateful to my supervisor Prof. Dr Florian Müller-Plathe who gave me an apportunity to his group as a PhD student. His impressive knowledge, patience, and energy have been crucial during my PhD time. His hints and punctual advices have been, for me, a great treasure to improve my professional and personal life.

I would like thank Prof. Dr Michael C. Böhm for his support and daily attention to my work. Our scientific discussions and his advices have been grateful to me and make me more productive.

The patience of Jessica Alhuwalia, Kristin Adolph and Dana Voss in dealing with some of our administrative issues and their effort in maintaining a warm atmosphere in the group has been highly appreciable.

I would like acknowledge all people in our group, Dr. Frédéric Leroy, Prof. Hossein Eslami, Dr.-Ing. Hans-Jürgen Bär, Dr. Evangelos Voyiatzis, Dr. Enrico Riccardi, Dr. Simon Butler, Dr. Jianguo Zhang, Dr. Ganesh Balasubramanian, Dr. Tinashe Ndoro, Dr. Azadeh Ghanbari, Michael Langeloth and Mezian Yahia-ouahmed, for the moment we spent together. I have had great time with them and I have learned many things from each of them.

My deep gratitude is addressed to my co-workers in Department of Engineering Mechanics in Erlangen, Prof. Dr.-Ing. hab. P. Steinmann, Gunnar Possart and Sebastian Pfaller. Espessialy I wish to offer my deep gratitude to Sebastian Pfaller for his kindness and patience in helping me and answering my questions. Beside this, he had unforgettable role in my work with his friendly and warm-hearted behavior.

Finally, I want to dedicate my deep thanks to my family for their support and encouragement. There is no word to express what a son owes to his parents; to mine I just want to tell that they have been – and this is of course totally subjective - the best parents in the world and that I love them very much. The same holds for my sister; she belong to the best parts of my life.

Curriculum Vita

Name: Mohammad

Last Name: Rahimi

Place of Birth: Isfahan (Iran)

Date of Birth: 7/6/1981

Nationality: Iranian

Education

1999-2004: Kashan University (Iran), (BSc of Physics)

2004-2007: Isfahan University of Technology (Iran), (MSc of physics)

2009-2012: PhD student in theoretical physical chemistry, Technical University of Darmstadt, Germany.

(Mohammad Rahimi)

Mohammad Rahimi
Ingelheimer str 1
64295 Darmstadt
Germany

Darmstadt, 5 of October, 2012

Erklärung

Ich erkläre hiermit, noch keinen Promotionsversuch unternommen zu haben.

_____

(Mohammad Rahimi)

Mohammad Rahimi
Ingelheimer str 1
64295 Darmstadt
Germany

Darmstadt, 5 of October, 2012

Eidesstattliche Erklärung

Ich erkläre hiermit an Eides Statt, dass ich meine Dissertation selbständig und nur mit den angegebenen Hilfsmitteln angefertigt habe.

_____

(Mohammad Rahimi)